An Infrared and Optical View of Young Eruptive Stars

PhD Thesis

Written by: Ágnes Kóspál

PhD School of Physics
Particle- and Astrophysics Programme
Eötvös Loránd University, Faculty of Science

Head of PhD School: Prof. Zalán Horváth
Head of PhD Programme: Prof. Ferenc Csikor

Supervisor: Dr. Kristóf Petrovay, associate professor, Eötvös University
Thesis Advisor: Dr. Péter Ábrahám, senior research fellow, Konkoly Observatory

Konkoly Observatory of the Hungarian Academy of Sciences

Budapest, Hungary
2008

Foreword

I started scientific research in 2003. I joined the Konkoly Infrared and Space Astronomy group, and started working on young eruptive stars under the supervision of Péter Ábrahám. Since then, I had the opportunity to travel to a lot of conferences, to visit several astronomical institutes, to get to know many very helpful colleagues from all over the world, and to participate in different projects, all more or less related to star formation or infrared astronomy.

Recently, I underwent a few job interviews and once I was asked what I found the most important scientific result in astronomy in the last ten years. I was not prepared for this question at all. I have always felt comfortable when working on young stars and infrared data. It always provided me with the necessary challenge and also gave the necessary satisfaction when I realized something no one knew before me, but I have never tried to phrase why the topic I am working on is successful. I think I know the answer now, or at least some elements of it. I believe that the research on star formation and the technology that made this research possible, infrared astronomy, has been one of the most dynamically developing field in the last ten years. It would be difficult to choose a single discovery that I find the most important. Instead, in the following I highlight a few important steps that led the research of star formation where it is nowadays.

Most of the infrared radiation coming from the Universe is blocked by Earth's atmosphere. To solve this problem, infrared detectors were first installed on balloons and rockets, later on special airplains. The first astronomical satellite working at infrared wavelengths, the *Infrared Astronomical Satellite* (IRAS) was launched in 1983 and its observations revealed a whole new world to astronomers. It turned out that – contrary to the night sky in the visible – the night sky at infrared wavelengths is not dark at all, but bright from the emission of cold interstellar matter (galactic cirrus). It turned out that there are protostars so embedded in gas and dust that they are only visible in the infrared. It was discovered that not only young stars can have circumstellar disks, but also main-sequence stars (debris disks, Vega-phenomenon).

The *Infrared Space Observatory* (ISO) working between 1995 and 1998 already had infrared spectrometers on-board. Spectra made it possible to study the chemical composition

of the Universe. ISO discovered the presence of water vapour in star-forming regions. It also detected the signs of hydrogen fluoride, and many other molecules in the interstellar medium. Thanks to its far-infrared detectors, ISO was able to detect the earliest stages of star formation: cold pre-stellar cores invisible even at near- or mid-infrared wavelengths.

The *Spitzer Space Telescope*, launched in 2003 and still working as of 2008, has an unprecedented sensitivity and spatial resolution. Spitzer is extremely productive, thus I do not attempt to summarize its contribution here. Press releases – many of which is related to young stars – are coming out every few weeks.

Not only space missions, but ground-based instruments are also developing. The 10 m-class telescopes at Paranal Observatory or at Mauna Kea, equipped with adaptive optics, can often reach or even exceed the resolution of space-borne instruments. Interferometry, which in the past was only available for radio telescopes, is now working in the mid-infrared (VLT/MIDI), and in the near-infrared (VLTI/AMBER and Keck Interferometer) wavelength regime. With the help of these instruments, circumstellar disks can be studied at a milliarcsecond scale.

The future of star formation studies is very exciting. The construction of many second generation instruments for the VLT is in the design phase. The *Herschel* and *Planck* satellites will be launched soon. The *James Webb Space Telescope*, with a 6.5 m mirror will also work at infrared wavelengths. These instruments are all very well suited for studying star formation, planet formation and the interstellar matter. This is an exciting time to be an astronomer and I'm happy that I'm one of them.

Contents

List of Figures

List of Tables

Chapter 1

Introduction

1.1 Star formation

Stars represent only a part of the total mass of our Milky Way. 10-15% of the material is present in the form of interstellar medium. Star formation in this medium is ongoing still nowadays. Our primary source of information about star formation comes from nearby star-forming regions: Orion, Taurus, Perseus, Cepheus, Aquila, Serpens, Ophiuchus (Fig. 1.1), Scorpius, Lupus and Chamaeleon. These regions are parts of the Gould Belt, a giant ring of young stars and dense molecular clouds at a distance of 100−400 pc.

The molecular clouds are in a delicate equilibrium which can easily be upset. Forces such as the thermal gas pressure, magnetic fields, and turbulent motions resist gravity. Molecular clouds are not homogeneous, but have a very complex structure with clumps and filaments. Parts of a cloud might start collapsing spontaneously, while other parts might be disturbed by e.g. supernova explosions or the stellar wind of high-mass stars. In these cases, gravity can overcome the resisting forces and denser parts of the molecular cloud form gravitationally contracting *cloud cores*. Molecular cloud cores typically have densities of 10^3−$10^4\,\mathrm{cm}^{-3}$, sizes of a few times 0.1 pc, and masses of a few solar masses. According to current theories of star formation, many low-mass ($<2\,\mathrm{M}_\odot$), solar-type stars are formed in such cloud cores. In the following I focus on the formation of low-mass stars, partly because high-mass star formation is not well-known yet, partly because this work deals with low-mass stars, and summarize the formation of low-mass stars following Shu et al. (1987) and André et al. (1993).

Figure 1.1 Star formation in the ρ Ophiuchi cloud. The youngest stars are surrounded by dusty disks and thus appear as reddish-yellowish dots. More evolved stars, which have already cleared their surroundings, are bluish-white. (Image taken by the Spitzer Space Telescope, NASA/JPL-Caltech/Harvard-Smithsonian CfA.)

The cloud core is initially starless. It is in hydrostatic equilibrium, but it rotates and contracts very slowly. Though the core is only slightly ionised, on large scales magnetic fields play an important role in stabilising the core. Due to the *ambipolar diffusion*, the core gradually loses magnetic flux. Eventually it becomes unstable to gravitational collapse. The free-fall collapse starts in the center, then spreads outwards (*inside-out collapse*). At the beginning, the material is tenuous enough so that it is transparent for its own thermal radiation. Therefore, the contraction is isotherm. When the cloud core becomes so dense at the center that it is optically thick for infrared radiation, the temperature and pressure start increasing. Eventually the collapse stops in the center and a *first core* forms, which is in equilibrium, but which still accumulates material from its surroundings. The mass of the first cores is usually only a few hundredths of solar masses, and their size is a few AU. Initially they are composed mostly of molecular hydrogen, but due to the continuous mass accretion, and the increasing temperature, hydrogen molecules dissociate. At that point, the

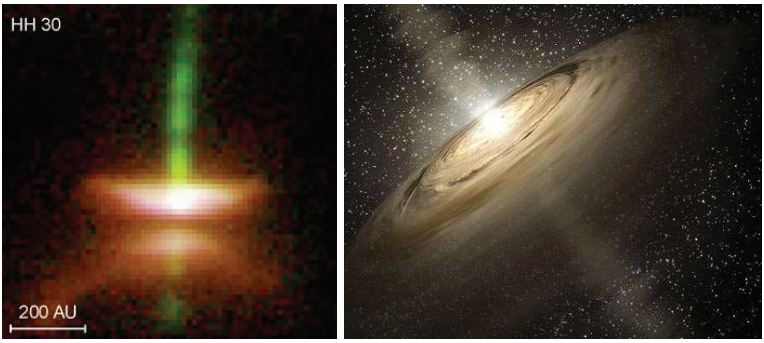

Figure 1.2 *Left:* Hubble Space Telescope image of the HH 30 system, a young star with outflows and an edge-on disk (C. Burrows and J. Krist, STScI, K. Stapelfeldt, JPL, and NASA). *Right:* Artist's concept illustrating a young star with outflows and a dusty disk (NASA/JPL-Caltech/T. Pyle).

released accretion energy does not lead to the increase of temperature any more, but it causes more molecules to dissociate. Thus, the first core becomes unstable and it collapses rapidly, forming a *protostar*. Protostars already contain ionised hydrogen (their central temperature is 10^5 K), their mass is a few tenth of solar masses, their size is a few solar radii. They form in about 10 000 years after the start of the gravitational collapse.

Due to the non-zero angular momentum of the initial cloud core, material cannot fall directly to the protostar's surface, but it forms a disk-like structure. In the disk, the material is slowly spiralling inwards. At this stage, the protostar and the accretion disk are still deeply embedded in the surrounding envelope (*Class 0 object*). As the star accretes material from the disk, a bipolar outflow might form, in which material flows from the poles of the protostar and starts clearing away the envelope (*Class I object*, see also the reddish-yellowish dots in Fig. 1.1, and the system in Fig. 1.2). This happens in about 100 000 years after the start of the gravitational collapse. Inside the protostar, first deuterium, then hydrogen starts fusing. The star becomes optically visible and appears at a special place in the Hertzsprung-Russell diagram: the *birthline*. Young stars having masses less than $2\,M_\odot$ are called T Tauri stars, while those between 2 and $8\,M_\odot$ are called Herbig Ae/Be stars. When the remnant envelope can no longer supply the disk with material, accretion rate becomes lower and lower. Stellar

wind starts blowing and the star slowly blows away most material that is still present apart from the disk. The disk becomes passive: its main energy source is no longer the accretion but the irradiation from the central star (*Class II object*, see also the bluish-white dots in Fig. 1.1). This takes about 1 million years. At this stage, planetesimals and planets might also form in the disk. Finally, most of the gas and dust content of the disk disperses or coagulates into larger bodies (*Class III object*). The inner parts of the disk disappear during the first few million years, while the outer parts can exist for several tens or hundred million years. *Planets* might also form during this stage. Collisions between planetesimals might induce a collisional cascade leading to a second generation of small dust grains: a *debris disk*.

Figure 1.3 shows the timescale of the different stages and the corresponding spectral energy distribution. The spectra of pre-main sequence objects are usually very complex. Apart from the radiation of the star itself, the emission of the disk and the envelope is also visible. Moreover, at certain wavelengths (especially in the infrared and submm wavelength range), the disk and the envelope dominates the spectrum. Cloud cores are only observable in the submm-mm-radio regime. A Class 0 source is also radiating at far-infrared wavelengths. In the spectrum of a Class I source, one can see the (proto)stellar photosphere (mainly at near-infrared wavelengths) and a huge mid- and far-infrared excess due to the disk and envelope. The main source of energy is the accretion luminosity. In a Class II source, most energy comes from the stellar photosphere, which is hot enough to be observable at optical wavelengths. In the infrared, however, the spectrum is still dominated by the disk emission (reprocessed starlight). A Class III object has only a very modest infrared excess due to the remnant disk.

A very detailed description of the formation of stars can be found in Stahler & Palla (2004).

1.2 Eruptive phenomena

In late 1936 a star appeared in the elongated dark nebula B35 within the Orion star forming region (Wachmann, 1954). Subsequent examination showed that FU Orionis (because this is the star in question) was about 16.4−15.3 mag earlier, then it brightened by about 5

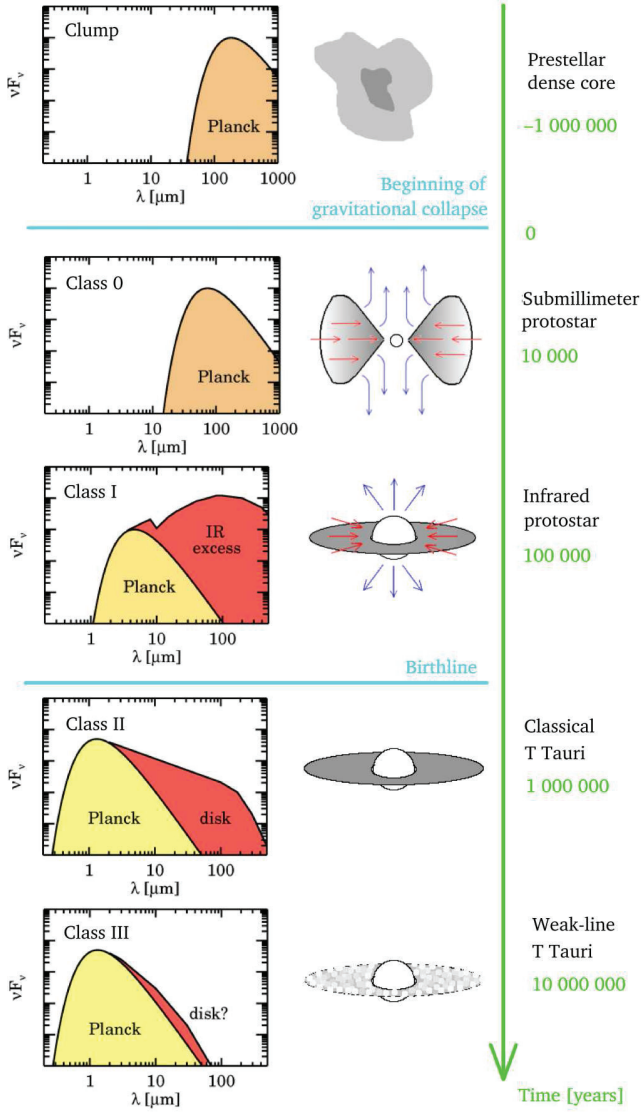

Figure 1.3 Classification of young stellar objects (after Shu et al., 1987; André et al., 1993).

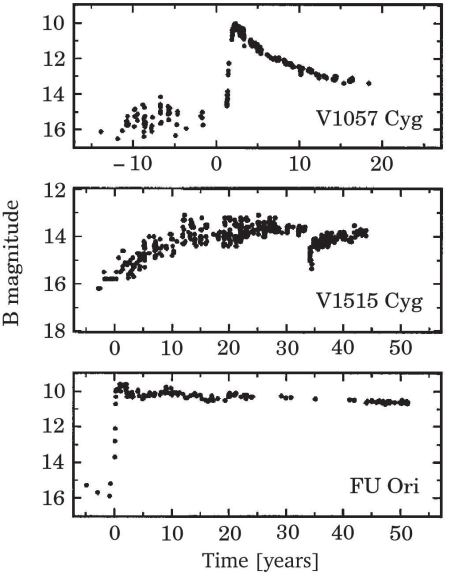

Figure 1.4 Light curve of the outburst of three FUor-type stars (Hartmann & Kenyon, 1996).

magnitudes, and is still above 11 mag. The ideas that the star emerged from an obscuring nebula, or that it is an extremely slow nova were soon rejected by Herbig (1966). He proposed that the flare-up of FU Ori represents a phenomenon of early stellar evolution. During the following decade, two similar objects were discovered: V1057 Cyg and V1515 Cyg. With these three objects as prototypes, Herbig (1977) defined a special class of young stellar objects: FU Orionis-type stars or shortly *FUors*. Fig. 1.4 shows the light curves of the three prototypes.

FU Ori, V1057 Cyg and V1515 Cyg have been extensively studied, and soon more young stars were found which resembled these prototypes, either because they also exhibited a ≈5 magnitude brightening, or because – though no outburst was observed – their spectral characteristics were similar to those of the prototypes. Currently we know roughly 20 FUors (including candidates, see Ábrahám et al. 2004a). Their most important properties can be summarised as follows:

– FUors whose outburst is well-documented show a 4−5 magnitude brightening at optical wavelengths. They reach the maximum brightness in a few months or few years. This is followed by a slow fading phase lasting several decades or even a century. As Fig. 1.4 suggests, the light curves can be very different for each object.

– FUors are young objects. They are often associated with star forming regions, illuminate reflection nebulae (Fig. 1.5), and have other young stars (T Tauri or Herbig Ae/Be stars) in their vicinity. They also often exhibit strong Li I 0.6707 μm absorption characteristic of young stars.

– The spectral type of FUors depends on the wavelength: they are F−G supergiants based on their optical spectra, while K−M giants or supergiants based on the near-infrared spectra.

– In the optical spectrum, broad blueshifted Balmer lines and Na resonance lines can be observed. Near-infrared spectra of FUors often show strong CO absorption at 2.2 μm and water vapour bands in the 1-3 μm regime. At high spectral resolution, many optical and near-infrared lines turned out to have a double-peaked profile and indicate high rotation velocities (consistent with a rotating disk).

– A pre-outburst spectrum of V1057 Cyg suggests that the precursors of FUors are probably T Tauri stars.

– All FUors show large infrared excess emission, a sign of a large amount of circumstellar material.

There exists another type of young stars that show eruptions of similar magnitude to FUors but of shorter duration. *EXors* (named after the prototype EX Lupi) are young stars showing 1−4 mag repetitive brightenings. These eruptions usually last some weeks or some months and the time between adjacent eruptions ranges from some months to some years. Fig. 1.6 shows the light curve of the EXor-type star VY Tau. The spectral type of EXors is K−M dwarf and at maximum brightness, their optical/near-infrared spectra are dominated by emission features characteristic of classical T Tauri stars (Herbig, 1977, 1989; Hodapp

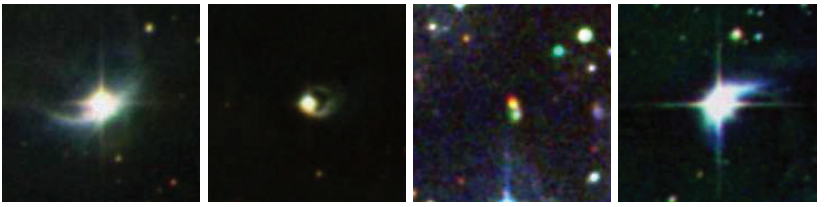

Figure 1.5 FUors in the near-infrared. 2MASS J H K_S composite images of FU Ori, V1515 Cyg, V346 Nor and Z CMa (from left to right, respectively).

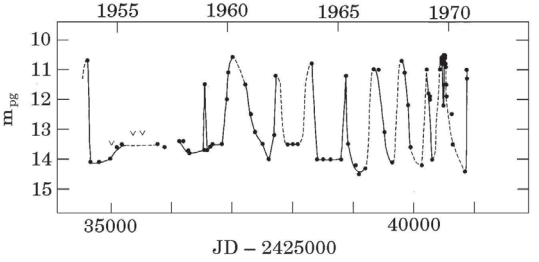

Figure 1.6 Light curve of the EXor-type star VY Tau (Herbig, 1977).

et al., 1996b). It is possible that the outburst mechanisms of FUors and EXors are similar: EXors are the somewhat scaled-down versions of FUors (e.g. Hessman, 1991a).

Some objects, especially the newly discovered young eruptive stars (e.g. OO Ser, V1647 Ori) cannot be unambiguously classified into the two groups mentioned above. Their light curves and spectral characteristics suggest that they may be intermediate objects.

What mechanism can increase the brightness of a star by a factor of 100 and keep it at such a high level for decades? The answer lies in the circumstellar material. It is certainly not the star itself that flares up. Young eruptive stars are Class I or Class I/Class II transition objects (Quanz et al., 2007), thus they have active accretion disks. Fig. 1.7 shows a widely-used model for the circumstellar geometry of FUors. According to the most accepted model for FUor and EXor eruptions, the brightening is due to enhanced accretion from the circumstellar disk to the stellar photosphere (Bell et al., 1995; Hartmann & Kenyon, 1996).

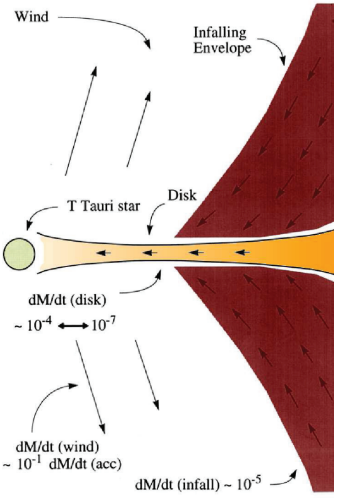

Figure 1.7 Schematic picture of FUors (adopted from Hartmann & Kenyon, 1996).

In quiescence, the accretion rate through the disk is a steady $\approx 10^{-7} M_{\odot}/\mathrm{yr}$ (the reservoir that provides the disk with enough material might be the envelope in which the star+disk system is embedded). However, since the disk is not very hot yet, turbulent motions are not particularly violent. If turbulence is not significant, inner friction (i.e. viscosity) in the disk material will be low, leading to inefficient transfer of angular momentum, and thus low accretion rate. As a consequence, part of the material does not flow directly to the stellar surface, but accumulates in the disk close to the star (typically within 0.25 AU from the star).

As more and more material accumulates in the inner disk, the density and the opacity increases and the disk material becomes opaque to its own thermal radiation, leading to increasing temperature. Gas opacity increases very steeply in the 5000−10 000 K temperature range because of the ionisation of hydrogen. This makes it possible to have a thermal instability in this range. When the instability switches on, an ionisation front develops and soon, the complete inner disk becomes fully ionised. Since the ionised material has a different (higher) viscosity than that of the neutral, accretion can be much more effective.

Accretion rate rises to $\approx 10^{-4}\,M_\odot/yr$, and suddenly a large amount of material falls onto the stellar surface. As the ionisation front propagates outwards, more and more material becomes ionised and the brightness of the system becomes larger and larger. This is what can be observed as a *FUor outburst*. During the high accretion phase, the hot material in the inner disk emits most of its energy at ultraviolet and optical wavelengths, and by far outshines the star. Eventually the mass accumulated in the inner disk depletes. What material remains recombines and the outburst ends. Material starts accumulating again and the cycle is repeated. FUor outbursts probably recur on timescales of several thousand years.

There are several theories about what can trigger the thermal instability in the disk. One idea is that the close passing of a binary companion may produce these episodic outbursts. A sufficiently high perturbation in the surface density of the disk results in a fast risetime, similarly to what can be seen in the light curve of V1057 Cyg or FU Ori in Fig. 1.4. Another mechanism is a spontaneous, self-regulated thermal instability, when the ionisation front is initiated at the inner edge of the disk and slowly propagates outwards. This leads to a slow risetime, as demonstrated by V1515 Cyg in Fig. 1.4.

The flare-up of a FUor does not only observable at optical wavelengths, but can also be detected in the infrared. Depending on the exact wavelength, the infrared emission traces outer, cooler parts of the circumstellar disk and the possible envelope around the system. In an earlier study (Ábrahám et al., 2004a), we investigated the long-term flux evolution of seven FUors by comparing their IRAS and ISO observations obtained in 1983 and in 1996-1997, respectively. At $\lambda \leq 25\,\mu$m we detected flux changes (either fading and brightening), while the longer wavelength part of the spectral energy distribution remain constant. An example, V1057 Cyg, can be seen in Fig. 1.8.

Although the number of known FUors is relatively small compared to all known low-mass young stars, the occurrence of FUor outbursts cannot be considered infrequent. Following the argumentation of Hartmann & Kenyon (1996), let us suppose that all low-mass young stars undergo such eruptions. Eruptions recur in every 10 000 or 100 000 years. Statistics show that there is about 10 FUor eruptions per star. With accretion rates as high as $10^{-4}\,M_\odot/yr$, the star accretes one hundredth solar masses during a century-long outburst. Repetitive outbursts might supply the star with one tenth of solar mass, making the high accretion

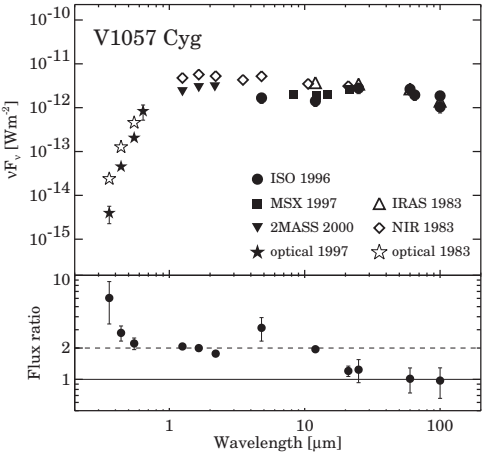

Figure 1.8 Spectral energy distribution of V1057 Cyg (Ábrahám et al., 2004a).

phase an important episode in the star's pre-main sequence life, maybe a link between the more embedded Class I objects and the more evolved Class II objects (Quanz et al., 2007).

1.3 Circumstellar structure around young stars

As it was already mentioned in the previous two subsections, the circumstellar material around young stars is usually in the form of a disk and an envelope. The material around the star has a considerable effect on the spectral energy distribution of the system. There are wavelengths, where the star is practically invisible and the emission is dominated by the disk and the envelope. The circumstellar material scatters the light of the central star, resulting in such reflection nebulae as in Fig. 1.5. Scattering is more efficient at shorter wavelengths, thus a reflection nebula around a low-mass young star is best seen at optical wavelengths. The circumstellar material (or more precisely the dust grains in it) also emits its own thermal radiation, mostly at infrared and submm wavelengths, due to its temperature (usually between 10−1000 K).

According to Shu et al. (1987), disks around young stars have basically two types: passive or active disks. Passive disk absorb and reemit the light from the central star. Active disks

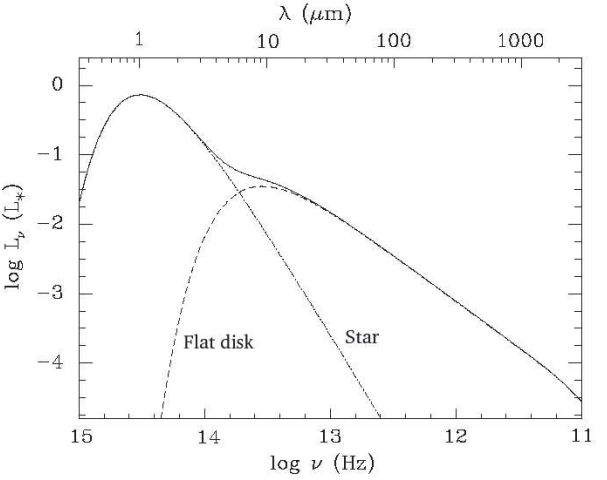

Figure 1.9 Spectral energy distribution of a star + flat blackbody disk system (Chiang & Goldreich, 1997).

are self-luminous, since they have their own energy source (viscous heating). The simplest model for a passive disk is a geometrically thin, optically thick flat disk (e.g. Hartmann, 2000). The disk absorbs the incident starlight and it reradiates as a blackbody corresponding to the local temperature. In such a configuration, the disk luminosity is $L_d = \frac{1}{4}L_*$, the radial temperature profile is $T_d \sim R^{-3/4}$, and the spectral energy distribution is $\nu F_\nu \sim \nu^{4/3} \sim \lambda^{-4/3}$ (Fig. 1.9). Interestingly, in case of active disks, the radial temperature profile – and thus also the spectral energy distribution – scales with the same exponent as for the passive disk. However, the total luminosity is proportional to the accretion rate, thus it can be higher than $\frac{1}{4}L_*$ (Shakura & Sunyaev, 1973).

If we do not specify an infinitely thin disk, we can calculate its thickness by supposing vertical hydrostatic equilibrium. From this, the vertical scale height of the disk as a function of radius is $H \sim R^{9/7}$ (Kenyon & Hartmann, 1987). Such a disk is opening up at larger radii (*flared disk*). Since the disk can absorb more starlight than a flat disk, its temperature profile will be shallower, resulting in a broader, flatter spectral energy distribution ($\nu F_\nu \sim \lambda^{2/3}$, Fig. 1.10). An even more realistic model includes an optically thin disk atmosphere, which

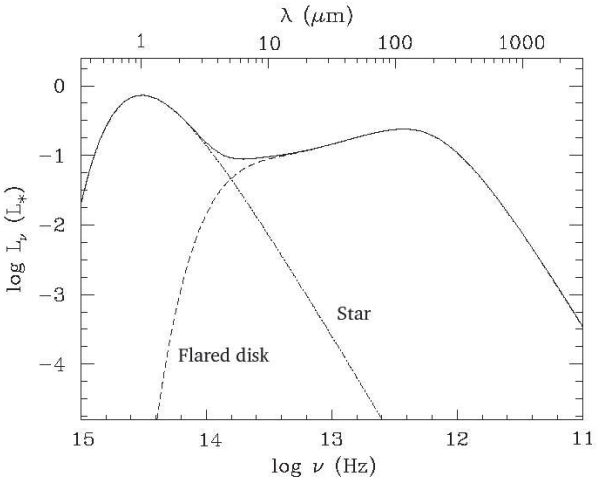

Figure 1.10 Spectral energy distribution of a star + flared blackbody disk system (Chiang & Goldreich, 1997).

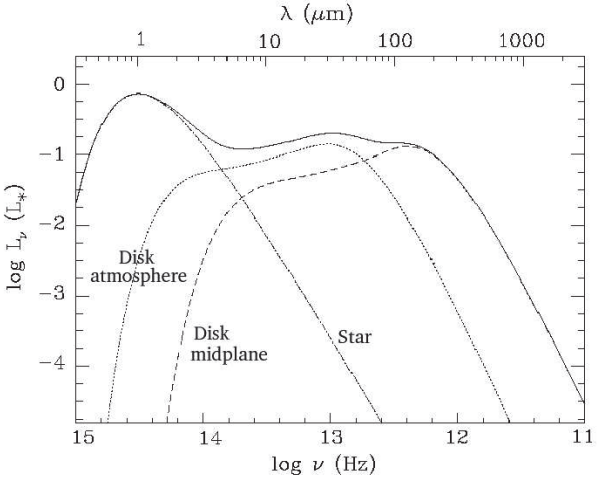

Figure 1.11 Spectral energy distribution of a star + hydrostatic, radiative equilibrium disk system (Chiang & Goldreich, 1997).

absorbs the stellar radiation and heats the disk interior (Chiang & Goldreich, 1997). Fig. 1.11 shows the SED of such a model.

The radial temperature profile of a circumstellar disk (either flat or flared) falls like $T \sim R^{-q}$, where $q = 0.5 - 0.75$. There are sources, however, where the slope of the SED indicates a shallower temperature profile. This is probably a signature of an optically thin circumstellar envelope (Adams et al., 1987). In fact, envelopes and disks probably coexist in many systems.

Chapter 2

The Infrared Monitoring of the Outburst of OO Serpentis

2.1 Introduction

OO Serpentis ($\alpha_{2000} = 18^{\rm h}29^{\rm m}49^{\rm s}$, $\delta_{2000} = +01°16'20''$) is a deeply embedded pre-main sequence star in the Serpens NW star-forming region at a distance of 311 pc. In 1995 OO Ser underwent a large increase in K-band flux in less than 1 year, reaching its maximum brightness in 1995 October (Hodapp et al., 1996b). The object was not visible, even at peak brightness, in the J-band or at shorter wavelengths, therefore it is also known as Serpens Deeply Embedded Outburst Star (DEOS). In the H and K bands the object was observable but the emission is dominated by scattered light (Fig. 2.1). In the K-band Hodapp (1999) monitored the outburst until 1998 October, and found that after the peak OO Ser gradually faded at a rate faster than the typical fading rate of FUors, but slower than that of EXors. Its K-band spectrum (a steeply rising, smooth continuum) also differed from both FUor and EXor spectra, which usually exhibit absorption or emission features.

Eruptions of pre-main sequence stars are rare events, thus a new outburst is always noteworthy. The close link between the eruption phenomenon and the circumstellar material makes it crucial to document the outburst also at infrared wavelengths, where the circumstellar dust radiates. However, such observing programs are constrained by the availability of active infrared satellite missions. The physical analysis of the phenomenon is limited due

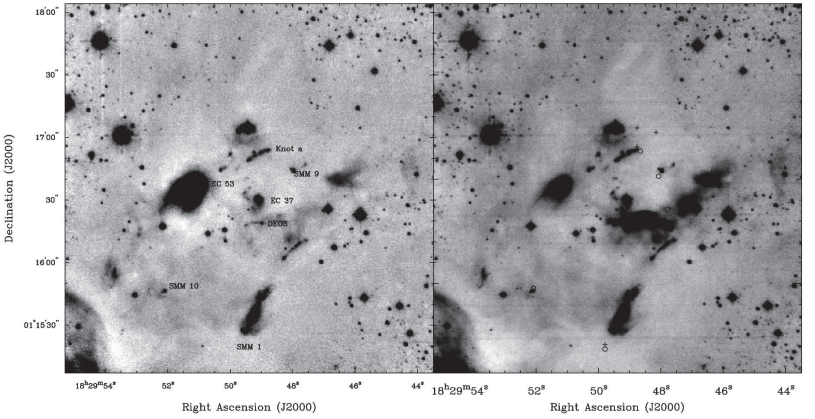

Figure 2.1 K-band images showing the surroundings of OO Ser from Hodapp (1999). The image to the left was taken in 1994 August, while the image to the right in 1998 September-October. Due to the outburst, OO Ser and its surrounding reflection nebulosity appear much brighter in 1998 than in 1994.

to the lack of preoutburst data. The eruption of OO Ser in 1995 provided a unique opportunity to collect such a dataset and carry out a multiwavelength infrared study of the whole outburst event for the first time.

Timo Prusti had a "Target of Opportunity" program submitted for the *Infrared Space Observatory* (*ISO*, Kessler et al., 1996). Triggered by the news on the outburst of OO Ser, this program was activated. The monitoring started 4 months after the maximum brightness of OO Ser and continued for 20 months. The ISO-SWS measurements from this program were published separately by Larsson et al. (2000). They found that OO Ser changed its infrared fluxes in the $2-45\,\mu$m range and estimated an extinction of $A_V \approx 20$ mag from the optical depth of the $10\,\mu$m silicate absorption feature. In an independent program the Serpens core was surveyed by the ISOCAM instrument providing 6.7 and $14.3\,\mu$m photometry on OO Ser for a single epoch (Kaas et al., 2004).

In the following I analyse the data from our ISOPHOT monitoring program and from the ISOCAM observations. In addition to the ISO measurements, OO Ser was observed from the ground at $2.2\,\mu$m in 2004 and 2006 as well as at $12\,\mu$m in 2004. I complemented this database with archival Spitzer data also from 2004, as well as with previously published

measurements on OO Ser from the literature.

2.2 Observations and data reduction

2.2.1 ISOPHOT observations

The *Infrared Space Observatory* (*ISO*, Kessler et al., 1996) was an astronomical satellite of the European Space Agency (ESA). It was operational between 1995 November and 1998 May. It operated at wavelengths between 2.5 and 240 μm. The telescope had a single 0.6 meter mirror and four instruments: an infrared camera (ISOCAM, Cesarsky et al., 1996), a photo-polarimeter (ISOPHOT, Lemke et al., 1996), a short wavelength spectrometer (ISO-SWS, de Graauw et al., 1996), and a long wavelength spectrometer (ISO-LWS, Clegg et al., 1996).

ISOPHOT, the photometer on-board ISO, carried out multi-filter photometry of OO Ser with 9 different filters in the 3.6−200 μm wavelength range and spectrophotometry in the 2.47−11.62 μm range, at 8 different epochs between 1996 February and 1997 September. Table 2.1 shows the log of the observations. In most cases small raster maps were obtained except in 1997 September, when at 25 μm and shortwards the source and background positions were observed separately. The typical integration time was 64 s. Aperture sizes varied according to the filters: 14″ at 3.6 μm, 18″ at 4.8 μm, 52″ at 12, 15, and 25 μm. At 60 and 100 μm the C100 camera (3×3 pixel, 43″×43″ per pixel), while at 170 and 200 μm the C200 camera (2×2 pixel, 89″×89″ per pixel) was utilised (the focal plane map of the ISOPHOT instrument can be seen in Fig. 2.2). Some far-infrared observations were performed in the PHT 32 mode, which provided higher spatial resolution (for a description of this mode see Tuffs & Gabriel, 2003).

2.2.2 ISOPHOT data processing

Standard processing and absolute flux calibration at $\lambda \leq 25\,\mu$m. The data reduction was performed using the ISOPHOT Interactive Analysis Software Package v10.0 (PIA, Gabriel et al., 1997, available from the ISO website[1]). Edited Raw Data (ERD) files were

[1] `http://www.iso.vilspa.esa.es/manuals/PHT/pia/pia.html`

Date	ISO_id	λ [μm]	Aper./pix. size [$''$]	Obs. mode	Map size	Δ [$''$]	Flux [Jy]	Abs. unc.	Rel. unc.
1996 Feb 28	10300901	3.6	13.8	Mapping	3×3	50×50	0.141	40%	11%
	10300901	4.8	18	Mapping	3×3	50×50	1.08	40%	1%
	10300901	12	52	Mapping	3×3	50×50	4.43	40%	25%
	10300902	25	52	Mapping	3×3	50×50	29.5	10%	10%
1996 Apr 14	14901404	3.6	13.8	Mapping	3×1	55	0.125	40%	10%
	14901404	4.8	18	Mapping	3×1	55	0.99	40%	3%
	14901404	12	52	Mapping	3×1	55	4.07	40%	3%
	14901405	25	52	Mapping	3×1	55	39.5	10%	3%
1996 Sep 01	29000208	3.6	13.8	Mapping	3×1	55	0.090	40%	8%
	29000208	4.8	18	Mapping	3×1	55	0.69	40%	4%
	29000208	12	52	Mapping	3×1	55	3.18	40%	5%
	29000208	15	52	Mapping	3×1	55	5.10	40%	14%
	29000210	60	43×43	Mapping	9×3	43×43	100	17%	-
	29000210	100	43×43	Mapping	9×3	43×43	116	19%	-
	29000212	200	89×89	PHT32 map	27×20	30×30	203	11%	-
	29000213	$2 - 12$	24×24	SP	3×1	45	-	-	-
1996 Oct 06	32500703	170	89×89	PHT32 map	5×8	90×46	162	15%	-
1996 Oct 24	34300314	3.6	13.8	Mapping	3×1	55	0.073	40%	-
	34300314	4.8	18	Mapping	3×1	55	0.62	40%	-
	34300314	12	52	Mapping	3×1	55	3.73	40%	-
	34300314	15	52	Mapping	3×1	55	4.89	40%	-
	34300315	25	52	Mapping	3×1	55	21.1	10%	-
	34300316	60	43×43	Mapping	9×3	43×43	101	16%	-
	34300316	100	43×43	Mapping	9×3	43×43	122	21%	-
	34300318	$2 - 12$	24×24	SP	3×1	45	-	-	-
1997 Mar 08	47800219	3.6	13.8	Mapping	3×1	55	0.076	40%	10%
	47800219	4.8	18	Mapping	3×1	55	0.53	40%	5%
	47800219	12	52	Mapping	3×1	55	2.98	40%	2%
	47800219	15	52	Mapping	3×1	55	4.50	40%	3%
	47800220	25	52	Mapping	3×1	55	18.5	10%	2%
	47800221	60	43×43	Mapping	9×3	43×43	88.2	16%	-
	47800221	100	43×43	Mapping	9×3	43×43	124	20%	-
	47800223	$2 - 12$	24×24	SP	3×1	45	-	-	-
1997 Apr 12	51301125	3.6	13.8	Mapping	3×1	55	0.060	40%	8%
	51301125	4.8	18	Mapping	3×1	55	0.61	40%	4%
	51301125	12	52	Mapping	3×1	55	3.25	40%	6%
	51301125	15	52	Mapping	3×1	55	4.20	40%	4%
	51301126	25	52	Mapping	3×1	55	18.9	10%	2%
	51301127	60	43×43	Mapping	9×3	43×43	85.3	15%	-
	51301127	100	43×43	Mapping	9×3	43×43	121	19%	-
	51301124	200	89×89	PHT32 map	27×20	30×30	233	13%	-
	51301129	$2 - 12$	24×24	SP	3×1	45	-	-	-
1997 Sep 22	67601730/31	4.8	18	ON/OFF	-	55	0.44	40%	-
	67601730/31	12	52	ON/OFF	-	55	2.03	40%	-
	67601730/31	15	52	ON/OFF	-	55	3.76	40%	-
	67601730/31	25	52	ON/OFF	-	55	17.1	10%	-
	67601732	60	43×43	Mapping	9×3	43×43	82.9	16%	-
	67601732	100	43×43	Mapping	9×3	43×43	118	20%	-
	67601734	$2 - 12$	24×24	SP	3×1	45	-	-	-
	67601735	6.7	1.5×1.5	ISOCAM	44×44	1.5×1.5	0.712	3.3%	-
	67601735	14.3	1.5×1.5	ISOCAM	44×44	1.5×1.5	3.53	4.8%	-

Table 2.1 Log of ISOPHOT and ISOCAM observations. SP stands for spectrophotometry. "Map size" indicates the sizes of the final maps. Δ denotes the increment between adjacent pixel positions in the map (mapping) or the separation between source and background positions (ON/OFF). At certain wavelengths the beam contained nearby sources; for a detailed discussion see Sec. 2.2.7. All fluxes are color corrected. The last two columns give the uncertainties of the absolute and the relative flux calibration (Sec. 2.2.2).

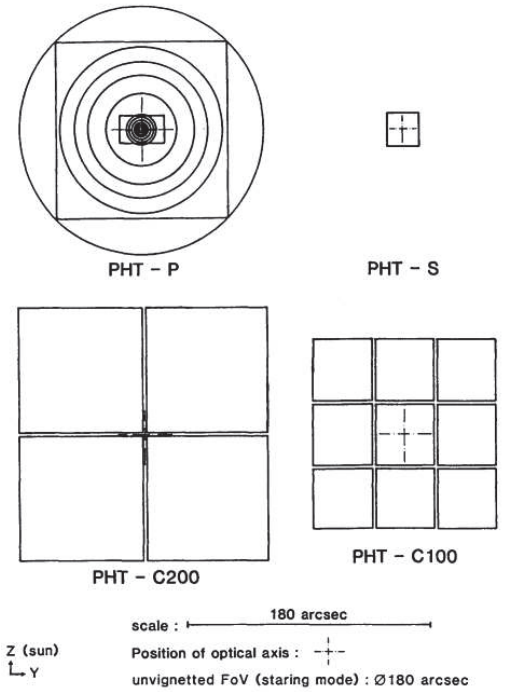

Figure 2.2 Focal plane map of the ISOPHOT instrument, showing relative sizes of the pixels and apertures of the different sub-instruments (Laureijs et al., 2003).

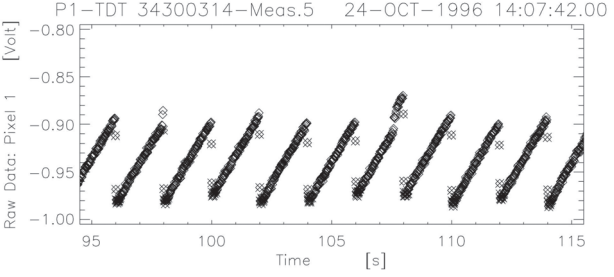

Figure 2.3 Example for Edited Raw Data (ERD).

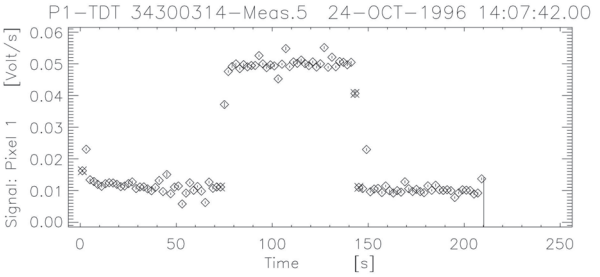

Figure 2.4 Example for Signal Raw Data (SRD).

downloaded from the ISO archive). At this point, no scientific nor instrument-specific processing is yet performed. ERD products are in the form of binary FITS tables. Standard data processing can be divided into three stages (Laureijs et al., 2003):

- *Ramp processing.* ERD files contain the readouts of an integration ramp in V (for an example from the OO Ser observations, see Fig. 2.3). These integration ramps were corrected for non-linearities. Cosmic particle hits were removed using the two thresholds deglitching method. Then, signal values in V/s were derived by fitting a first order polynomial to each ramp. The resulting files are called Signal Raw Data (SRD, Fig. 2.4).

- *Signal processing.* SRD files were further processed (including corrections for instrumental effects and averaging). The signals were transformed to a standard reset interval, then an orbital dependent dark current was subtracted and cosmic ray hits were again checked. In most cases, signals for each chopper plateau were simply averaged. In case the signal did not fully stabilise during the measurement time due to detector transients, only the last part of the data stream was used. This was found mainly in observations with the 12 and 25 μm filters, while at other wavelengths the measurements showed sufficient stability. The resulting files are called Signal per Chopper Plateau (SCP) data (Fig. 2.5).

- *Flux calibration.* In this step, photometric calibration factors are used to convert the signals to flux for the selected filter band. Calibration factors can be determined from

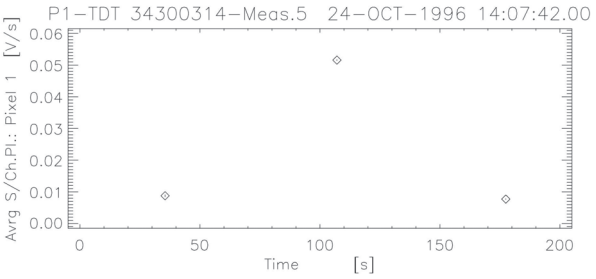

Figure 2.5 Example for Signal per Chopper Plateau Data (SCP).

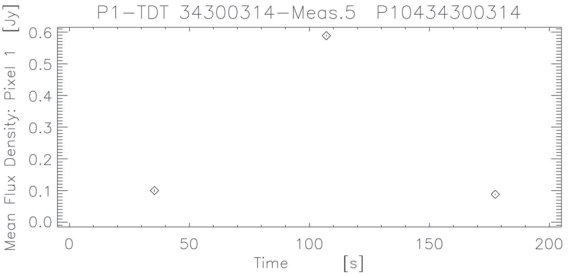

Figure 2.6 Example for Auto Analysis Product Data (AAP).

Fine Calibration Source (FCS) observations, or the default responsivity of the detector can also be used. The absolute flux calibration of the OO Ser measurements at 25 μm and shortwards was done by adopting the default responsivity of the detector. The resulting files are called Auto Analysis Product (AAP) Data (Fig. 2.6). The ISOPHOT Handbook (Laureijs et al., 2003) gives a typical absolute flux uncertainty of 40% at 3.6, 4.8, 12, and 15 μm, and 10% at 25 μm for ON/OFF staring measurements. Since our small raster maps enabled better background subtraction than the ON/OFF mode, the error of our measurements is probably smaller. Nevertheless, we adopted the abovementioned values as conservative estimates for the absolute flux uncertainty (see Col. 9 of Table 2.1).

After flux calibration, Jy values for each chopper plateau are obtained. In the case of OO Ser, most observations (inlcuding the one used as an example in Figs. 2.3-2.6) were small

3×1 raster maps, where the first point is the sky, the second point is the source, and the third point again is the sky. The flux values for these points were read from the AAP files, and the average sky value was subtracted from the source observation.

Relative flux determination at $\lambda \leq 25\,\mu$m. Due to the monitoring strategy, the observations were carried out with identical instrument setup at most epochs. This enabled us to determine relative flux variations at a certain wavelength more accurately than the standard processing by applying a new method developed at Konkoly Observatory especially for the fine relative calibration of ISOPHOT data (Juhász et al., 2007). The algorithm compares the detector transient curves in a measurement sequence with the corresponding curves of a reference day (in our case 1996 October 24) at the SRD level. The method consists of the following steps:

- Calculate a scaling factor between the FCS measurements in the two sequences; scale the whole measurement sequence with this factor (Fig. 2.7, first panel).
- Subtract sky background by fitting a line to the signal points corresponding to the sky position (Fig. 2.7, second panel).
- Calculate a scaling factor between the on-source signal points (Fig. 2.7, third panel).

The advantage of the method is that it works reliably also for unstabilised signal sequences, because it does not attempt to determine stabilised signal level, but uses the complete signal sequence. This can be done because the observational setup is identical and the illumination history is very similar at each epoch. Evaluating all epochs, one obtains a light curve normalized to the reference day. The final fluxes are computed as the product of the scaling factors and the absolute flux level of the reference day. The method provides relative uncertainties, which correspond to the formal errors of the scaling factors. In our case, the relative uncertainties were usually around or below 10% (see Col. 10 of Table 2.1). The absolute flux level of the whole light curve is determined by the absolute calibration of the reference flux.

Far-infrared maps. The far-infrared observations at 60 and 100 μm were processed with PIA in a standard way. PHT32 observations at 170 and 200 μm were reduced using a dedi-

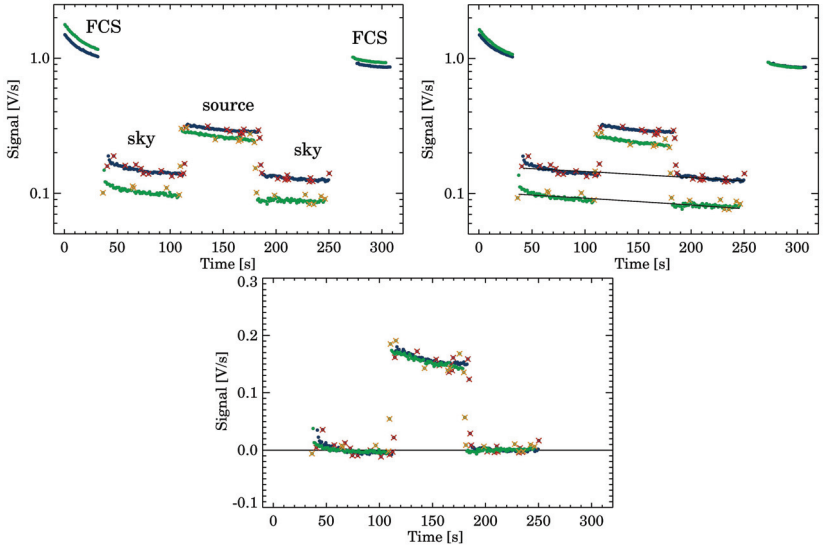

Figure 2.7 *First panel:* original SRD data sequences; *second panel:* scaled data sequences; *third panel:* sky-subtracted data sequences. Blue dots: data from the reference date of 1996 October 24; green dots: data from 1997 April 12. Crossed out data points are not used in the procedure, because they are flagged due to cosmic hits. Solid black lines are the fitted sky levels.

cated software package (P32TOOLS) developed at MPI Kernphysik in Heidelberg (Tuffs & Gabriel, 2003). This tool provides adequate correction for transients in PHT32 measurements. Absolute calibration was done by comparing the source flux with the FCS observations. At 60 and 100 μm each 9×3 map was flat-fielded using the first raster step (3×3 pixel) as the sky flat position. En example for the resulting flat-fielded maps can be seen in Fig. 2.8. Then the sum of two point spread functions, centred on the positions of OO Ser and a nearby submillimeter source, SMM 1 (see Sec. 2.2.7), was fitted to the brightness distribution on the map using the ISOPHOT measured footprint maps. A similar fitting procedure was applied to the PHT32 maps. The errors given in Table 2.1 represent the quadratic sum of the formal uncertainties of the fits (in the range of 3-15%) and the photometric calibration uncertainty of the detector given in the ISOPHOT Handbook (Laureijs et al., 2003). We note that with this technique OO Ser could be separated from SMM 1 but not

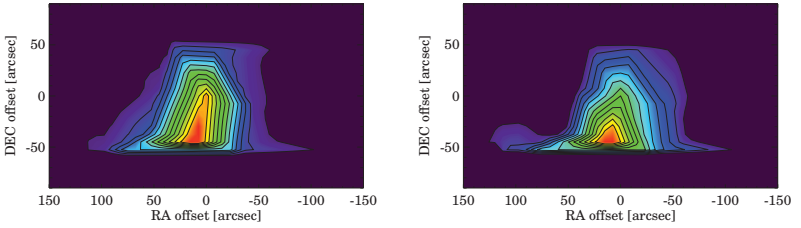

Figure 2.8 Far-infrared maps of OO Ser from 1996 October 24. *Left:* 60 μm; *right:* 100 μm.

from other closer nearby sources, which may contaminate the flux of OO Ser. 9×3 maps at 60 and 100 μm were obtained at 7 different epochs, but the first two measurements (in 1996 February and April) were executed at late orbital phases during ISO's orbit. This caused a large uncertainty in these measurements, thus we decided not to present them. In the PHT32 oversampled maps more than one detector pixel observed OO Ser; their independent photometric results were combined with a robust averaging technique described by Ábrahám et al. (2004a).

ISOPHOT-S spectra. Spectrophotometric observations, also in the form of 3×1 small raster maps centred on OO Ser, were obtained with the ISOPHOT-S subinstrument. The processing of these data deviated from the standard scheme implemented in PIA. ISOPHOT-S has a successful dynamic calibration for staring observations but in PIA this method is not applicable for raster maps, leading to uncorrected transients and consequently reduced photometric accuracy. Since the contrast between OO Ser and the background level is relatively low, we treated these rasters as long staring observations, and applied the dynamic calibration by modifying some PIA routines. The resulting photometric uncertainties are in the range of 5-10%.

Color corrections. Color corrections were applied to each broadband photometric measurement by convolving the observed spectral energy distribution (SED) at a certain epoch with the ISOPHOT filter profile in an iterative way. The result of the ISOPHOT photometry is presented in Table 2.1.

2.2.3 ISOCAM observations and data processing

The 6.7 and 14.3 μm photometry was obtained with the ISOCAM instrument (Cesarsky et al., 1996) on 1997 September 22 (see Table 2.1). The data were reduced with the CAM Interactive Analysis Software v5.0 (CIA, Ott et al., 1997). A dark current correction was applied following the 'VilSpa' method. Glitches were removed using the 'multiresolution median transform'. This efficiently removes glitches based on the fact that glitches in general are much shorter than the signature of a real source. The data were stabilised using the Fouks-Schubert model. Next the individual frames were averaged to four mean images, one for each sky position. After this, a second deglitching was applied based on the overlapping projected sky positions of these mean images. Finally, the images were flat-fielded and combined into the final mosaic. The pixel values were converted to mJy/arcsec^2 using the tabulated conversion factors available in CIA.

Photometry of the sources was obtained using the IRAF tool 'xphot'. We used a small aperture photometry of 4.5″ and 6″ radius for the 6.7 and 14.3 μm mosaic, respectively. These values were then corrected for the flux falling in the wings of the point spread function outside the chosen aperture. The small aperture was selected because of a nearby source (V370 Ser at a distance of $\sim 11''$) which otherwise would have contributed to the measured flux. The results are shown in Table 2.1. The insignificant background level of 1 and 3 mJy/arcsec^2 does not contribute to the measurement error, which should be dominated by the absolute flux calibration uncertainty of 3.3% at 6.7 μm and 4.8% at 14.3 μm (Blommaert et al., 2003).

2.2.4 Near-infrared observations and data processing

K_S-band images were obtained by the LIRIS instrument on 2004 June 11 (as part of the LIRIS Guaranteed Time program) and on 2006 May 6. LIRIS is an infrared camera/spectrograph built at the Instituto de Astrofísica de Canarias (Acosta-Pulido et al., 2003; Manchado et al., 2004), and is mounted on the 4.2 m William Herschel Telescope at the Observatorio del Roque de los Muchachos (Canary Islands). The detector used is a 1024×1024 HAWAII–1 detector (Hodapp et al., 1996a), which provides a plate scale of 0.250 arcsec/pixel and a total area of $4.27' \times 4.27'$. In 2004 a three point dither pattern was used with a total exposure time of 140 s, while in 2006 a five-point dither pattern was used

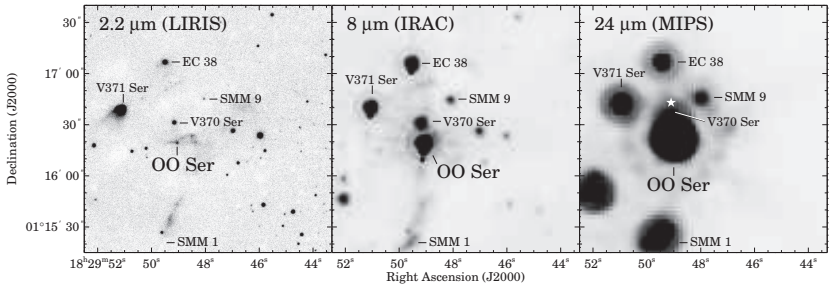

Figure 2.9 OO Ser and its surroundings at different infrared wavelengths. V370 Ser (EC 37), V371 Ser (EC 53), EC 38, SMM 9, and SMM 1 are also marked. In the middle panel, the spots below the brightest sources are instrumental artifacts ('bandwidth effects'). The white star in the right panel indicates the position of IRAS18272+0114 as given in the IRAS Catalogue of Point Sources.

and the total exposure time was 250 s. The images were reduced using the IRAF package 'liris_ql' developed by the LIRIS team within the IRAF environment. The reduction steps consist of flat-fielding, sky subtraction and image co-addition.

In Fig. 2.9 (left) a part of our K_S-band LIRIS image from 2004 can be seen showing the surroundings of OO Ser. The eruptive star was clearly detected in K_S and a faint nebulosity around the star can be seen as well (see also Sec. 2.3.1). Because of this nebulosity, photometry should be done carefully. In order to be able to compare our measurements with those of Hodapp (1999), we used an aperture diameter of 11.3″, the same as Hodapp (1999). Conversion from instrumental magnitudes to real magnitudes was done using the 2MASS J−K_S color versus ΔK_S (the difference between the instrumental and the 2MASS K_S magnitudes) relationship for 20 comparison stars in the field. The resulting values are $K_S = 14.3 \pm 0.2$ mag in 2004 and $K_S = 14.1 \pm 0.2$ mag in 2006. We note that the colors of the 20 comparison stars used in this calibration procedure covered a sufficiently large range to include also the color of OO Ser itself. Similar photometry was derived for some nearby sources (similarly to Hodapp (1999), we used a larger, 11.3″ diameter aperture for the two extended objects: OO Ser and V371 Ser, and a smaller 1.9″ diameter aperture with the corresponding aperture correction for the point-like objects: V370 Ser, EC 38, and SMM 9); the results can be seen in Table 2.2.

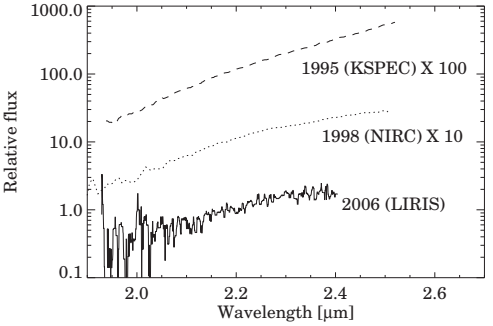

Figure 2.10 Normalised K-band spectra of OO Ser. *Continuous line:* this work, *dashed and dotted lines:* Hodapp (1999). For clarity, we multiplied the spectrum from 1998 by 10 and the spectrum from 1995 by 100.

A K-band spectrum of OO Ser was obtained using LIRIS on 2006 May 6. The observation was performed following an ABBA telescope nodding pattern. The total exposure time was 2400 s, split in 4 individual exposures of 600 s. In order to reduce the readout noise, the measurements were done using multiple correlated readout mode, with 4 readouts before and after the integration. We used a slit width of $1''$ and a medium resolution sapphire grism which yielded a spectral resolution of 2500. The wavelength calibration was provided by observations of an Argon lamp available in the calibration unit at the A&G box of the telescope. In order to obtain the telluric correction, the nearby A0V star HIP 90123 was observed with the same configuration as the object. The data were reduced and calibrated using the package 'liris_ql'. Consecutive pairs of AB two–dimensional images were subtracted to remove the sky background, then the resulting images were wavelength calibrated and flat-fielded before registering and coadding all frames to provide the final combined spectrum. A one dimensional spectrum was extracted with the IRAF 'apall' task. The extracted spectrum was divided by a composite to eliminate telluric contamination. This composite spectrum was generated from the observed spectrum of the calibration star, divided by a stellar model and convolved to our spectral resolution. The resulting normalised K-band spectrum is shown in Fig. 2.10.

2.2.5 Mid-infrared observations and data processing

OO Ser was imaged with TIMMI2 mounted on the ESO 3.6 m telescope at La Silla on 2004 October 21, under clear and stable conditions. The N11.9-OCLI filter was used which has a central wavelength of 11.66 μm and a FWHM of 1.16 μm. The total integration time was 4 minutes. Both chopping and nodding amplitudes were 10″, and the 0.2″ pixel scale of the 240×320 Raytheon detector was set. This resulted in a chop–nod corrected image with two negative and two positive beams captured on the detector. The four beams were used for independent determination of the source flux and error. The resulting fluxes are 0.64 Jy for OO Ser and 0.18 Jy for V370 Ser (a nearby young star is also visible in the field, see also Table 2.2). The flux calibrator was the photometric standard HD 96171 which was observed with the same set-up. Other photometric standard star observations of the same night were inspected to estimate the total absolute flux uncertainty of $\sim 15\%$.

2.2.6 Spitzer observations and data processing

OO Ser was measured with the IRAC and MIPS instruments of the Spitzer Space Telescope on 2004 April 4 and 5, respectively, as part of the legacy program 'c2d' (From Molecular Cores to Planet Forming Disks, PI: Neal J. Evans II). The third data release of this program containing enhanced data products and catalogues can be downloaded from the Spitzer website[2]. As an example we plotted parts of the 8 μm IRAC and the 24 μm MIPS maps in Fig. 2.9.

The 'c2d' catalogue contains IRAC fluxes for OO Ser, but it is treated as a point source. The nebulosity seen in the K-band images, however, are still visible at 3.6 and 4.5 μm too. In order to be able to compare the IRAC fluxes with the ISO measurements, we decided to extract fluxes from the IRAC images for OO Ser using the same apertures as ISOPHOT used (diameter of 13.8″ at 3.6 μm and 18″ at $\geq 4.5\,\mu$m)

The current version of the 'c2d' catalogue does not contain MIPS fluxes yet. In order to obtain photometry in the MIPS bands, we downloaded the enhanced MIPS images. At 24 μm we selected 7 isolated stars to construct the point spread function. Since OO Ser was saturated, this profile was then fitted to the non-saturated wings of OO Ser. At 70 μm

[2]http://ssc.spitzer.caltech.edu/legacy/all.html

λ [μm]	Date	Instrument	OO Ser	V370 Ser	V371 Ser	EC 38	SMM 9
2.2	2004 Jun 11	LIRIS	1.16 ± 0.20	2.25 ± 0.39	3.76 ± 0.57	5.64 ± 0.95	0.13 ± 0.02
2.2	2006 May 6	LIRIS	1.54 ± 0.26	2.85 ± 0.44	1.60 ± 0.22	4.82 ± 0.70	0.15 ± 0.02
3.6	2004 Apr 4	IRAC	7 ± 1	17 ± 1	10 ± 1	43.4 ± 0.4	1.9 ± 0.2
4.5	2004 Apr 4	IRAC	82 ± 2	38 ± 1	17 ± 1	101 ± 1	3.1 ± 0.2
5.8	2004 Apr 4	IRAC	81 ± 4	63 ± 1	140 ± 2	139 ± 1	12.4 ± 0.7
8.0	2004 Apr 4	IRAC	570 ± 20	86 ± 2	190 ± 6	162 ± 2	14.4 ± 0.4
12	2004 Oct 21	TIMMI2	640 ± 100	180 ± 30	-	-	-
24	2004 Apr 5	MIPS	13 300 ± 1 800	1 560 ± 60	1 010 ± 20	530 ± 10	227 ± 10
70	2004 Apr 5	MIPS	14 000 ± 600	900 ± 600	7 900 ± 220	5 200 ± 1 400	13 400 ± 4 000

Table 2.2 Log of observations from 2004–2006. All fluxes are presented in mJy. Spitzer fluxes are from the third delivery of data from the 'c2d' legacy project, except the 70 μm data of all sources and the 3.6, 4.5, 5.8, 8, and 24 μm data of OO Ser, which were extracted by us from MIPS and IRAC images improved and published by the 'c2d' legacy team. All Spitzer fluxes are color corrected.

OO Ser and a nearby young star, V370 Ser could not be fully separated. Thus an aperture of 20″ was utilized, which included both objects. The measured flux was then distributed between OO Ser and V370 Ser in the same ratio as their peak brightnesses (measured in a 5″ aperture at the position of the two sources). We also extracted 70 μm photometry for some other sources in the vicinity of OO Ser, since they possibly cause source confusion in IRAS and ISO far-infrared measurements. In these cases, a 20″ aperture was utilized with a fixed 0.142 Jy background.

Color corrections were applied to each measurement for each source by convolving the observed SED with the IRAC and MIPS filter profiles in an iterative way. The resulting fluxes and estimated uncertainties can be seen in Table 2.2.

2.2.7 Source confusion

Fig. 2.9 shows that several infrared and submillimeter sources are present in the vicinity of OO Ser: V370 Ser (also known as EC 37), V371 Ser (also known as EC 53 or SMM 5), EC 38, SMM 9, and SMM 1. At shorter wavelengths (2.2, 3.6, 4.5, and 5.8 μm), an extended nebulosity can also be seen around OO Ser. Thus, when comparing the fluxes of OO Ser measured with different instruments one has to keep in mind that – to some extent – the nebulosity and some of the abovementioned sources may contribute to the observed flux at a particular wavelength. At 2.2 μm and with the ISOPHOT/ISOCAM at 3.6, 4.8, 6.7, and 14.3 μm the beam included OO Ser only. At 12, 15, and 25 μm the ISOPHOT beams included OO Ser and V370 Ser. At 60, 100, 170, and 200 μm the fluxes extracted for OO Ser include

also contributions from V370 Ser, V371 Ser, EC 38, and SMM 9. Recent infrared photometry for these sources can be seen in Table 2.2. It should be noted that fluxes presented in Table 2.1 contain the contributions of nearby sources as discussed above. In Sec. 2.3.4 we give a detailed description of how we corrected the ISOPHOT measurements for the effects of source confusion.

2.3 Results

2.3.1 Morphology of the nebula

According to Hodapp (1999) before the outburst a triangle-shaped nebula west of OO Ser and a small elongated nebula east of OO Ser could be seen (Fig. 2.1, left). During the outburst these – presumably reflection – nebulae became much brighter (Fig. 2.1, right). In this phase Hodapp et al. (1996b) observed OO Ser in the L′ and M′ bands, as well as at 11.7 and 20.6 μm. They found that the nebulosity can be seen in the L′ but not at longer wavelengths. Our recent K_S-band images reveal that the nebulae still exist and look very similar to the preoutburst image of Hodapp (1999) (compare Fig. 2.1 left and Fig. 2.9 left). The nebulosity around OO Ser is also visible in the Spitzer/IRAC maps from 2004 at 3.6, 4.5, and 5.8 μm and some extended emission can be suspected even at 8 μm.

2.3.2 Preoutburst fluxes

In order to study the consequences of the outburst in the whole infrared regime, one has to compile first the SED of OO Ser in the quiescent phase, i.e. estimate the preoutburst fluxes. At 2.2 μm there exists a preoutburst measurement from 1994 (Hodapp et al., 1996b). At longer wavelengths, only the IRAS measurements are available from 1983. Analysing high-resolution IRAS maps, Hurt & Barsony (1996) derived fluxes of 0.63, 4.5, 24, and 111 Jy at 12, 25, 60, and 100 μm respectively. The authors claim that these values represent the total fluxes from a region encompassing three confused sources: OO Ser, V371 Ser, and SMM 9, and they give the one third of the abovementioned values as upper limits for the brightness of OO Ser. The position of IRAS18272+0114 from the IRAS Catalogue of Point Sources (marked by a white star in Fig. 2.9 right) is located halfway between the sources, which may

indicate that there was no dominant source, but all sources had comparable contributions to the IRAS flux.

With the help of Spitzer/MIPS measurements, it is possible to check the validity of the assumption of Hurt & Barsony (1996) via estimating the preoutburst fluxes of OO Ser at 25 and 60 μm. Assuming that EC 38 and SMM 9 have non-variable far-infrared fluxes, we subtracted the contribution of these sources from the IRAS values cited above. Another nearby source, V371 Ser, exhibits near-infrared variability of ≈ 1.5 mag and shares many characteristics with EXors (Hodapp, 1999). At far-infrared wavelengths, however, eruptive young stars do not typically show significant flux changes (Ábrahám et al., 2004a). Thus we assumed that V371 Ser is also non-variable at 25 and 60 μm, at least within our measurement uncertainties, and we subtracted its flux from the IRAS values. In practice, we estimated 25 μm fluxes for these nearby sources via interpolating from the 24 μm MIPS values in Table 2.2, and subtracted the sum of these (3.6 Jy) from the value given by Hurt & Barsony (1996) (4.5 Jy). The result is 0.9 Jy, which is indeed of the order of one third of 4.5 Jy. The result at 60 μm is also roughly consistent with the one third value. Due to the lack of recent 12 or 100 μm data for all nearby sources, the same test cannot be done at these wavelengths. Therefore, for homogeneity, at all four IRAS wavelengths we adopted as preoutburst fluxes the one third values within a factor of 2 uncertainty: $0.21^{+0.21}_{-0.10}$ Jy at 12 μm, $1.5^{+1.5}_{-0.8}$ Jy at 25 μm, 8^{+8}_{-4} Jy at 60 μm, 37^{+37}_{-19} Jy at 100 μm. We note that OO Ser is the first eruptive young star whose preoutburst fluxes are available in the whole infrared wavelength regime. Similar preoutburst data can be found only for one other young eruptive star, V1647 Ori (Ábrahám et al., 2004b).

2.3.3 Spectral energy distribution

In Fig. 2.11 the SED of OO Ser in the high (outburst) state from 1996 September is plotted with filled symbols. We attempted to correct for the effects of source confusion as described in details in Sec. 2.3.4. Thus, the resulting SED in Fig. 2.11 represents the flux from OO Ser alone at ≤ 60 μm. Due to high extinction the star is invisible at optical wavelengths and is very faint in the near-infrared regime. In the mid-infrared (3$-$25 μm) the SED is rising towards longer wavelengths. This wavelength regime is zoomed in Fig. 2.12, showing a broad

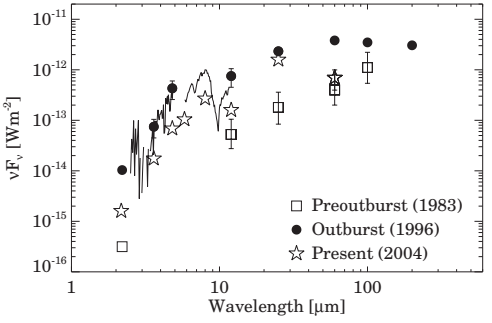

Figure 2.11 Spectral energy distribution of OO Ser. *Squares*: preoutburst fluxes measured with IRAS in 1983 (Hurt & Barsony, 1996), and K-band photometry from 1994 August, (Hodapp et al., 1996b); *Dots and line*: outburst fluxes from 1996 September, measured with ISOPHOT; *Stars*: current fluxes from 2004, measured with LIRIS, TIMMI2, and Spitzer. Error bars smaller than the symbol size are not plotted. ISOPHOT beams at 100 and 200 μm contained nearby sources; for a detailed discussion see Sec. 2.2.7 and 2.3.3.

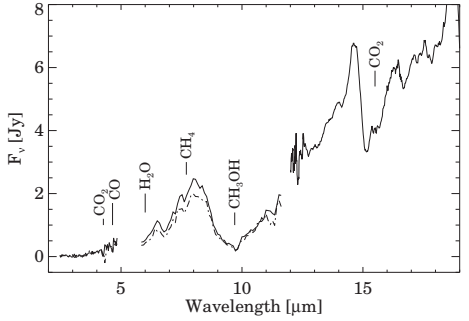

Figure 2.12 Ice features in the spectrum of OO Ser. Data below 12 μm were taken by ISOPHOT-S. Solid line indicates data from 1996 October, dash-dotted line from 1997 April. Data above 12 μm were taken by the ISO-SWS instrument (highly processed data products from Frieswijk et al., 2004). In order to obtain high signal-to-noise ratio, ISO-SWS spectra from 1997 March, April, and September were averaged and a 0.3 μm wide moving median window was applied.

silicate absorption feature at 9.7 μm, as well as several ice features, which also indicate high extinction. Measuring the optical depth of the 9.7 μm feature, and converting it to visual extinction assuming $A_V/\Delta\tau_{9.7} = 18.5$ (Draine, 2003), we obtained $A_V = 42 \pm 5$ mag. This value is twice as large as the one measured by Larsson et al. (2000); the difference is probably related to the low signal-to-noise of his SWS spectra around the 9.7 μm absorption feature. The measured high extinction indicates that OO Ser is more deeply embedded than most FUors. At far infrared wavelengths (60−200 μm) the SED is flat, but it should be noted that data points at 100 and 200 μm are contaminated by source confusion (see Sec. 2.2.7).

In Fig. 2.11 the preoutburst SED (see Sec. 2.3.2) and the present SED (based on measurements from 2004) are also plotted. They will be discussed in Sec. 2.3.4.

2.3.4 Light curves

ISOPHOT, ISOCAM, LIRIS, TIMMI2, Spitzer, IRAS (Hurt & Barsony, 1996), and K-band measurements (Hodapp et al., 1996b; Hodapp, 1999) were combined to construct the light curves of OO Ser at different wavelengths between 1995 and 2006.

For the subsequent light curve analyses, we attempted to correct for the effects of source confusion. One possibility would be to smooth all data to the same resolution, in most cases defined by the ISOPHOT aperture. In doing so, however, several additional sources would be included in the beam, falsifying the fading rate calculations for OO Ser. Instead, we decided to use the higher spatial resolution images to correct for the contribution of additional, unrelated sources in the large ISOPHOT beams.

At 12 μm TIMMI2 could resolve OO Ser and V370 Ser. Assuming that V370 Ser is not variable at this wavelength, we subtracted its contribution of 0.18 Jy (see Table 2.2) from each ISOPHOT 12 μm measurement. The MIPS camera of Spitzer at 24 μm could separate OO Ser from V370 Ser giving a flux of 1.56 Jy for the latter source, which we interpolated to 25 μm (1.71 Jy) and subtracted from the ISOPHOT points at 25 μm. At 60 μm, MIPS 70 μm measurements could be utilized. Using the SEDs presented in Table 2.2, we interpolated 60 μm fluxes for V370 Ser, V371 Ser, EC 38, and SMM 9, and subtracted the sum of these values (24 Jy) from the ISOPHOT 60 μm data points. Due to the lack of 100 μm fluxes for the nearby sources, a similar correction was not possible in the case of the 100 μm ISOPHOT

light curve.

In Fig. 2.13 six representative light curves between 2.2 and 60 μm are shown. All these light curves are corrected for source confusion and represent the brightness evolution of OO Ser alone. In the following, we describe these light curves in detail.

The outburst history at 2.2 μm

FUor and EXor ourbursts were historically monitored at optical wavelengths. Since OO Ser is invisible in the optical, K_S is the shortest available band where the outburst could have been followed. The top left panel of Fig. 2.13 shows the 2.2 μm light curve of OO Ser. The star brightened by 4.6 mag between 1994 August and 1995 July. After reaching peak brightness, it started an approximately exponential fading with a rate of 1.00 mag/year in the first 350 days and 0.34 mag/year afterwards, as the data between 1995 and 1999 indicate (Hodapp, 1999). The change in fading rate divides this period of the outburst into a first and a second part. Our measurements from 2004−2006 prove that the fading continued, although at a slightly different rate, representing a third part of the fading. Comparing the preoutburst flux with the new observations, one can conclude that OO Ser is still above the preoutburst flux level at 2.2 μm.

In the following, we describe the lightcurves of OO Ser at longer wavelengths, following the abovementioned division: the initial rise (until peak brightness); the first part of the fading (until mid-1996); the second part of the fading (until mid-1997); and the third part of the fading (until 2004).

The initial rise (until peak brightness)

Comparison of the preoutburst fluxes with the SED in outburst (Fig. 2.11) shows that the eruption caused brightening in the whole near- to far-infrared spectrum. Though the fluxes at 100 μm are contaminated by nearby sources, there is a flux change at this wavelength, too. The shape of the SED changed significantly: the outburst SED is flatter.

At 2.2 μm the light curve reached its peak in 1995 October. At 3.6, 4.8, and 12 μm, the exact date of the peak is not known, but it happened not later than 1995 October, thus it was probably simultaneous with the K-band peak. At 25 μm, however, the peak took place

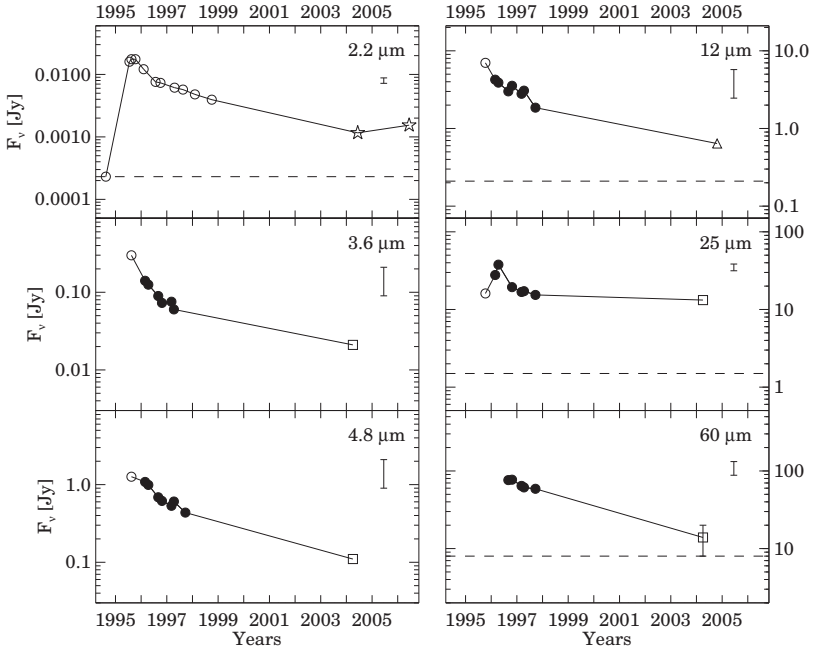

Figure 2.13 Light curves of OO Ser at different wavelengths. *Open circles:* measurements of Hodapp et al. (1996b); Hodapp (1999); *Stars:* LIRIS; *Filled circles:* ISOPHOT; *Triangle:* TIMMI2; *Squares:* Spitzer; *Dashed lines:* preoutburst fluxes from 1994 at 2.2 μm and from 1983 at 12, 25, and 60 μm (for details see Sec. 2.3.2). Tick marks indicate January 1 of the corresponding year. Error bars in the upper right corner of each panel show the typical uncertainty in the absolute flux level. Due to the homogeneous measurement strategy, the uncertainties of the ISOPHOT data points relative to each other at a certain wavelength are usually better than the absolute errors (see Sec. 2.2.2). All fluxes are corrected for source confusion (for a detailed description see Sec. 2.2.7 and 2.3.4), thus these light curves show the brightness evolution of OO Ser alone.

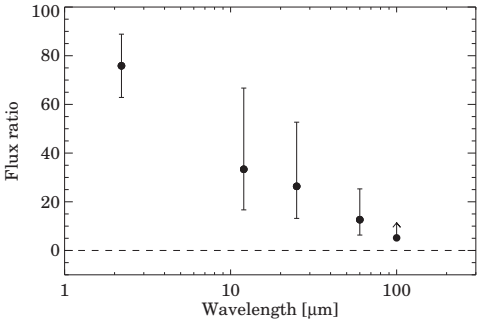

Figure 2.14 Initial rise: flux ratio of peak brightness to preoutburst brightness at each wavelength. (See discussion in Sec. 2.3.4.)

in 1996 April, i.e. some 200 days later than at 2.2 μm. The shape of the peak at 25 μm is also different, it is broader than at 2.2 μm, and has a triangle-like shape. At 60 and 100 μm, the photometry is more uncertain, thus the peak dates cannot be determined. Nevertheless, the time-shift at 25 μm gives a hint that the peak brightness happened gradually later at longer wavelengths. To our knowledge, such a time-shift has not been observed for other eruptive stars.

In order to analyse the wavelength dependence of the brightening, in Fig. 2.14 we plotted the ratio of the peak flux to the preoutburst value at 2.2, 12, 25, 60, and 100 μm. Since at 100 μm both the preoutburst IRAS flux and the peak ISOPHOT flux include contributions from several nearby sources, the ratio derived from these numbers represents a lower limit for the brightening of OO Ser itself. Figure 2.14 suggests that the amplitude of the flux increase has a characteristic wavelength dependence: the flux ratio is lower at longer wavelengths, with an approximately linear dependence on $\log \lambda$. Although the peak brightness did not occur simultaneously at different wavelengths, this trend can also be seen if one compares in Fig. 2.11 the preoutburst SED with its counterpart from 1996 September (close to peak brightness). We note that this result is different from the case of another young eruptive star, V1647 Ori, where the initial rise was practically wavelength-independent (Ábrahám et al., 2004b; Muzerolle et al., 2005).

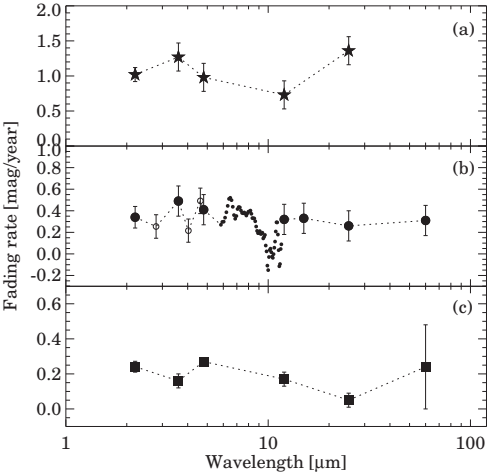

Figure 2.15 Fading rates of OO Ser at different wavelengths, (a) between 1996 April and 1996 September, (b) between 1996 October and 1997 March, (c) between 1997 April and 2004.

The first part of the fading (until mid-1996)

During the first year after peak brightness, OO Ser exhibited similar exponential fading at all wavelengths. This can be quantified by fitting a linear relationship to the first part of the light curves plotted logarithmically in Fig. 2.13, using data taken only after peak brightness at a given wavelength. The derived fading rates are displayed in Fig. 2.15 (a). This graph shows that the fading rate during this period was approximately 1.0 ± 0.3 mag/year irrespectively of wavelength in the whole mid-infrared regime.

The second part of the fading (until mid-1997)

The second part of the light curves (between 1996 October and 1997 September) can be characterised by fading rates of 0.35 ± 0.10 mag/year, similar at all wavelengths from 2.2 to 60 μm (Fig. 2.15 (b)). This is approximately three times slower than the fading during the first part. In this period ISOPHOT-S spectra were also obtained, which give the opportunity to analyse the fading with high wavelength resolution. In order to increase the signal-to-noise ratio, the fitted fading rates of ISOPHOT-S were binned (in the case of the short wavelength

channels) or smoothed (in the case of the long-wavelength channels). The resulting values are overplotted with small open or filled dots in Fig. 2.15 (b), respectively. These values also support a wavelength-independent fading, characteristic of the second part of the outburst (except where the emission of OO Ser is strongly reduced by the silicate absorption around 10 μm, introducing a large uncertainty in the fit).

The third part of the fading (until 2004)

New measurements from 2004 revealed that the fading monitored by ISOPHOT continued at all wavelengths after 1997. We calculated fading rates for the period 1997–2004. The resulting numbers, which are plotted in Fig. 2.15 (c), are even lower than those for the second part and they also show no wavelength dependence. The values are in the range of 0.19 ± 0.08 mag/year.

The present status of OO Ser

In Fig. 2.13 the preoutburst fluxes (marked by dashed lines) can be compared with the latest measurements from 2004-2006. This comparison reveals that OO Ser was still above the preoutburst state in the whole infrared wavelength regime in 2004, indicating that the outburst had not finished yet. The same conclusion can be drawn from Fig. 2.11 if one compares the SED from 1996 with that from 2004.

In Fig. 2.13 the last K-band photometric point from 2006 seems to deviate from a linear extrapolation of the preceding fading, possibly indicating a fourth phase of the outburst with very slow flux change. Extrapolating the lightcurves using the rates calculated for the third part of the fading (1997–2004), the expected end date of the outburst is $\approx$2011 from both the 2.2 μm and the 12 μm lightcurves. The slowing down of the fading process, however, may delay this event even well beyond 2011.

2.3.5 K-band spectral evolution

Figure 2.10 displays our K-band spectrum from 2006, together with the outburst spectra from 1995 and 1998 (Hodapp, 1999). All three spectra are taken with comparable slit widths and were normalised to their value at 2.4 μm. In general, all spectra show a steep continuum,

rising towards longer wavelengths. No individual absorption or emission lines can be seen, even in quiescence. The overall shape of the three spectra is very similar, though there is a tendency that later spectra are less steep.

2.4 Discussion

2.4.1 The outburst

OO Ser offers a unique possibility to investigate the long-term behaviour of an eruptive young stellar object. The rise time of OO Ser was 8.5 months at the longest (Hodapp et al., 1996b), similar to the typical timescale of "fast" FUor outbursts (e.g. the outburst of FU Ori or V1057 Cyg, which was modeled by a triggered eruption, see Bell et al., 1995).

As discussed in Sec. 2.3.4, the fading rate abruptly decreased 350 days after the maximum brightness. A similar event was observed in the case of V1057 Cyg (Kenyon & Hartmann, 1991) too, but there the transition happened later, about 1300 days after the maximum. Using the light curves of Kenyon & Hartmann (1991) we computed fading rates for V1057 Cyg and compared them with corresponding values of OO Ser. We found that both before and after the transition, the fading of OO Ser (1.00 mag/yr before, 0.35 mag/yr after) was significantly faster than that of V1057 Cyg (0.09...0.40 mag/yr before, 0.04...0.14 mag/yr after, between 0.44 and 21 μm).

From the 2.2 μm light curve in Fig. 2.13 we can conclude that the object will return to the quiescent phase some time after 2011. This implies that the duration of the outburst of OO Ser will be at least 16 years. This timescale differs both from that of FUors (being several decades or a century) and that of EXors (being some weeks or months), suggesting that OO Ser is a young eruptive object that differs from both FUors and EXors.

The magnitude of the luminosity change during outburst is another argument in favour of OO Ser being different from FUors or EXors. From Fig. 2.11 we could estimate a bolometric preoutburst luminosity of $L_{pre} = 4.5 \pm 1.5 L_{\odot}$ for OO Ser and from the ISOPHOT data we also computed luminosities for OO Ser for the different epochs during the outburst. Since the far-infrared fluxes are contaminated by nearby sources, we calculated an upper and a lower limit for the luminosity, by including or neglecting the 100−200 μm data points,

respectively. Adopting the 1996 February values of $L_{peak} = 26 \ldots 36 L_{\odot}$ as a representative outburst luminosity range, OO Ser changed its luminosity by a factor of about $6 \ldots 8$. Thus one may conclude that both the peak brightness and the amplitude of the luminosity increase were significantly lower than the corresponding values of classical FUors ($\sim 100\, L_{\odot}$ and a factor of 100, see Hartmann & Kenyon, 1996).

We note that there exists another star, V1647 Ori, which seems to share some characteristics of OO Ser. Based on the amplitude of its brightening, V1647 Ori was classified as an intermediate-type object between FUors and EXors by Muzerolle et al. (2005). Preoutburst and outburst luminosities of V1647 Ori are $L_{pre} = 5.6\, L_{\odot}$ (Ábrahám et al., 2004b) and $L_{peak} = 44\, L_{\odot}$ (Muzerolle et al., 2005), respectively, thus its luminosity changed by a factor of about 8, similarly to OO Ser. The timescales of their outbursts are somewhat different, because the eruption of V1647 Ori was only 2 years long (Kóspál et al., 2005) and it also produced an outburst in the 1960s (Aspin et al., 2006).

We speculate, following Hodapp et al. (1996b), that OO Ser (and in some respects V1647 Ori) may be the representative of a new class of young eruptive stars ("Deeply Embedded Outburst Star" or DEOS in Hodapp et al., 1996b). Members of this class may be defined by their relatively short timescales compared to FUors, possibly recurrent outbursts, modest increase in bolometric luminosity and accretion rate, and an evolutionary state earlier than that of typical FUors or EXors (see Sec. 2.4.2).

2.4.2 The evolutionary stage of OO Ser

Based on optical to millimeter measurements available at that time, Hodapp et al. (1996b) claimed that the SED of OO Ser appeared consistent with that of a Class I source and assumed its age to be 10^5 yr, indicating that OO Ser is in a very early evolutionary phase. The new data presented in this chapter make it possible to reestablish the evolutionary stage of the source, using the method presented in Chen et al. (1995). They calculated bolometric temperatures and bolometric luminosities for 235 YSOs in the Taurus and Ophiuchus star-forming regions. They define the bolometric temperature and luminosity as follows:

$$T_{\rm bol} = \frac{\zeta(4)}{4\,\zeta(5)} \frac{h\bar{\nu}}{k} = 1.25 \times 10^{-11} \bar{\nu} \left({\rm K\,Hz^{-1}} \right)$$

and

$$L_{\rm bol} = 4\pi D^2 \int_0^\infty F_\nu d\nu,$$

where F_ν is the flux density at frequency ν, $\zeta(n)$ is the Riemann zeta function of argument n, h is Planck's constant, k is Boltzmann's constant, D is the source distance, and the mean frequency $\bar{\nu}$ is the ratio of the first and zeroth moments of the source spectrum:

$$\bar{\nu} = \int_0^\infty \nu F_\nu \Big/ \int_0^\infty F_\nu d\nu.$$

They plotted their 235 sources in a bolometric luminosity-temperature diagram (Fig. 2.16 and found that $T_{\rm bol}$ correlates well with the age inferred from the evolutionary models of pre-main sequence stars and protostars. We followed this method and computed the bolometric temperature for the preoutburst, outburst and present SEDs. Due to the uncertainty of the far-infrared data points (see Sec. 2.2.7 about source confusion), we calculated $T_{\rm bol}$ in two different ways, with and without data points affected by source confusion ($60 < \lambda < 800\,\mu$m). The resulting values are in the range of 50 – 120 K for all three SEDs (within a range indicated by the grey square in Fig. 2.16). Within this interval, the bolometric temperature slightly increased, and the luminosity changed by a factor of 7 during the outburst. We compared these values with the distribution of corresponding values among young stellar objects in the Taurus and Ophiuchus star forming regions (Chen et al., 1995, see also Figs. 2.16 and 2.17). From this check we can conclude that OO Ser seems to be an early Class I object, and its age is $< 10^5$ yr.

2.4.3 Structure of the circumstellar environment

The circumstellar environment of young eruptive stars is usually modeled with a flat or flared accretion disk and an extended infalling envelope (e.g. Kenyon & Hartmann, 1991; Turner et al., 1997). In these models the emission of the central source (the star and the innermost part of the accretion disk) dominates the emission at optical and near-infrared wavelengths. Between 3 and 10 μm the origin of the emission is the release of accretion

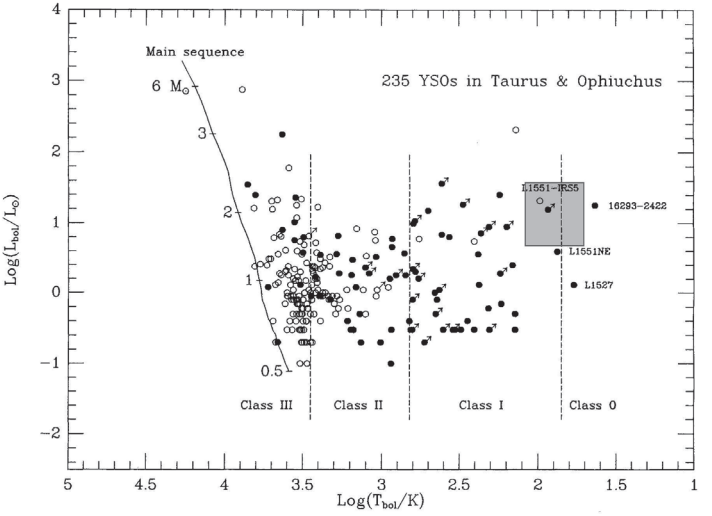

Figure 2.16 Bolometric luminosity-temperature diagram for 235 YSOs in Taurus and Ophiuchus (Chen et al., 1995). The grey square indicates the approximate position of OO Ser.

energy in the disk, and also starlight reprocessed in the same part of the disk and also in the envelope. The emission at $\lambda > 10\,\mu$m is starlight reprocessed in the envelope. The outburst occurs when, due to thermal instability in the inner edge of the disk, the accretion rate suddenly increases. After peak brightness, the accretion slowly relaxes to its quiescent value. The decreasing accretion rate causes the fading of the central source and consequently leads to the simultaneous fading of the reprocessing envelope. Thus, this model predicts a wavelength-independent fading of the source in the whole optical to mid-infrared regime (see e.g. V1057 Cyg in Ábrahám et al. 2004a and V1647 Ori in Acosta-Pulido et al. 2007).

The circumstellar environment of OO Ser probably shares many properties with the abovementioned models, except that the unusually high extinction indicates a larger and/or denser envelope. As it can be seen in Fig. 2.15, the fading of OO Ser was indeed wavelength-independent in the whole near- to mid-infrared wavelength regime, in agreement with the model predictions. This, together with the overall shape of its SED and the ice features in its mid-infrared spectrum indicates that the circumstellar structure of OO Ser is similar

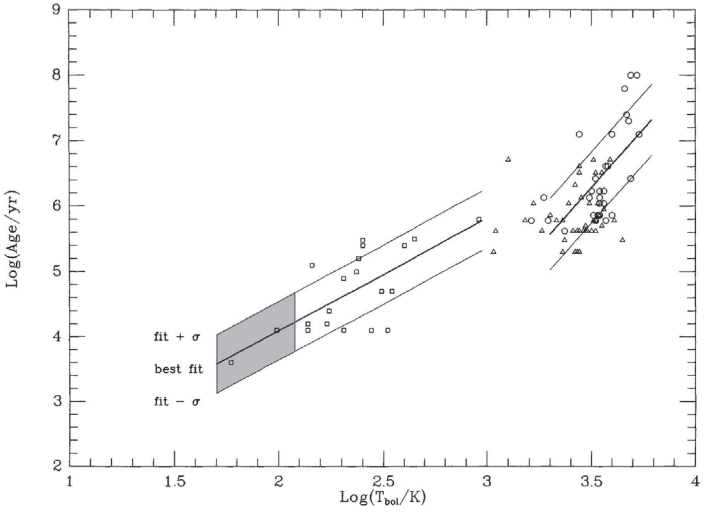

Figure 2.17 Age estimate of YSOs from their bolometric temperatures (Chen et al., 1995). The grey area indicates the approximate position of OO Ser.

to those of other young eruptive stars, i.e. possesses a circumstellar accretion disk and is embedded in a dense circumstellar envelope.

2.4.4 Viscosity

Bell & Lin (1994) modeled FUor outbursts as self-regulated accretion events in protostellar accretion disks. In this model the rise time of the outburst, the subsequent high state and the time between successive outbursts are dependent on α, the viscosity parameter in the model of Shakura & Sunyaev (1973). Fitting their model to the observed FUor timescales, Bell & Lin (1994) derived $\alpha_c = 10^{-4}$ for the α value in the cool, neutral state, and $\alpha_h = 10^{-3}$ in the hot, ionised state. Since OO Ser is similar to FUors in many respects, the model of Bell & Lin (1994) might be applicable, although the timescales of the OO Ser outburst are remarkably shorter than those of FUors. Thus, applying this model to OO Ser requires different parameters than those for FUors. Bell & Lin (1994) give in their Table 2 the dependence of different timescales on α, from which we can estimate $\alpha_h = 10^{-2}$ for OO Ser.

This is one order of magnitude larger than the usual value for FUors, which implies that OO Ser may differ from classical FUors in a way that its disk has different, one order of magnitude higher viscosity.

2.5 Summary and conclusions

In this chapter we presented an infrared monitoring program on OO Ser, a deeply embedded young eruptive star in the Serpens NW star-forming region. OO Ser went into outburst in 1995 and has been gradually fading since then. Our infrared photometric data obtained between 1996 and 2006 revealed that the fading of the source is still ongoing in the whole infrared wavelength regime, and that OO Ser will probably not return to quiescent state before 2011. The flux decay has become slower since the outburst peak and has been practically wavelength-independent.

From these results we draw the following conclusions:

- The outburst timescale and the moderate luminosity suggest that OO Ser is different from both FUors and EXors, and shows some similarities to the recently erupted young star V1647 Ori.

- Based on its SED and bolometric temperature, OO Ser seems to be an early Class I object, with an age of $< 10^5$ yr. As proposed by outburst models, the object is probably surrounded by an accretion disk and a dense envelope. This picture is also supported by the wavelength-independence of the fading.

- Due to the shorter timescales, outburst models developed for FUors can only work for OO Ser if the viscosity parameter in the circumstellar disk, α, is set to an order of magnitude larger value than usual for FUors.

Chapter 3

The 2004–2006 Outburst and Environment of V1647 Orionis

On 2004 January 23, the amateur astronomer Jay McNeil discovered a new nebula towards the Orion B molecular cloud, close to the diffuse nebulosity Messier 78. Later, the designation V1647 Ori has been given to the variable star associated with the nebula. The recent outburst of the young star V1647 Ori offered a rare opportunity to study phenomena accompanying the eruption of a low-mass pre-main sequence star. Following a 3-month brightening of $\Delta I_C \sim 4.5$ mag (Briceño et al., 2004), V1647 Ori reached peak light in January 2004, illuminating also a conical reflection nebulosity called McNeil's Nebula (McNeil et al., 2004). The object stayed in high state for about 2 years, then started a rapid fading in October 2005 (Kóspál et al., 2005). V1647 Ori exhibited already a similar eruption in 1966–67 (Aspin et al., 2006).

During the 2004–2005 outburst V1647 Ori was intensively studied from many aspects. The brightness evolution at optical and near-infrared wavelengths was monitored by Briceño et al. (2004), Reipurth & Aspin (2004), Walter et al. (2004), McGehee et al. (2004), and Ojha et al. (2005, 2006). The optical/infrared spectrum, and its changes were studied by Vacca et al. (2004), Walter et al. (2004), Andrews et al. (2004), Rettig et al. (2005), Ojha et al. (2006), and Gibb et al. (2006). The structure of the circumstellar matter and the physics of the outburst were investigated by McGehee et al. (2004), Muzerolle et al. (2005), and Rettig et al. (2005). The X-ray properties of the star were studied by Grosso et al.

(2005), Kastner et al. (2004), and Kastner et al. (2006). These works produced a wealth of very important information on the eruption, but a general picture is still to be worked out. Nevertheless, all authors seem to agree in that: V1647 Ori is a deeply embedded low-mass pre-main sequence object; it is surrounded by a disk; the outburst was caused by increased accretion; and that the eruption was accompanied by strong stellar wind. It is still an open question whether V1647 Ori belongs to the FUor or the EXor class, and whether the standard outburst models, developed for FU Orionis events, could be applied for this case (or how should they be modified to make them applicable).

I was a member of a group who studied V1647 Ori right from the beginning of its outburst. As a first step we collected and analysed the quiescent state data available in the literature and published the results in Ábrahám et al. (2004b). Then we submitted a Director's Discretionary Time proposal to ESO and observed V1647 Ori with MIDI, the mid-infrared interferometer at the VLTI. The results (the visibilities and the SED were modeled together) are presented in Ábrahám et al. (2006). In addition, during the whole outburst we monitored the brightness evolution of the object.

The data, which include optical (V, R_C, I_C) and near-infrared (J, H, K_S) imaging, and intermediate-resolution optical and near-infrared spectroscopic observations, were obtained between 2004 February and 2006 September, covering the whole outburst period. A particularly important part of the light curve, when the star suddenly faded, was first reported in Kóspál et al. (2005). I was personally involved in performing many observations at Piszkéstető, and also in the data reduction. I actively contributed to many aspects of the analysis and discussion of the optical and infrared data, too. In this chapter I present mainly these aspects of our work.

3.1 Observations and data reduction

3.1.1 Optical imaging and photometry

Optical observations of V1647 Ori were obtained on 45 nights in the period 2004 February 12 – 2006 February 1. The measurements were performed in two observatories with three telescopes: the IAC–80 telescope of the Teide Observatory (Spain), and the 1 m Ritchey-

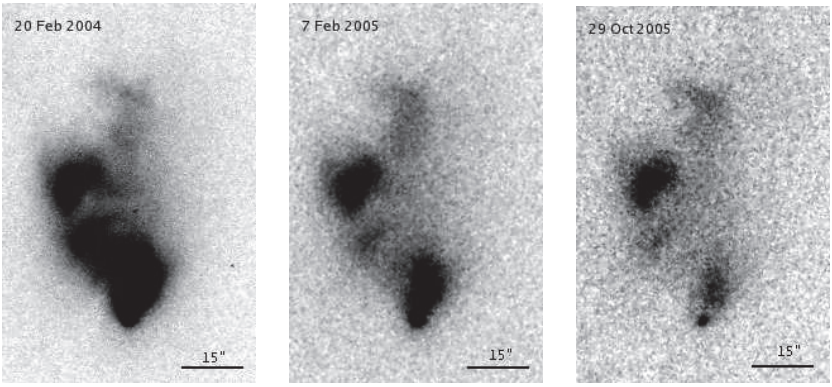

Figure 3.1 Examples of R-band optical images of V1647 Ori taken with the 1 m RCC telescope of the Konkoly Observatory at three different phases of the outburst. North is at the top and east to the left. V1647 Ori is located at the southern apex of the nebula. The color table has been scaled to represent the same brightness in all three images.

Chrétien-Coudé (RCC) and 60/90/180 cm Schmidt telescopes of the Konkoly Observatory (Hungary).

The IAC–80 telescope was equipped with a 1024×1024 Thomson CCD with a scale of $0\farcs4325$/pixel, and a field of view of $7\farcm4 \times 7\farcm4$. For the broad-band *VRI* observations we used the IAC#72, IAC#71, and IAC#70 filters[1]. Typically three frames were taken with exposure times of 120–300 s/frame each night.

At Konkoly Observatory, the 1 m RCC telescope was equipped with a Princeton Instruments VersArray 1300B camera. The back-illuminated 1340×1300 CCD has an image scale of $0\farcs306$/pixel and a field of view of $6\farcm8 \times 6\farcm6$. The Schmidt telescope was equipped with a 1536×1024 Kodak Photometrics AT 200 CCD camera. The image scale was $1\farcs03$/pixel, providing a field of view of $24' \times 17'$. On both telescopes, the utilized $V(RI)_C$ filters matched closely the standard Johnson-Cousins system (Hamilton et al., 2005). For each filter, 3–10 frames were taken on each night, and the integration times varied between 120 and 600 s/frame.

[1]The transmission curves are available at http://www.iac.es/telescopes/tcs/filtros-eng.htm

Data reduction and photometric calibration.

Raw frames were dark-subtracted and flat-fielded using the 'imred' package within the IRAF[2] environment. Dome flat-field images were taken each night, and sometimes sky flats were also available. In some cases, the consecutive frames taken through the same filter were co-added in order to increase the signal to noise. As an example, Fig. 3.1 shows R-band optical images of V1647 Ori taken with the 1m RCC telescope of the Konkoly Observatory at three different phases of the outburst.

The instrumental $V(RI)_C$ magnitudes of V1647 Ori were determined by PSF-photometry using the 'daophot' package in IRAF (Stetson, 1987). The field of view of our telescopes allowed us to include several field stars to define the point spread function of the images. The use of PSF–photometry was important to exclude the contribution of the nebula, which becomes dominant especially in the V-band. In order to assure the consistency of the results obtained with the three different telescopes we treated our data in a homogeneous manner: the position and extension of the sky region near V1647 Ori were the same in all images, and the preliminary aperture photometry, used for scaling the PSF magnitudes was obtained using equally narrow apertures (1.5 arcsec) in each image.

For photometric calibration we used the secondary standards from the list of Semkov (2006). Differential photometry was performed by computing the instrumental magnitude differences between V1647 Ori and each comparison star. The differential magnitudes were transformed into the standard photometric system as follows. For the comparison stars, we searched for a relationship between Δm, the differences between instrumental and absolute magnitudes in the V, R_C or I_C band and the color indices of the stars, similarly as described in Serra-Ricart et al. (1999). We note that the color indices of the comparison stars covered a large enough range to bracket the color indices of V1647 Ori. The data points were fitted with a linear relationship, except a few low-quality nights, when due to large scatter, all Δm values were averaged. For a given telescope, the derived color terms (the slope of the fit) were consistent from night to night within the formal uncertainties provided by the fitting procedure. Color terms computed from the 1 m RCC observations also agreed

[2]IRAF is distributed by the National Optical Astronomy Observatories, which are operated by the Association of Universities for the Research in Astronomy, Inc., under cooperative agreement with the National Science Foundation. http://iraf.noao.edu/

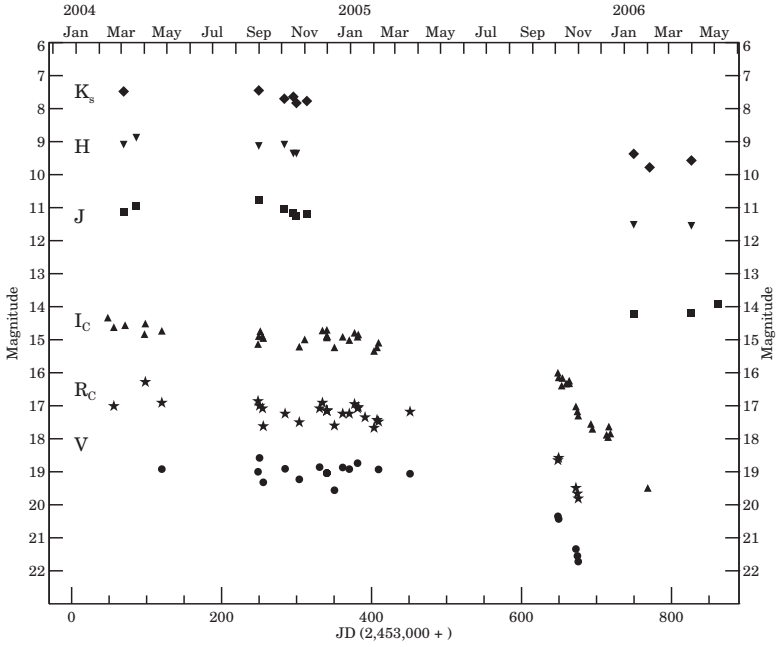

Figure 3.2 Light curves of V1647 Ori in the V *(dots)*, R_C *(asterisks)*, I_C *(upward triangles)*, J *(squares)*, H *(downward triangles)*, and K_S *(diamonds)* bands between 2004 February 16 and 2006 May 5, based on the data presented in Tables 3.1 and 3.2. The uncertainties are comparable with symbol sizes.

with values determined with high precision from observations of NGC 7790 with the same instrument. For calibration of the V1647 Ori data we applied the color terms determined for the corresponding night. Results of the optical photometry of V1647 Ori are presented in Tab. 3.1 and plotted in Fig. 3.2. The uncertainties given in Tab. 3.1 were computed as the quadratic sum of the formal errors of the instrumental magnitudes provided by IRAF and the uncertainties of the standard transformation. In those cases when the frames were evaluated separately (rather than co-added), the standard deviation of the magnitudes from each frame was also computed, and the maximum of the two types of errors was adopted.

Date	JD [a]	V	R_C	I_C	Telescope
2004 Feb 12	048.3	···	···	14.33 ± 0.04	Schmidt
2004 Feb 20	056.3	···	17.01 ± 0.08	14.62 ± 0.04	RCC
2004 Mar 06	071.3	···	···	14.56 ± 0.04	RCC
2004 Apr 1	097.2	···	···	14.83 ± 0.08	Schmidt
2004 Apr 2	098.3	···	16.28 ± 0.08	14.51 ± 0.06	Schmidt
2004 Apr 24	120.3	18.92 ± 0.06	16.91 ± 0.04	14.73 ± 0.07	IAC-80
2004 Aug 31	248.6	19.00 ± 0.12	16.86 ± 0.10	15.13 ± 0.15	RCC
2004 Sep 1	249.6	···	···	14.89 ± 0.08	IAC-80
2004 Sep 2	250.6	19.58 ± 0.08	17.00 ± 0.08	···	IAC-80
2004 Sep 3	251.6	···	···	14.74 ± 0.04	RCC
2004 Sep 6	254.6	···	17.08 ± 0.03	14.90 ± 0.04	RCC
2004 Sep 7	255.6	19.32 ± 0.06	17.62 ± 0.08	14.95 ± 0.03	RCC
2004 Oct 6	284.7	18.91 ± 0.10	17.24 ± 0.06	···	IAC-80
2004 Oct 25	303.6	19.23 ± 0.10	17.50 ± 0.05	15.21 ± 0.06	IAC-80
2004 Nov 1	310.8	···	···	14.99 ± 0.04	IAC-80
2004 Nov 21	330.7	18.86 ± 0.08	17.08 ± 0.08	···	IAC-80
2004 Nov 24	334.5	···	16.91 ± 0.07	14.72 ± 0.03	RCC
2004 Nov 30	340.4	19.04 ± 0.06	17.16 ± 0.04	14.87 ± 0.04	RCC
2004 Dec 11	350.5	19.56 ± 0.08	17.60 ± 0.05	15.23 ± 0.06	RCC
2004 Dec 22	361.5	18.87 ± 0.11	17.24 ± 0.08	14.91 ± 0.05	RCC
2004 Dec 30	370.3	18.92 ± 0.05	17.24 ± 0.06	15.01 ± 0.05	RCC
2005 Jan 6	377.3	···	16.95 ± 0.06	14.79 ± 0.07	RCC
2005 Jan 10	381.3	18.74 ± 0.06	17.08 ± 0.08	14.91 ± 0.10	RCC
2005 Jan 11	382.3	···	17.04 ± 0.07	14.84 ± 0.07	RCC
2005 Jan 20	391.3	···	17.35 ± 0.06	···	IAC-80
2005 Feb 1	403.3	···	17.67 ± 0.04	15.34 ± 0.10	RCC
2005 Feb 5	407.3	···	17.43 ± 0.09	15.23 ± 0.05	RCC
2005 Feb 7	409.3	18.93 ± 0.09	17.48 ± 0.07	15.09 ± 0.05	RCC
2005 Mar 21	451.3	19.06 ± 0.07	17.18 ± 0.03	···	IAC-80
2005 Oct 4	648.5	20.35 ± 0.10	18.65 ± 0.06	16.00 ± 0.08	RCC
2005 Oct 5	649.5	20.43 ± 0.06	18.58 ± 0.04	16.14 ± 0.05	RCC
2005 Oct 9	653.6	···	···	16.39 ± 0.06	RCC
2005 Oct 10	654.6	···	···	16.16 ± 0.04	RCC
2005 Oct 15	659.7	···	···	16.03 ± 0.07	RCC
2005 Oct 19	663.6	···	···	16.29 ± 0.05	RCC
2005 Oct 28	672.6	21.34 ± 0.16	19.49 ± 0.08	17.02 ± 0.08	RCC
2005 Oct 31	674.6	21.55 ± 0.16	19.66 ± 0.05	17.17 ± 0.03	RCC
2005 Nov 1	675.6	21.75 ± 0.08	19.83 ± 0.04	17.30 ± 0.04	RCC
2005 Nov 17	692.5	···	···	17.55 ± 0.08	RCC
2005 Nov 19	694.6	···	···	17.70 ± 0.10	RCC
2005 Dec 8	713.4	···	···	17.88 ± 0.10	RCC
2005 Dec 10	715.4	···	···	17.95 ± 0.10	RCC
2005 Dec 11	716.4	···	···	17.63 ± 0.10	RCC
2005 Dec 13	718.5	···	···	17.84 ± 0.10	RCC
2006 Feb 1	768.3	···	···	19.49 ± 0.10	RCC

Table 3.1 Optical photometry of V1647 Ori. [a] 2,453,000+

Date	JD [a]	J	H	K_S	Telescope
2004 Mar 4	069.4	11.13 ± 0.10	9.09 ± 0.07	7.48 ± 0.09	LIRIS
2004 Mar 21	086.3	11.00 ± 0.12	8.70 ± 0.19	···	TCS
2004 Sep 1	249.6	11.12 ± 0.10	9.17 ± 0.03	7.66 ± 0.01	TCS
2004 Oct 5	283.7	11.06 ± 0.07	9.07 ± 0.14	7.76 ± 0.05	TCS
2004 Oct 17	295.7	11.10 ± 0.09	9.09 ± 0.14	7.62 ± 0.04	TCS
2004 Oct 21	299.8	11.17 ± 0.08	9.19 ± 0.05	7.84 ± 0.08	TCS
2004 Nov 4	313.7	11.20 ± 0.06	···	7.77 ± 0.06	LIRIS
2006 Jan 14	749.6	14.27 ± 0.09	11.48 ± 0.08	9.41 ± 0.19	LIRIS
2006 Feb 6	770.8	···	···	9.78 ± 0.02	TCS
2006 Mar 31	826.5	14.19 ± 0.13	11.55 ± 0.05	9.57 ± 0.08	TCS
2006 May 5	861.4	13.92 ± 0.08	···	···	LIRIS
2006 Sep 9	987.8	···	11.59 ± 0.05	9.82 ± 0.06	LIRIS

Table 3.2 Near infrared photometry of V1647 Ori. [a] 2,453,000+

3.1.2 Near-infrared imaging and photometry

Near-infrared J, H, and K_S band observations were carried out at 10 epochs in the period 2004 March – 2006 September. The data were obtained using two instruments: LIRIS, installed on the 4.2 m William Herschel Telescope (WHT) at the Observatorio del Roque de Los Muchachos, and CAIN-2, installed on the 1.52 m Carlos Sanchez Telescope (CST) at the Teide Observatory. Table 3.2 lists the epochs of all near-infrared observations.

LIRIS is a near-infrared camera/spectrograph attached to the Cassegrain focus of the WHT (Acosta-Pulido et al., 2003; Manchado-Torres et al., 2003). The data were obtained during the commissioning period (2004 March) plus some nights corresponding to the guaranteed time of the instrument team. LIRIS is based on a HAWAII-1 detector with an image scale of $0\farcs25$ per pixel and $4\farcm2 \times 4\farcm2$ field of view. Observations were always performed by taking several dithered exposures around the position of V1647 Ori in order to ensure proper sky image subtraction. For each dither point we took several frames using short exposure time to avoid saturation, which were later averaged to obtain the final reduced image. The minimum exposure time was 1 s for individual exposures, the total integration time per filter was about 5 min. During the first observing period the individual exposure times were optimized to detect the nebula, which nearly saturated the detector at the position of the illuminating star.

The infrared camera CAIN–2 at the 1.52 m TCS is equipped with a 256×256 Nicmos 3

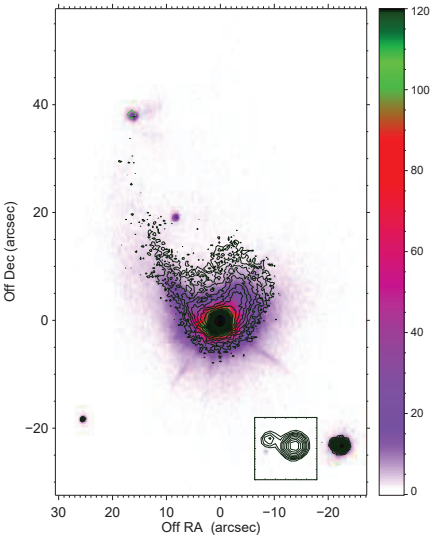

Figure 3.3 Near-infrared images of McNeil's Nebula obtained on 2004 November 4 with LIRIS on WHT. North is at the top and east to the left. The color scaled image represents the K_S-band emission and the contours represent the J-band emission. The inset is a zoom on the star southwest of V1647 Ori, demonstrating that the star is a double system. The open diamond at $(\Delta\alpha, \Delta\delta) \simeq (16'', 38'')$ marks the position of the bright infrared source detected by Muzerolle et al. (2005) in Spitzer images.

detector, which provides a pixel projection of $1''$ with its wide optics configuration. The same dithering technique was used as in the case of LIRIS observations. Total integration time was usually 10 min in all filters (J, H and K_S), splitted in many exposures of 0.5–3 s, the shortest corresponding to filter K_S and the longest to filter J.

Data reduction and photometric calibration

Data reduction process involved the following steps: sky subtraction, flat-fielding and coaddition of all frames taken with the same filter. The sky image was obtained as the median combination of all frames, masking regions occupied by bright sources. The final image was produced using the standard "shift–and–add" technique including rejection of outlier pixels. The LIRIS images were reduced using the package 'liris_ql' developed within the IRAF

environment. The CAIN–2 data were also treated with IRAF tasks. The J and K_S images obtained on 2004 November 4 can be seen in Fig. 3.3.

The instrumental magnitudes of the central star were extracted using aperture photometry since the contribution of the nebula in the near-infrared becomes negligible compared to it. Based on the measured radial profiles we estimate that the nebula contributes to the central star photometry at most 15% in the J band, but less than 5% in the K_S band. Due to the high brightness of V1647 Ori some LIRIS images entered the non–linear regime at the position of the star. In these cases we estimated the flux of the star by fitting a PSF model to the non-saturated parts of the stellar profile using the *daophot* package in IRAF.

For the photometric calibration we used the 2MASS catalog (Cutri et al., 2003). In general, five or six 2MASS stars were found within the sky region covered by our images. We have determined the offset between the instrumental and the calibrated 2MASS magnitudes by averaging all available stars, after removal of deviant sources (identified as likely variable stars by Semkov, 2006). Results of the near-infrared photometry for V1647 Ori are listed in Tab. 3.2, and the light curves are shown in Fig. 3.2. The standard deviation is used as an estimate of the measurement error and reported in Tab. 3.2. We cannot determine a reliable color term correction using our reduced number of reference stars. The 2MASS star J054611162-0006279 was always included as a comparison star, since it shows calibration offsets close to the average in all occasions. We note that this source was the only comparison star used by Walter et al. (2004) for the photometric calibration of their near-infrared data. The colors of this star are very similar to those of V1647 Ori which reduces the importance of color terms when determining the photometrical calibration.

3.1.3 Near-infrared spectroscopy

Near-infrared spectrograms of V1647 Ori were obtained using LIRIS at five different epochs, four of them during the first year of the outburst. Five spectra cover the wavelength interval of 0.9–1.4μm (ZJ bands) and three others cover the 1.4–2.4μm (HK) wavelength band. The log of the observations is presented in Tab. 3.3.

Observations were performed following an ABBA telescope nodding pattern both in the ZJ and HK bands. In order to reduce the readout noise, the measurements were done using

Date	JD [a]	Slit ($''$)	Band	t_{exp} (s)	Band	t_{exp} (s)	Air Mass
2004 Mar 8	073.4	1	ZJ	400	HK	12	1.3
2004 Nov 4	313.7	0.75	ZJ	800	HK	432	1.2
2005 Jan 24	395.4	0.75	ZJ	200	···	···	1.2
2005 Mar 25	455.4	1	ZJ	100	···	···	2.0
2006 May 5	861.4	1	ZJ	1200	HK	400	4.1
2006 Sep 9	987.7	0.75	ZJ	1200	HK	900	1.4

Table 3.3 Journal of near-infrared spectroscopy of V1647 Ori. [a] 2,453,000+

multiple correlated readout mode, with 4 readouts before and after the integration. We used a slit width of $0''.75$ or $1''$, depending on the seeing conditions, which yielded a spectral resolution in the range $R = 500$–660 and 550–700 in the ZJ and HK spectra, respectively. The wavelength calibration was provided by observations of Argon and Xenon lamps available in the calibration unit at the A&G box of the telescope. In order to obtain the telluric correction and the flux calibration, nearby A0V or G2V stars were observed with the same configuration as the object.

The data were reduced and calibrated using the package 'liris_ql'. Consecutive pairs of AB two-dimensional images were subtracted to remove the sky background, then the resulting images were wavelength calibrated and flat-fielded before registering and coadding all frames to provide the final combined spectrum. One-dimensional spectra were extracted with the IRAF 'apall' task. The extracted spectra were divided by a composite spectrum to eliminate telluric contamination. This composite spectrum was generated from the observed spectra of the calibration star, divided by a stellar model and convolved to our spectral resolution. We used the publicly available code 'Telluric' (Vacca et al., 2003) to perform the correction when A0 stars were observed. Differences in the strength of telluric features likely due to mismatch of air masses and variation of atmospheric conditions between observations of the object and the reference star were taken into account using Beer's law. The IRAF task 'telluric' was used in this step. The flux calibration was carried out normalizing to the J, H, and K_S magnitudes obtained in our near-infrared photometry. We show in Fig. 3.4 the flux calibrated infrared spectra for those observing dates when the full range from 0.9 to 2.4μm was observed.

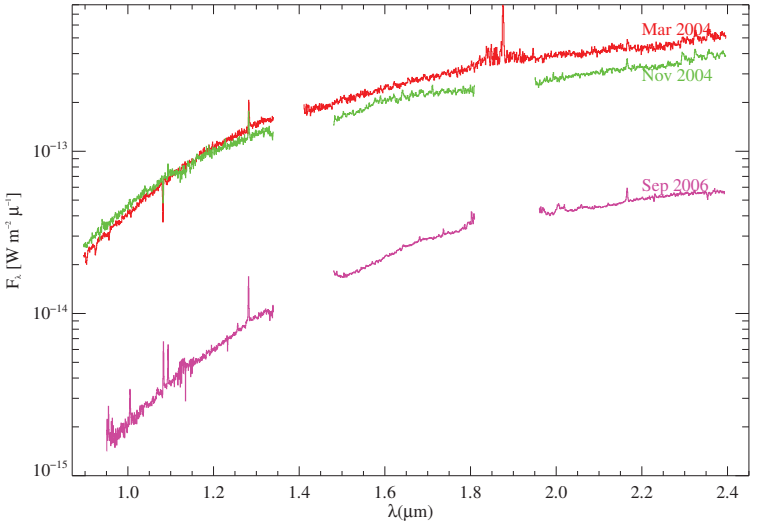

Figure 3.4 Flux calibrated near-infrared spectra of V1647 Ori obtained with LIRIS on WHT.

3.2 Brightness variations during the outburst

3.2.1 Long-term evolution

In order to examine the flux evolution during the whole outburst history we combined our I_C measurements with those of Briceño et al. (2004), which covered the beginning of the eruption. The complete I_C-band light curve is displayed in Fig. 3.5. Following an initial brightening of ~ 4.5 mag between 2003 November and 2004 February (Briceño et al., 2004), the star faded only moderately during the next one and a half years. This gradual decrease of brightness was observable in all photometric bands with similar rates (Fig. 3.2). Then, between 2005 October and November the brightness of the star suddenly dropped by more than 1 mag at all optical wavelengths (Kóspál et al., 2005). This decay was also monitored by Semkov (2006) and Ojha et al. (2006). The rapid fading continued in the next months, although the rate was slightly slower after 2005 mid-November. By 2006 February, some 800 days after the onset of the eruption, V1647 Ori was very close to the reported pre-outburst

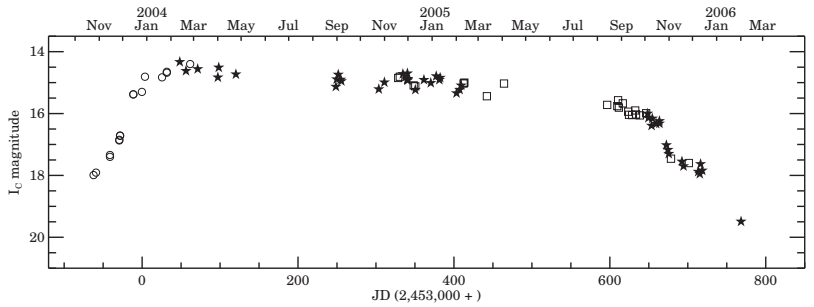

Figure 3.5 I_C-band light curve of V1647 Ori covering the complete 2-years outburst period. *Filled stars*: our observations reported in Tab. 3.1; *open circles*: data from Briceño et al. (2004); *open squares*: data from Ojha et al. (2006). The uncertainties are comparable with symbol sizes.

state.

The complete light curve of the outburst can naturally be divided into three phases: the initial rise, the "plateau", and the final decay. In order to quantify the rate of brightness evolution, we fitted straight lines to the data points in Fig. 3.5 for each phase separately. The results are −1.3 mag/month, 0.04 mag/month and 0.8 mag/month, respectively. It is remarkable that the pace of brightness change in the rising and decaying phases is similar.

The fact that the fading rate of V1647 Ori is apparently wavelength independent is different from the case of another eruptive star, V1057 Cyg, whose decline rate decreased monotonically from the ultraviolet to the mid-infrared during the years following the outburst (Kenyon & Hartmann, 1991). However, the decline of V1057 Cyg was most pronounced in the B band, which was not observable in the case of V1647 Ori.

3.2.2 Hour scale variations

Ojha et al. (2005) claimed weekly variations of the optical flux of V1647 Ori. Grosso et al. (2005) reported on a periodic variation in the X–ray flux of 0.72 days, about 17 hours. We have also searched for very short term variability in our optical data. We compared 5 consecutive I_C-band observations of V1647 Ori obtained on the same night (2004 November 30) during a period of 2.5 hours with the 1 m RCC telescope. The first four measurements are

identical within their formal photometric uncertainties (≈ 0.03 mag), but the fifth measurement deviates about 0.2 mag from the others. This figure may be the characteristic variation expected on hour scale.

3.2.3 The possible origin of variability

In order to study further the mechanisms causing the initial brightening and the final fading, we plotted in Fig. 3.6 optical and near-infrared color–magnitude diagrams, and looked for relationships between brightness and color index variations. We also marked in Fig. 3.6 the standard interstellar reddening law (Cohen et al., 1981).

Reipurth & Aspin (2004) noted that the star moved along the extinction path in the J–H vs. H–K diagram during the initial brightening phase. Ojha et al. (2006) demonstrated that the final fading of the object in November 2005 also followed the same path in the opposite direction. However, the variation of the near-infrared and visible colors is not compatible with simple dust obscuration. It can be seen from Fig. 3.6 that the amount of extinction needed to explain the color variation in the near-infrared is much larger than the one required in the visible. In order to explain the amplitude of the outburst a color independent flux increase has also to be assumed. A similar conclusion was reached by McGehee et al. (2004).

In order to explain the flux variations during the plateau phase we looked for any possible relationship between brightness and color index variations (Fig. 3.6). A loose trend that the star tends to be redder when dimmer can be observed in the diagrams. Eiroa et al. (2002) successfully explained the light variations of several young stars by obscuration by dense slabs within the circumstellar disk. A similar mechanism could be responsible for the observed variations of V1647 Ori, too.

3.2.4 Inclination of the star–nebula axis

McNeil's Nebula shines due to the scattered light of V1647 Ori, therefore its observed properties are closely related to the brightness of the star. Briceño et al. (2004) examined the temporal evolution of two well-defined positions of the nebula (marked as B and C in their fig. 2), and concluded that their light curves followed the brightening of the star with delays of about 14 days (Pos. B) and of more than 50 days (Pos. C). The angular distance of $36''$

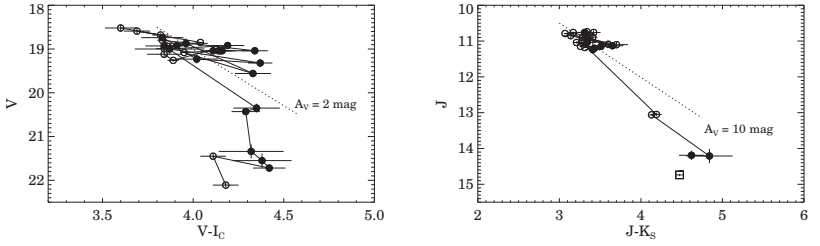

Figure 3.6 Relationship between the color indices and magnitudes of V1647 Ori during the monitoring period. *Left*: V *vs.* V−I_C; *Right*: J *vs.* J−K_S. The filled symbols represent our measurements, and the open symbols are taken from Ojha et al. (2006). The dotted lines indicate the slope of the normal interstellar reddening (Cohen et al., 1981). Solid lines connect consecutive observed points.

between the star and Pos. C implies a delay of 85 days. Since these delays carry information on the inclination of the nebula (see Fig. 3.7), we reanalysed the three I_C-band light curves (from Fig. 3 in Briceño et al., 2004), supplemented with our measurements obtained in the period 2004 February–April, in order to find the accurate time shifts between them. First we interpolated the light curves for a time sampling of 0.25 days. The resulting light curves of V1647 Ori, Pos. B, and Pos. C are called $A(t_i)$, $B(t_i)$ and $C(t_i)$, respectively, where t_i is the time ($i = 1...N$). Then we calculated a function called $D(s)$ as follows:

$$D(s) = \sum_{i=1}^{N} A(t_i) - C(t_i - s)$$

The quantity s which results in the lowest value of $D(s)$ gives the time shift between the light curves of A and C. The shifts between A and B can be calculated similarly. In this manner we obtained a time shift 12.5±2 days between V1647 Ori and B and 50±3 days between V1647 Ori and Pos. C.

The measured time delay between the light curves of V1647 Ori and Pos. C, together with the projected separation of the two objects results in an angle of 61^{+3}_{-2} degrees between the axis of the nebula and the line of sight. Because the clump lies inside the polar stellar wind cavity of the star, this angle is a good estimate for the inclination of the rotation axis of the star (see Fig. 3.7). We estimated the uncertainty of the inclination derived this way as follows. We assumed that the Herbig–Haro object *HH 23* (Eislöffel & Mundt, 1997)

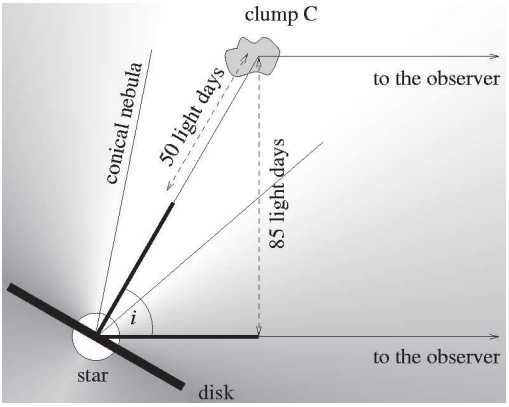

Figure 3.7 Geometry of McNeil's Nebula, deduced from the time delay between the light curves of V1647 Ori and Clump C.

lies exactly along the rotation axis of the star. Then we assumed that the projected angle between the *star–Pos. C* and *star–HH 23* directions, 11°, is the same as the difference in their tilts to the line of sight. Thus the total uncertainty of the inclination derived from the time delay of the brightness variation of clump C is $\pm 14°$.

The time delay between the light curve features of V1647 Ori and Pos. B results in $65° \pm 8°$. The inclinations derived from positions B and C are compatible within the errors. Due to the larger opening angle of the conical nebula at small distances from the star, position B is less suitable for estimating the inclination of the stellar rotation axis.

This result apparently conflicts with Rettig et al. (2005) finding that the disk of V1647 Ori is seen nearly face-on, because the absorption line of the cold CO due to the outer, flared regions of the disk cannot be observed in the high resolution infrared spectrum of the star. But if the thickness H of the disk at a distance R from the star does not exceed $H/R \approx 0.50$, then the absorption lines produced by the outer disk is not expected to be observed in the spectrum of the star.

Line	λ	2004 Mar		2004 Nov		2005 Jan		2005 Mar		2006 May		2006 Sep	
	(μm)	EW	Flux	EW	Flux	EW	Flux	EW	Flux	EW	Flux	EW	Flux
Paδ	1.005	−0.8	1.2	−2.5	1.2	−2.1	0.5	−1.7	0.4	···	···	−12.4	0.26
HeI	1.083	9.18	−5.9	4.3	−3.0	3.3	−1.1	5.2	−1.8	−11.6	0.3	−17.0	0.56
Paγ	1.094	−3.0	1.9	−2.4	1.7	−2.7	0.9	−2.2	0.8	−14.8	0.5	−13.4	0.50
Paβ	1.282	−10.7	14.4	−8.5	10.1	−12.5	8.1	−15.1	8.2	−14.9	1.4	−16.7	1.51
MgI	1.504	−3.7	7.6	−2.8	4.4	−5.9	6.6	−6.7	5.2	···	···	−1.3	0.23
Brδ	1.945	−2.9	10.5	···	···	···	···	···	···	···	···	···	···
HeI	2.058	<0.8	<3.0	0.8	−2.5	···	···	···	···	···	···	−1.7	0.77
Brγ	2.166	−5.2	22.0	−44.8	15.1	···	···	···	···	−6.9	4.0	−6.7	3.31

Table 3.4 Equivalent width and flux of near-infrared lines of V1647 Ori. EW is in Å, and flux is in units of 10^{-17} Wm^{-2}.

3.3 Spectral evolution

Our near-infrared spectra, normalized to the continuum, are displayed in Fig. 3.8 (ZJ band) and Fig. 3.9 (HK band). The most prominent features are the Paβ, Paγ, and Brγ lines of HI in emission, the HeI 1.083 μm line most of the time seen in absorption, the MgI 1.50 μm line, and the rovibrational $\Delta\nu = +2$ transitions of CO at 2.3–2.4 μm in emission. These spectral features are present in all spectra, though significant changes can be recognised in the line strengths during our observational period of 30 months. In the following we analyse these spectral variations, including also data sets from Walter et al. (2004), Gibb et al. (2006) and Ojha et al. (2006), which cover shorter periods. We note that our last spectra were taken in 2006 May and September when the outburst was over, thus probably they are representative of the quiescent phase of the object.

Table 3.4 lists the equivalent widths and fluxes of the infrared lines. The near-infrared line fluxes were computed from the absolutely calibrated spectra, with a typical estimated uncertainty of about 15% in the brightest lines to 25% in the faintest ones. Figure 3.10 shows the time evolution of the line fluxes. In addition, we plotted the Hα and CaII λ 8542 Å lines, where line fluxes were derived by combining the equivalent widths published by Walter et al. (2004) and Ojha et al. (2006), and I_C and R_C magnitudes taken from Tab. 3.1 or from the literature for the same day as the spectroscopic data. The typical uncertainty of these latter flux values, derived from the errors of the magnitudes and equivalent widths, is about 6%. We noticed inconsistencies when comparing our line fluxes with those published by other authors for close observing dates. For this reason we recomputed their line fluxes combining the reported EW with photometric data. These are the values plotted in Fig. 3.10.

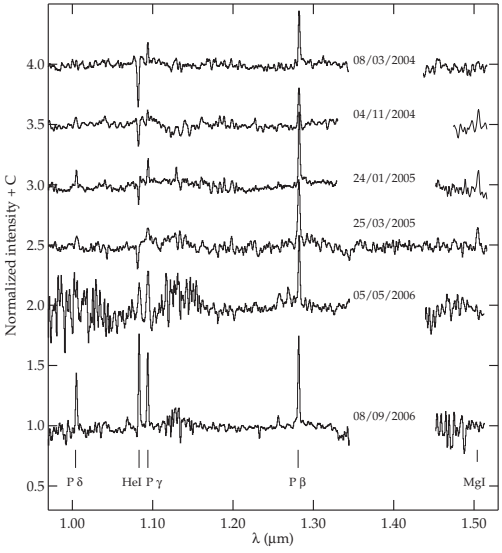

Figure 3.8 Near-infrared (ZJ-band) spectra of V1647 Ori obtained with LIRIS, normalized to the continuum.

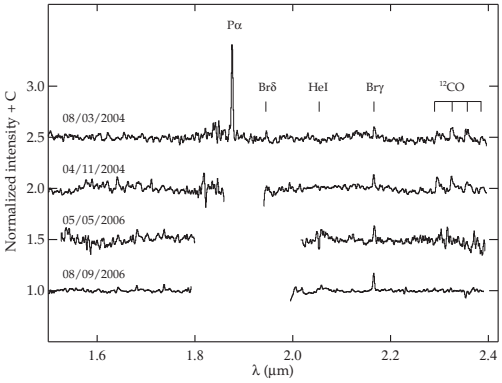

Figure 3.9 Near-infrared (HK-band) spectra of V1647 Ori obtained with LIRIS, normalized to the continuum.

Hydrogen lines. Figure 3.10 shows that the line fluxes of Paβ, Brγ and Hα declined slowly during the period of observations. The Paγ shows a similar trend, but with higher scatter.

In many young stellar objects the origin of HI lines is related to accretion processes. Muzerolle et al. (1998b) established empirical relationships between the accretion rate and the luminosity of Paβ and Brγ lines. The data in Fig. 3.10 clearly indicate parallel decrease of the strongest hydrogen emission lines during the whole outburst, which would suggest a decreasing accretion rate. Application of the relationships of Muzerolle et al. (1998b) with the assumptions that V1647 Ori is located at 400 pc from the Sun; suffers an extinction of $A_V = 11$ mag; has a mass of $0.5\,M_\odot$ and an accretion radius of $3\,R_\odot$, results in an accretion rate about $5 \times 10^{-6} M_\odot$/yr in 2004 March, and an order of magnitude lower value in 2006 May.

The Paschen lines of HI showed P Cygni profile with a blueshifted absorption only in 2004 March, whereas the absorption part disappeared in later observations. Gibb et al. (2006) also reported the same variations in the profiles of the HI lines. Similar changes of the Hα and CaII lines were reported by Ojha et al. (2006). These results indicate that at the beginning of the outburst the source of the HI lines was at least partly stellar wind, whose strength decreased during the outburst. As a consequence, the drop of accretion rate was probably smaller than we derived in the previous paragraph.

Helium lines. The evolution of the HeI 1.083 μm line tells an interesting story. It was seen in blueshifted absorption during the whole outburst, although its strength decreased with time (Fig. 3.10, see also Gibb et al., 2006). The flux decreases quickly towards the end of 2004, and later decreases again in 2006 May. In our spectra of 2006 May and September, taken in the quiescent phase this line was detected *in emission*, without any apparent velocity shift (Fig. 3.8). The transition of the HeI 1.083 μm line from absorption to emission is a remarkable event, not seen in any other line in our spectra. This line also shows a blueshifted (~ 500km s^{-1}) absorption component in the spectrum taken in 2006 September.

In young stellar objects the HeI 1.083 μm line is usually attributed to hot winds. The profile of the HeI absorption line observed in V1647 Ori was similar to those seen in a large sample of strongly accreting T Tauri stars (Edwards et al., 2006), where the whole

velocity range of the HeI wind can be observed against the stellar continuum. In these cases Edwards et al. (2006) argue that the wind traced by the HeI 1.083 μm line originates close to the star and not from the inner part of the circumstellar disk. This may also be the case for the V1647 Ori system. The hard X-ray emission from V1647 Ori, observed by the X-ray observatories *Chandra* and *XMM-Newton* (Kastner et al., 2004; Grosso et al., 2005), indicates the presence of a magnetic reconnection ring located at 1–1.5 stellar radii above the stellar surface in the plane of the disk. We speculate on that the source of the wind is the magnetic reconnection ring. This hypothesis is supported by the fact that the strongest HeI line, observed on 2004 March 8, (Fig. 3.10, Vacca et al., 2004; Gibb et al., 2006), was preceded by a high X-ray emission event on 2004 March 7, (Kastner et al., 2004), indicating a direct connection between the two phenomena. The drop of the flux of the HeI 1.083 μm line during the outburst suggests weakening of the wind.

Edwards et al. (2006) proposed that there may be two types of the hot wind, producing absorption or emission of the HeI 1.083 μm line. The transition of this line from absorption to emission at the end of the outburst indicates that the nature of the wind in V1647 Ori changed between the two types of hot wind.

We also detected the HeI 2.058 μm line in absorption both in 2004 November and 2006 May. The apparent increase of its strength in the latter spectrum (taken during quiescence) is due to the lower continuum.

Other spectral features. In Fig. 3.10 we also plotted the flux of the MgI 1.505 μm emission line. The feature was detectable during the whole outburst, showing hints for a slowly decreasing trend in flux. In the spectrum of May 2006, during the quiescent phase, the line was not visible; the derived upper limit in Tab. 3.4 indicates that the MgI 1.505 μm emission is weak in the quiescent phase.

The last panel of Fig. 3.10 shows the flux variation of the CaII 8542 Å emission line based on literature data. This middle component of the CaII triplet was found to be an excellent tracer of the accretion rate (Muzerolle et al., 1998a). It can be seen that, contrary to all the other lines in Fig. 3.10, the flux of the CaII 8542 Å line was constant during the period of the observations (there is no available measurement from the quiescent phase). A reason for the discrepancy may be that the hydrogen and calcium lines originate from regions where the

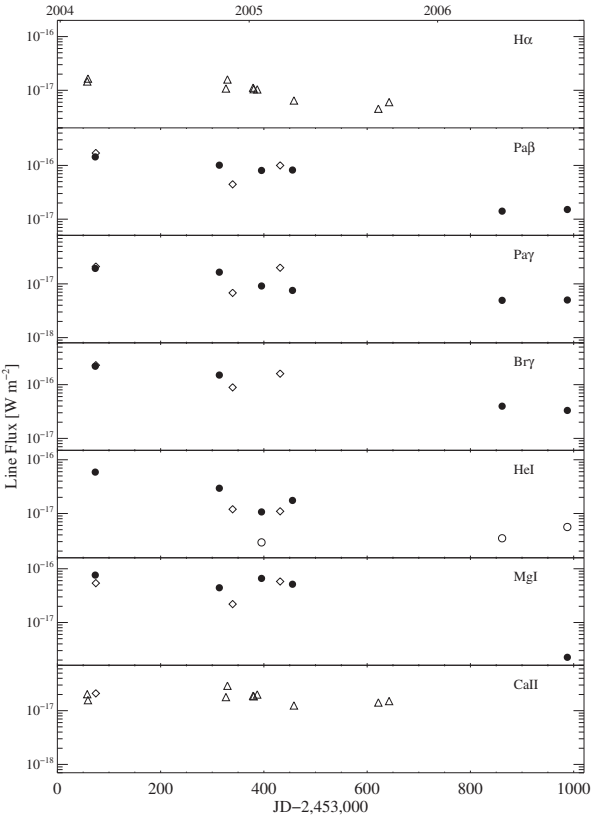

Figure 3.10 Flux evolution of near-infrared and optical spectral lines of V1647 Ori. *Circles:* this study, open circles correspond to HeI emission component (Tab. 3.4); *diamonds:* data taken from Gibb et al. (2006); *triangles:* data taken from Walter et al. (2004) and Ojha et al. (2006). The formal error bars are smaller than the symbol sizes.

physical conditions are very different. Ojha et al. (2006) noted that the density of the CaII region is very high and optically very thick. According to Muzerolle et al. (2001) optically thick lines are less reliable tracers of the variable accretion. The accretion rate, derived from its luminosity, is about $2 \times 10^{-6} M_{\odot}/\mathrm{yr}$, close to the values obtained from the hydrogen lines for the high state of the outburst.

The CO band head features at 2.3–2.4 μm were observed in strong emission during the whole outburst period (Fig. 3.9, see also Reipurth & Aspin, 2004; Vacca et al., 2004; Rettig et al., 2005; Gibb et al., 2006). However, the CO feature is not present in our quiescent spectrum suggesting that the appearance of this band is related to the outburst.

3.4 The nebula around V1647 Ori

McNeil's nebula is a reflection nebulosity which scatters the light of its illuminating star, V1647 Ori. The optical and near-infrared morphology of the nebula can be seen in Fig. 3.1 and Fig. 3.3, respectively. Their study provides information not only on the neighbouring interstellar medium but also on the outbursting star. In the following we describe the morphology of the nebula (see also Ojha et al., 2005; Reipurth & Aspin, 2004).

Comparing the optical and near-infrared images one immediately notices that the shape of the nebula looks rather different at optical (Fig. 3.1) and at infrared wavelengths (Fig. 3.3). In the optical images the nebula shows a conical shape, extending up to a distance of $\sim 50''$ ($\sim$ 22000 AU at the distance of the nebula) to the north. The diffuse emission area appears to be delimited by two bright regions indicating an opening angle of $\sim 50°$. The north-west side is marked by region B (named by Briceño et al., 2004), a plume located at a distance between 5 and 10″. The north-east rim appears more extended and is delimited by region C (also named by Briceño et al., 2004), which is located around 35″ from the star and is elongated perpendicularly to the radial axis from the star. No southern extension of the nebula can be recognized in the optical images.

In contrast to the optical, the infrared morphology indicates a much more compact structure, though the cometary shape can still be seen with a sharp curved tail along the north–east side. The nebula appears to be more extended in the J band, exhibiting diffuse emission both at the north–east and west sides. It appears roughly spherical in the K_S band, although the structure is flattened perpendicularly to the nebula axis; the largest size of the structure is $\sim 18''$. This size corresponds to a diameter of $\sim$ 7200 AU at the distance of Orion B cloud, which is slightly smaller than the size derived by Johnstone et al. (2001) for the matching submillimeter source *Ori B N55*, about 13500 AU. The southward extension is also clearly seen in the K_S band.

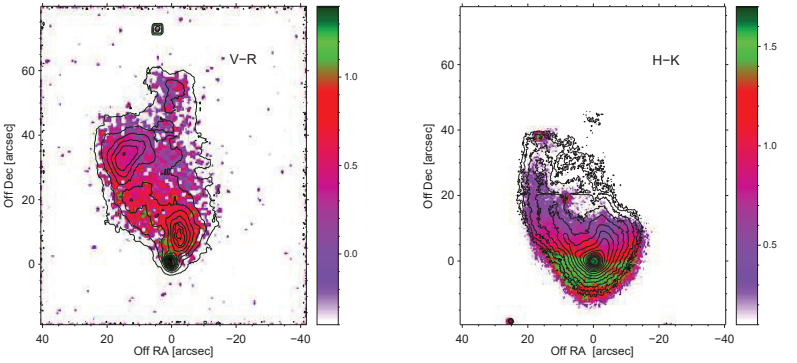

Figure 3.11 Color maps showing the V−R_C (*left panel*) and H−K_S (*right panel*) indices of the infrared nebula around V1647 Ori. The contours in the left and right panels represent the emission in R_C and J bands, respectively.

3.5 Discussion

The eruptions of young stellar objects are commonly explained as a consequence of dramatically enhanced accretion from the circumstellar disk onto the star. Based on this idea, detailed models for FUors have been developed by Bell & Lin (1994) (hereafter BL model), which were later extended to include trigger mechanism for the eruption (Bell et al., 1995), and to take into account reprocessed light (Turner et al., 1997). In this section we first discuss whether the different types of observational results on V1647 Ori, collected during the two years of the outburst, could be consistently interpreted in the framework of the BL model. Then we comment on the question if V1647 Ori could be considered to be a member of either the FUor or the EXor group.

3.5.1 The outburst mechanism

Pre-outburst phase. In the BL model FUor eruptions occur in low-mass pre-main sequence stars at an early evolutionary phase ($t_{age} \leq 10^5$ yr). These young objects are still surrounded by an infalling envelope which feeds material onto an accretion disk. V1647 Ori seems to be precisely this type of star: based on pre-outburst measurements, it is a Class

I/Class II object ($t_{age} \approx 10^4$ yr), whose flat SED shows that the object is deeply embedded (Ábrahám et al., 2004b).

The rate at which material spirals within the disk towards the star is a critical input parameter of the BL model. If accretion exceeds a threshold value of about $5 \times 10^{-7} M_\odot$/yr, then most of the matter would not fall directly onto the star due to the inefficient outward transportation of angular momentum. It piles up in the inner disk, soon or later leading to an outburst. In Sect. 3.3 we determined the accretion rate of V1647 Ori from the Brγ line fluxes for May 2006 when the star was in quiescent phase, and obtained a value of $5 \times 10^{-7} M_\odot$/yr (a similar figure was proposed by Muzerolle et al. 2005). The result agrees with the threshold value, indicating that V1647 Ori just passed the criterion of the BL model to produce an outburst, but its accretion rate in the disk was probably the lowest among all known FUors.

The outburst. According to the BL model, the inflowing matter piles up in the inner disk at $R_{limit} \approx 0.25$ AU, until its column density – and thus opacity – becomes high enough to switch on a thermal instability. An ionisation front propagates in the inner disk, and the emission of the bright ionised region behind the front causes the increase of flux at optical and near-infrared wavelengths. V1647 Ori brightened by about 4.5 magnitudes in the I_C band, which is a typical value for FUor eruptions. One should note, however, that the brightening of V1647 Ori consisted of two effects of comparable amplitude: an intrinsic brightening presumably related to the appearance of a new hot component in the system (probably the ionised inner disk); and a dust-clearing event which reduced the extinction along the line-of-sight (Reipurth & Aspin, 2004; McGehee et al., 2004). Thus the amplitude of the outburst of V1647 Ori was probably lower than typical of FUors. Also, the bolometric luminosity increased only by a factor of 15, in contrast with the factor of $\sim$100 of classical FUors.

During the outburst the high temperature in the ionized part of inner disk leads to higher efficiency of angular momentum transport, resulting in dramatically increased accretion rate onto the star. Muzerolle et al. (2005) determined that the accretion rate increased by a factor of 15. In Sec. 3.3 we calculated an accretion rate of $5 \times 10^{-6} M_\odot$/yr from the Brγ line luminosity for the peak of the outburst (close to the estimates of Vacca et al. 2004 and Gibb

et al. 2006). These results suggest that in the eruption of V1647 Ori both the peak value of the accretion rate and its increase with respect to the quiescent phase were relatively modest compared to those of other FUors.

Many observations indicated that a new, hot component appeared in the V1647 Ori system during the outburst. This component is probably the inner ionised part of the disk, for which the BL model predicts a surface temperature of 6000-8000 K. The observations seem to be consistent with this expectation: McGehee et al. (2004) attempted to fit the SED of this new component with a 7000 K blackbody; Muzerolle et al. (2005) assumed a temperature of 6000 K for the innermost, outbursting part of the disk; and the disk model of Ábrahám et al. (2006) predicted a temperature of 4200 K for the same part. The high temperature of the inner disk is also supported by the CO excitation diagrams (2400 K, Rettig et al., 2005). It is also consistent with the model of Bell & Lin (1994), that the region participating in the outburst is limited to within a few AU around the star (see the interferometric measurements by Ábrahám et al. 2006; and the estimations of Tsukagoshi et al. 2005).

The main apparent contradiction to the BL model is related to the timescales. In their standard self-regulated model, Bell & Lin (1994) computed a rise time of several decades (matching the case of the FUor V1515 Cyg). In order to explain shorter initial brightening curves (e.g. V1057 Cyg, FU Ori), they proposed 'triggered eruption' when a nearby companion can temporarily increase the accretion rate. V1647 Ori went into outburst in about 4 months (Briceño et al., 2004), thus it is tempting to speculate on such a trigger mechanism; but so far there is no observational signature of any companion. One can realize, however, that in the BL model all timescales depend on the accretion rate in the outer disk: lowering the accretion rate leads to shorter eruptions. Thus the very low accretion rate of V1647 Ori (practically at the threshold value for producing an outburst) can be one factor to explain the short initial brightening. Table 2 in the paper of Bell & Lin (1994) presents rise time estimates for several $\dot{M}_{in}$ values. Interpolating within this table suggests, however, that the resulting timescales are still too long for V1647 Ori. The other main factor which determines the timescale of the initial brightening is the viscosity parameter in the outburst high state of the inner disk α_h. Guessing again from the numbers of Table 2 of Bell & Lin (1994), we

concluded that a value of $\alpha_h = 3 \times 10^{-2}$ (rather than their standard value of $\alpha_h = 10^{-3}$) would produce the observed rising timescale of about 4 months.

The plateau phase. The initial brightening of V1647 Ori was followed by a 2-year long slow fading. This is the period under which the inner disk depletes and the matter is becoming neutral again. The length of this period is determined by the same viscosity parameter as we discussed in relation to the length of the initial brightening. It is encouraging, that adopting again $\alpha_h = 3 \times 10^{-2}$ and taking into account the low accretion rate of V1647 Ori, from the numbers in Tab. 2 of Bell & Lin (1994) we estimated a plateau phase of about two years, consistently with the observations.

According to the model of Bell & Lin (1994), the fading is due to the decreasing accretion rate. Checking two independent indicators of the accretion rate, in Sec. 3.3 we found the somewhat contradictory result that the temporal evolution of the flux of the HI lines indeed shows such a monotonic drop in the accretion rate, while the CaII 8542 Å line fluxes remained constant during the whole outburst.

The fading rate during this plateau was about 0.04 mag/yr. As mentioned already in Sect. 3.1, the fact that the fading rate appears wavelength independent suggests that no significant temperature variation occurred in the inner parts of the star-disk system in this period.

Final fading. In October 2005, V1647 Ori started a sudden fading which took approximately 4 months and ended when the object returned to the quiescent, pre-outburst state at optical and near-infrared wavelengths. Remarkably, the rate of the brightness change was similar during the final fading and the initial brightening. This is a natural fact in the BL model, where the ionization front reverses at the end of the outburst and proceeds with the same speed as in the extension phase. We note that such a return of a FUor to the quiescent phase has never been observed before.

Recurrent outbursts? Following an eruption, steady accretion from the outer disk slowly fills up the inner disk at R_{limit}, and the system is prepared for a new outburst. The timescale between outbursts is determined by the viscosity parameter of the model in the quiescent

cold state of the system α_c. From a rough interpolation in Tab. 2 of Bell & Lin (1994) one may conclude that $\alpha_c \approx 1.5 \times 10^{-3}$ would produce the 40 yr period between the last and the present outburst of V1647 Ori. This number is larger than the corresponding value in the standard BL model by a factor of 15.

Dust sublimation/condensation. Similarly to the initial brightening, the final fading also consisted of two events: an intrinsic fading and an increasing extinction along the line-of-sight. This suggests that the effects changing the extinction must be reversible. This reversibility is also supported by the fact that V1647 Ori had already an outburst in 1966–1967 (Aspin et al., 2006). Thus among the possible mechanisms responsible for the dust-clearing event sublimation of dust particles at the beginning of the outburst is a likely explanation. It could be a reversible process, since the increasing extinction observed during the final fading can be due to the condensation of dust grains (dust condensation effects were already observed in young eruptive stars, e.g. V1515 Cyg in 1980, see Kenyon et al. (1991)).

Wind. The analysis of spectral lines (Sect. 3.3) suggests the presence of a wind which was strongest at the peak of the outburst. During the plateau phase the P Cygni profile of the prominent spectral lines disappeared, also indicating that the strong wind present at the peak of the outburst decreased considerably. Such a wind is not included in the model of Bell & Lin (1994), but should be taken into account for a detailed modelling of V1647 Ori. The detailed model should also take into account the interesting finding that the HeI absorption turned into emission in the quiescent phase, indicating that the type of the wind changed after the end of the outburst.

Conclusions. From the comparison of observations of V1647 Ori with the model of Bell & Lin (1994) we conclude that the BL model reproduces most observational results, but in order to match the timescales one order of magnitude higher viscosity parameters – both in the cold and the high states – have to be assumed. The physical reason behind the increased viscosity parameter cannot be deduced from the available data.

3.5.2 FUor or EXor?

In the literature there is an on-going debate on the classification of V1647 Ori, presenting a number of arguments supporting either the FUor- or the EXor-like nature. On the one hand, in our previous paper (Ábrahám et al., 2004b) we argued that the shape of the SED is similar to FUors, and now we can add that the model of Bell et al. (1997), developed for explaining the FUor phenomenon, can model the outburst of V1647 Ori reasonably well. On the other hand, the short timescale of the eruption (2 years) and the recurrent nature argue more for an EXor-type event. EXors, however, are assumed to be classical T Tauri stars, while V1647 Ori is obviously in an earlier evolutionary phase than T Tau stars. We speculate that V1647 Ori – together with another recently erupted young stellar object OO Serpentis (Kóspál et al., 2007, see also Chapter 2) – might form a new class of young eruptive stars. Members of this class may be defined by their relatively short timescales, recurrent outbursts, modest increase in bolometric luminosity and accretion rate, and an evolutionary state earlier than that of typical EXors.

3.6 Summary

Comparison of our optical and near-infrared data obtained in 2004 February–2006 September on V1647 Ori with published results led to the following new results:

(1) The brightness of V1647 Ori stayed more than 4 mag above the pre-outburst level until October 2005 when it started a rapid fading.

(2) The time delay between the brightness variations of the star and a nebular position corresponds to an angle of $61^\circ \pm 14^\circ$ between the axis of the nebula and the line of sight.

(3) Based on our optical and near-infrared spectra obtained at different epochs during the outburst, we analysed the temporal variation of a number of spectral features. The observed decrease of line flux of the hydrogen lines can be interpreted as a decrease in the accretion rate of about an order of magnitude between the peak brightness and

the quiescence. An interesting result is that the CO band head emission at 2.2 μm was observable during the outburst, but is not present in our quiescent spectrum.

(4) The J−H and H−K_S color maps of the infrared nebula reveal an envelope around the star whose largest extension is about 18″(0.03 pc).

(5) We show that the observed properties of V1647 Ori could be interpreted in the framework of the thermal instability models of Bell et al. (1995).

(6) V1647 Ori might belong to a new class of young eruptive stars, defined by relatively short timescales, recurrent outbursts, modest increase in bolometric luminosity and accretion rate, and an evolutionary state earlier than that of typical EXors.

Chapter 4

High-resolution polarimetry of Parsamian 21

4.1 Introduction

Parsamian 21 is a system consisting of a central object, HBC 687 ($\alpha_{2000} = 19^{\rm h}\ 29^{\rm m}\ 0.87^{\rm s}$, $\delta_{2000} = 9^\circ\ 38'\ 42.69''$), and an extended nebula first listed in the catalogue of Parsamian (1965). Though no optical outburst was ever observed, Parsamian 21 was classified as a FUor on the basis of its optical spectroscopic and far-infrared properties (Staude & Neckel, 1992). According to Henning et al. (1998) Parsamian 21 is situated in a molecular cloud named "Cloud A", very close to the Galactic plane. Indeed, the distance of 400 pc and the radial velocity of $v_{lsr} = +27 \pm 15\,\mathrm{km\ s^{-1}}$ (Staude & Neckel, 1992) agree very well with the respective values for Cloud A ($v_{lsr} = +27 \pm 4\,\mathrm{km\ s^{-1}}$, $d = 500 \pm 100\,\mathrm{pc}$, Dame & Thaddeus, 1985). Recently Quanz et al. (2007) questioned the FUor nature of Parsamian 21 referring to mid-infrared spectral properties, which better resemble those of post-ABG stars (this issue will be discussed in Sect. 4.4).

The elongated nebulosity around the central source extends $\approx 1'$ to the north, while it is less developed to the south (Fig. 4.1). It is visible in the optical and the near-infrared, though the source becomes unresolved at 10.8 and 18.2 μm (Polomski et al., 2005). Polarimetric observations by Draper et al. (1985, see also Fig. 4.1) revealed a centrosymmetric polarization pattern and an elongated band of low polarization perpendicular to the axis of the bright

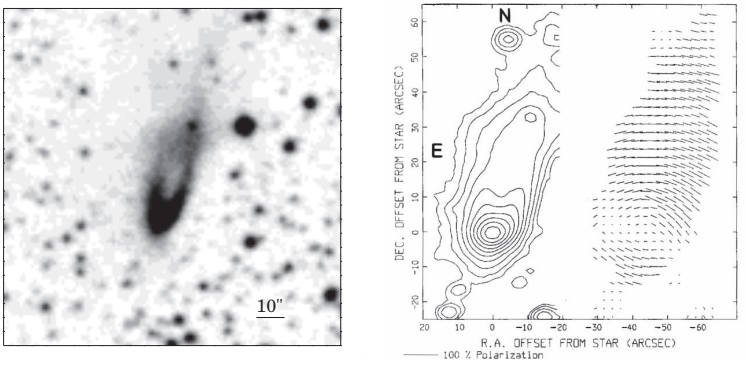

Figure 4.1 *Left:* Palomar red plate showing Parsamian 21 (from the Second Palomar Observatory Sky Survey); *Right:* a contour and polarization map of Parsamian 21 at 450–1000 nm (from Draper et al., 1985).

nebula. Bastien & Ménard (1990) interpreted the polarization map of Parsamian 21 in terms of multiple scattering in flattened, optically thick structures and derived an inclination angle of 80-85° and a size of $30'' \times 8''$ for this disk-like structure. The existence of a disk is also supported by the discovery of a short bipolar outflow oriented along the the polar axis of the nebula (Staude & Neckel, 1992). Emission at submm wavelengths was detected by Polomski et al. (2005) and Henning et al. (1998). The surroundings of Parsamian 21 have been searched for companions several times, but close-by stars seen in J, H and K-band images proved to be field stars (Li et al., 1994), and no close-by sources have been found at longer wavelengths so far (Polomski et al., 2005).

Several studies were recently published on the circumstellar environment of FUors using high resolution infrared and interferometric techniques (e.g. Green et al. 2006; Malbet et al. 1998, 2005; Millan-Gabet et al. 2006; Quanz et al. 2007). Such observations could prove or disprove the basic assumptions of FUor models. In this chapter we present the highest resolution imaging and polarimetric data yet on Parsamian 21 from the VLT/NACO instrument, allowing the inspection of the circumstellar material and disk at spatial scales of $\approx 0.07''$. The edge-on geometry of Parsamian 21 provides an ideal configuration to separate the components of the circumstellar environment (disk, envelope) and understand their role

in the FUor phenomenon.

In the following, I present and analyse new high spatial resolution near-infrared direct and polarimetric observations of Parsamian 21, as well as archival infrared photometric and spectroscopic measurements.

4.2 Observations and data reduction

The log of observations presented in this chapter is summarized in Table 4.1. In the following subsections I present these measurements in detail.

4.2.1 VLT/NACO observations

We have acquired ground-based near-infrared imaging and polarimetric observations in visitor mode using the NACO instrument mounted on the UT4 of ESO's Very Large Telescope at Cerro Paranal, Chile on 2004 June 18 (the observations were conducted by Dániel Apai). NACO consists of the NAOS adaptive optics system and the CONICA near-infrared camera (Lenzen et al., 1998; Hartung et al., 2000; Rousset et al., 2003). The weather conditions were excellent, the typical optical seeing was $\approx 0.72''$ with two short peaks of $1.3''$ during the night. For imaging, we used the visual dichroic and a camera with 13 mas/pixel scale to obtain H ($\lambda_c = 1.66\,\mu$m) and K_S ($\lambda_c = 2.18\,\mu$m) images and a camera with 27 mas/pixel scale to obtain L′ ($\lambda_c = 3.8\,\mu$m) images. In each filter, a 4-point dithering was applied with small-amplitude random jitter at each location. The adaptive optics configuration was fine-tuned for each filter to ensure the best possible correction. The H-band polarimetric observations were obtained using a 27 mas/pixel scale camera.

VLT/NACO imaging. The data reduction was carried out using self-developed IDL routines. For the H and K_S band filters lampflats were taken, while for the L′ filter, skyflats were acquired. For each filter, these images were combined to a final flatfield, and bad pixel maps were produced. Then the raw images were flatfield corrected, and bad pixels were removed. Sky frames were calculated by taking the median of all images taken with the same filter, then images were sky subtracted. Individual frames were shifted to the same position

Instrument	Filter (central λ)	Mode	Date YY/MM/DD	Exp. Time	Field of View [″ × ″]	Pixel scale [″]	FWHM [″]
VLT/NACO	H (1.66 μm)	Imaging	04/06/18	8×30 s	13.6×13.6	0.013	0.07
VLT/NACO	K_S (2.18 μm)	Imaging	04/06/18	8×20 s	13.6×13.6	0.013	0.07
VLT/NACO	L′ (3.80 μm)	Imaging	04/06/18	48×0.2 s	27.8×27.8	0.027	0.11
VLT/NACO	H (1.66 μm)	Polarimetry	04/06/18	72×10 s, 24×80 s	27.8×3.1	0.027	0.12
GFP	6563 and 6590Å	Imaging	07/05/15	900 s	130 circular	0.38	1.1
HST/NICMOS	2 μm	Polarimetry	97/11/12	18×31 s	19.5×19.3	0.076	0.16
HST/WFPC2	F814W (0.80 μm)	Imaging	01/07/30	2×500 s	79.5×79.5	0.1	0.17
Spitzer/IRAC	3.6, 4.5, 5.8 and 8.0 μm	Imaging	04/04/21	848 s	318×318	1.2	1.9–2.7
Spitzer/MIPS	24 and 70 μm	Imaging	04/04/13	73 s, 462 s	444×480, 174×192	2.5, 4.0	6, 18
Spitzer/IRS	5−40 μm	Spectroscopy	04/04/18	1121 s			
ISO/ISOPHOT	65 and 100 μm	Imaging	96/09/28	3542 s	360×420	15	44, 47

Table 4.1 Log of the observations of Parsamian 21. *Top part:* data from this work; *bottom part:* archival data.

and their median was taken to obtain the final mosaic. Shifts were calculated by computing the cross-correlation of the images, which gives a more precise result in the case of extended sources, than a simple Gaussian-fitting to the peak. Dithering resulted in a final mosaic of $21.4'' \times 21.4''$ in case of the H and K_S band, and $43.8'' \times 43.8''$ in L′ band. The photometric standard was S889-E for the H and K_S filters (H=11.662±0.004 mag, K_S=11.585±0.005 mag, Persson et al. 1998), and HD 205772 for the L′ filter (L′=7.636±0.027 mag, Bouchet et al. 1991).

VLT/NACO polarimetry. Polarimetric observations were obtained using the differential polarimetric imaging technique (DPI, Kuhn et al., 2001; Apai et al., 2004). The basic idea of this method is to take the difference of two orthogonally polarized, simultaneously acquired images of the same object in order to remove all non-polarized light. As the non-polarized light mainly comes from the central star, after subtraction only the polarized light, such as the scattered light from the circumstellar material remains.

We obtained polarimetric images with NACO through the H filter, using a Wollaston prism, which splits the light into two orthogonally polarized outgoing beams (the ordinary and the extraordinary beam). To exclude the overlapping of the beams of orthogonal polarization, a 2.8″ Wollaston mask was introduced in the light path (Fig. 4.2). Parsamian 21 was observed at four different rotator angles of 0°, 45°, 90°, and 135°, providing a redundant sampling of the polarization vectors (Fig. 4.3). At each angle a 3-point dithering was applied to allow sky subtraction and the removal of bad pixels. In order to increase the dynamic

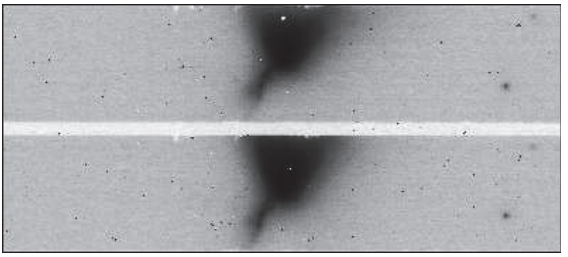

Figure 4.2 Part of a raw NACO polarimetric observation showing the two orthogonally polarized images of Parsamian 21 (top: ordinary beam (o), bottom: extraordinary beam (e)).

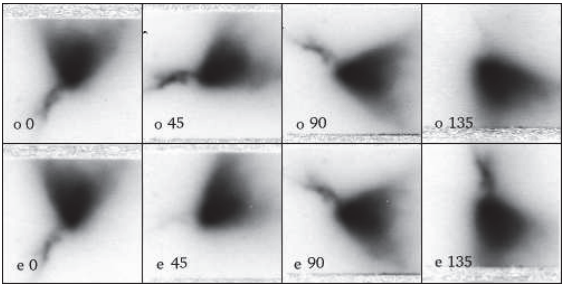

Figure 4.3 NACO polarimetric images of Parsamian 21 obtained at four different rotator angles (top row: ordinary beam, bottom row: extraordinary beam).

range of the observations, eight independent data sets were obtained: six short exposure time sets (exposure time per frame: 10 s, total on-source exposure time: 720 s) and two long exposure time sets (exposure time per frame: 80 s, total on-source exposure time: 1920 s). The polarimetric calibrator was R CrA DC No. 71 (Whittet et al., 1992), which were observed with identical instrumental setup (exposure time per frame: 0.5 s, total on-source exposure time: 3 s).

The polarimetric data reduction was done in IDL partly using previously developed software tools which we presented in detail in Apai et al. (2004, HYDRA pipeline), partly using self-developed routines. The raw images were sky subtracted and flat field corrected. Ordinary and extraordinary beams were located by finding the two peaks in each individual exposure and 124×124 pixel sub-images were cut (Fig. 4.3). The median of the three dither positions were calculated. On each frame with a rotator angle of α, the ordinary ray records

I_α, while the extraordinary ray records $I_{\alpha+90}$. Therefore, the resulting dataset is redundant, since

$$o\,0 = e\,90 = I_0 \tag{4.1}$$
$$o\,45 = e\,135 = I_{45} \tag{4.2}$$
$$o\,90 = e\,0 = I_{90} \tag{4.3}$$
$$o\,135 = e\,45 = I_{135} \tag{4.4}$$

Thus, the four intensities can be calculated as follows:

$$I_0 = \frac{o\,0 + e\,90}{2} \tag{4.5}$$
$$I_{45} = \frac{o\,45 + e\,135}{2} \tag{4.6}$$
$$I_{90} = \frac{o\,90 + e\,0}{2} \tag{4.7}$$
$$I_{135} = \frac{o\,135 + e\,45}{2} \tag{4.8}$$

From this, the I total intensity, the Q and U Stokes parameters, and the PI polarized intensity is (see e.g. Tinbergen, 1996):

$$I = I_0 + I_{90} = I_{45} + I_{135} = \frac{I_0 + I_{45} + I_{90} + I_{135}}{2} \tag{4.9}$$
$$Q = \frac{I_0 - I_{90}}{I} \tag{4.10}$$
$$U = \frac{I_{45} - I_{135}}{I} \tag{4.11}$$
$$PI = \sqrt{Q^2 + U^2} \tag{4.12}$$

These calculations were repeated independently on each dataset (six short and two long exposure time sets), and images with the same exposure time were averaged. The resulting total intensity, polarized intensity and degree of polarization maps can be seen in Fig. 4.12.

4.2.2 GFP H_α imagery

Parsamian 21 was observed with the Goddard Fabry-Perot (GFP) interferometer at the Apache Point Observatory 3.5m telescope on 2007 May 15. The observations were made

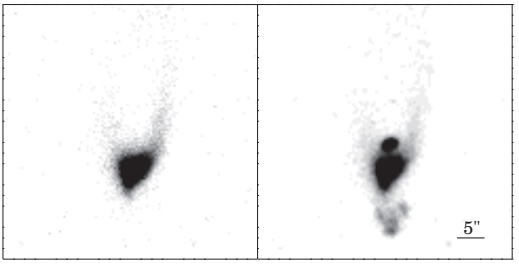

Figure 4.4 Parts of the GFP images showing Parsamian 21 and its surroundings. *Left:* off-band image ($\lambda_c = 6590\,\text{Å}$); *right:* on-band images ($\lambda_c = 6563\,\text{Å}$). North is to the top and east is to the left.

in direct imaging mode. The on-band image has a central wavelength of 6563 Å (H_α) and a width of 120 km/s. The off-band image has a central wavelength of 6590 Å and a width of 120 km/s. The pixel scale is $0.38''$ per pixel. The observations were made through patchy cirrus and are not photometric, with seeing near $1''$. The instrument and data reduction are described in Wassell et al. (2006) and references therein. For the H_α on-band image, conspicuous night sky rings contaminate the region near Parsamian 21. In order to remove these rings, we created a data cube consisting of subimages centered on the GFP optical axis, rotated by different angles. After excluding the area around Parsamian 21, we azimuthally medianed the subimages, and subtracted the resulting image from the original measurement. For the off-band image, the night sky rings had displaced beyond the location of the Parsamian 21 nebulosity, thus no ring subtraction was necessary. The on- and off-band images were shifted and scaled to match each other by measuring the positions and fluxes of seven stars in the vicinity of Parsamian 21. The on- and off-band images showing Parsamian 21 and its surroundings can be seen in Fig. 4.4, while the continuum-subtracted H_α image is plotted in Fig. 4.8.

4.2.3 HST archival data

HST/NICMOS polarimetric observations were obtained on 1997 November 12 using the NIC2 camera in MULTIACCUM mode, and the POL0L, POL120L and POL240L polarizing filters. These filters have a bandpass between 1.9 and 2.1 μm. Raw data files were calibrated

at the STScI with the *calnica* v.4.1.1 pipeline. Since these data have not been published yet, I downloaded the pipeline-processed files and did further processing using the IDL-based *Polarizer Data Analysis Software*, which is available through the STScI website and is described by Mazzuca & Hines (1999). This software package combines the images obtained through the three polarizers using an algorithm described in Hines et al. (2000). I used coefficients appropriate for the pre-NCS measurements from Hines & Schneider (2006). A 6-point dither pattern was applied, covering in all about $24'' \times 34''$. The central star and the inner parts of the Parsamian 21 nebula can only be seen in two of the six images, which I shifted and co-added.

HST/WFPC2. Parsamian 21 was observed with the WFPC2 on 2001 July 30 through the F814W filter. Parsamian 21 is in the middle of the image on the WF3 chip (Fig. 4.6), which has a pixel scale of $0.1''$. Since these data have not been published yet, I used the High-Level Science Product with the association name 'U6FC2801B', available at the HST archive.

4.2.4 Spitzer archival data

Observations of Parsamian 21 were obtained on 2004 April 13 (MIPS), April 18 (IRS) and April 21 (IRAC). The MIPS and IRAC, as well as part of the IRS data are still unpublished. The IRAC images cover an area of $5.3' \times 5.3'$ centered on Parsamian 21. The 'high-dynamic-range' mode was used to obtain 15 frames in each position, 5 with 0.4 s exposure time and 10 with 10.4 s. The frames were processed with the SSC IRAC Pipeline v14.0 to Basic Calibrated Data (BCD) level. I processed the BCD frames using the IRAC artifact mitigation software, and finally I made a mosaic of the artifact-corrected frames with MOPEX. As an example, part of the 3.6 μm image can be seen in Fig. 4.5. Photometry for Parsamian 21 was done in IDL. I used the short exposure images, because Parsamian 21 did not saturate these frames. I used an aperture of $6''$ and a sky annulus between 6 and $12''$. The aperture corrections were 1.061, 1.064, 1.067, and 1.089 for the four channels, respectively[1]. Color correction was applied by convolving the observed SED with the IRAC filter profiles in an iterative way.

[1]IRAC Data Handbook, version 3.0,
available at http://ssc.spitzer.caltech.edu/irac/dh/iracdatahandbook3.0.pdf

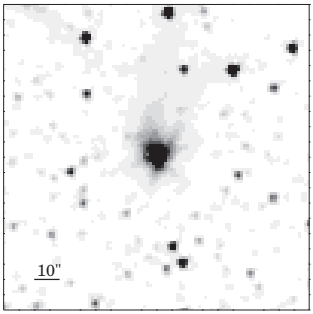

Figure 4.5 Part of the Spitzer/IRAC 3.6 μm image of Parsamian 21. North is to the top and east is to the left.

The resulting color-corrected fluxes can be seen in Table 4.2.

Photometry for field stars was obtained in the long exposure images, because most field stars are fainter than Parsamian 21 and did not saturate even the long exposure frames. For this purpose we used *StarFinder*, which is an IDL-GUI based program for crowded stellar fields analysis (Diolaiti et al., 2000). PSF-photometry was calculated for all stars having S/N > 3 and aperture corrections corresponding to "infinite" aperture radius were applied (0.944, 0.937, 0.772, and 0.737 for the four channels, respectively[1]). Then, we cross-identified the sources in the four bands and found that 100 field stars are present in all four IRAC images. We plotted these sources as well as Parsamian 21 on a [3.6]−[4.5] vs. [5.8]−[8.0] color-color diagram in Fig. 4.15. This plot will be discussed in Sect. 4.4.2.

The MIPS 24 and 70 μm images were taken in 'compact source super resolution' mode. At 24 μm 14 frames (each with 2.62 s exposure time), at 70 μm 44 frames (each with 10.49 s exposure time) were combined into a final mosaic using MOPEX. At 24 μm Parsamian 21 saturated the detector, thus we used a model PSF to determine which pixels are still in the linear regime. Then we fitted the PSF only to these pixels. The 70 μm image is not saturated, therefore we simply calculated aperture photometry in IDL using an aperture radius of 16″, sky annulus between 39 and 65″, and an aperture correction of 1.741[2]. We found that the source was point-like at both 24 and 70 μm. Color correction was applied by

[2]MIPS Data Handbook, version 3.2,
available at http://ssc.spitzer.caltech.edu/mips/dh/mipsdatahandbook3.2.pdf

convolving the observed SED with the MIPS filter profiles in an iterative way. The resulting color corrected fluxes can be seen in Table 4.2.

The IRS spectroscopy was carried out in 'staring mode' using the Short Low, the Short High and the Long High modules. Measurements were taken at two different nod positions and at each nod position three exposures were taken. We started from BCD level and extracted spectra from the 2D dispersed images using the Spitzer IRS Custom Extraction software (SPICE). In the case of the Short Low channel we extracted a spectrum from a wavelength dependent, tapered aperture around the star, and also from a sky position. In the case of the high resolution channels, we extracted spectra from the full slit. For the Short High channel, the target was off-slit and most of the stellar PSF fell outside of the slit. We corrected this spectrum for flux loss using the measured IRS beam profiles (for more details, see Sec. 4.6). The resulting complete $5-35\,\mu$m spectrum can be seen in Figs. 4.10 and 4.11.

4.2.5 ISO archival data

ISO measurements of Parsamian 21 at 65 and $100\,\mu$m were obtained in 'oversampled map' (PHT32) mode on 1996 September 28. These observations were reduced using a dedicated software package (P32TOOLS) developed by Tuffs & Gabriel (2003). This tool provides adequate correction for transients in PHT32 measurements. Absolute calibration was done by comparing the source flux with the on-board fine calibration source. In order to extract the flux of our target, a point spread function centered on Parsamian 21 was fitted to the brightness distribution on each map. At $65\,\mu$m the PSF could be well fitted by the ISOPHOT theoretical footprint function. At $100\,\mu$m, however, the source turned out to be extended. In this case the brightness distribution was modeled as the convolution of the standard theoretical footprint function with a two dimensional elliptical Gaussian of $40'' \times 20''$, and a position angle of 114°. The obtained fluxes were color corrected by convolving the observed SED with the ISOPHOT filter profiles in an iterative way. The results are displayed in Table 4.2.

Instrument	Wavelength [μm]	Flux [mJy]
Spitzer/IRAC	3.6	143 ± 8
Spitzer/IRAC	4.5	187 ± 10
Spitzer/IRAC	5.8	303 ± 16
Spitzer/IRAC	8.0	829 ± 42
Spitzer/MIPS	24	5 530 ± 310
Spitzer/MIPS	70	13 300 ± 1 300
ISO/ISOPHOT	65	12 600 ± 1 300
ISO/ISOPHOT	100	14 200 ± 1 900

Table 4.2 Photometry for Parsamian 21. All fluxes are color corrected.

4.3 Results

4.3.1 Broad-band imaging

Figure 4.6 displays the HST/WFPC2 image taken at 0.8 μm. The image reveals the structure of the Parsamian 21 nebula with an unprecedented spatial resolution and detail. We note that strong emission lines associated with the bipolar outflow (see Sect. 4.3.2) are not included in the bandpass, so the HST image provides a clean picture of the reflection nebula. The overall dimensions of the nebula are approximately $60'' \times 20''$. The northern part has a characteristic elliptic, loop-like shape, with the inside of the loop having a relatively low surface brightness. The outer edge of the nebula is rather well-defined, while the inner edge is more fuzzy. The farther end of the loop seems to be closed by a wide, faint SE-NW oriented stripe about $30''$ from the star. The nebula is clearly bipolar, although very asymmetric: the southern part is much less developed than the northern one. We note that while the southeastern arc is more visible close to the star (see the central part of the HST image in Fig. 4.7), the southwestern arc is more visible farther from the star (Fig. 4.6). It is remarkable that field stars are visible both to the north and to the south of Parsamian 21. Supposing that these stars are in the background, this implies that there is no significant difference in the extinction between the northern and southern part.

Fig. 4.7 shows the central parts of the HST/WFPC2 and the VLT/NACO images (note that the innermost $0.57''$ of the HST image is saturated). The bipolar nature of the nebula is most conspicuous at the shortest wavelength (0.8 μm), where all 4 arcs (roughly to the northeast, northwest, southwest and southeast) are visible. In the K_S and H bands the

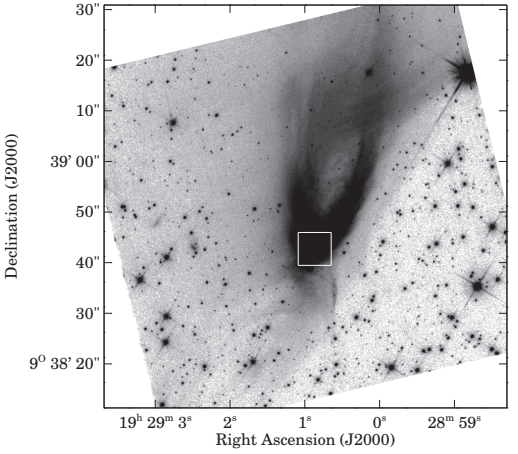

Figure 4.6 HST/WFPC2 image of Parsamian 21 taken through the F814W filter. The intensity scale is square root and brightness increases from light to dark. The white square marks the area shown in the upper left panel of Fig. 4.7.

nebula is more triangle-shaped. In all three NACO bands the central source is extended, with deconvolved sizes of 0.20, 0.12 and 0.08″ in the H, K_S and L′ bands, respectively.

4.3.2 Narrow-band imaging

Figure 4.8 displays the continuum-subtracted H_α image of Parsamian 21. Conspicuous Herbig-Haro knots are seen to the north and the south of the central star. The northern knot is compact, resembling the knot described in Staude & Neckel (1992). The southern knot, however, has a distinctly bowed shape. The southern extent of this knot has a S/N of 10 over background per pixel, while the flanking structures have S/N ≈ 7. The northern knot has S/N in excess of 15 per pixel. To measure the angular distance of the knots from the central star in the H_α imagery, we binned the data in a 3 pixel (1.1″) wide swath oriented north-south. Apart from the residual of the central source, we could identify three knots (see Fig. 4.8): Knots 1, 2 and 3 are located 5″ north, 10.5″ south and 3″ south, respectively. The knots correspond to those identified by Staude & Neckel (1992), but all three knots have moved outwards since then (Fig. 4.9). Assuming a distance of 400 pc, the velocity of

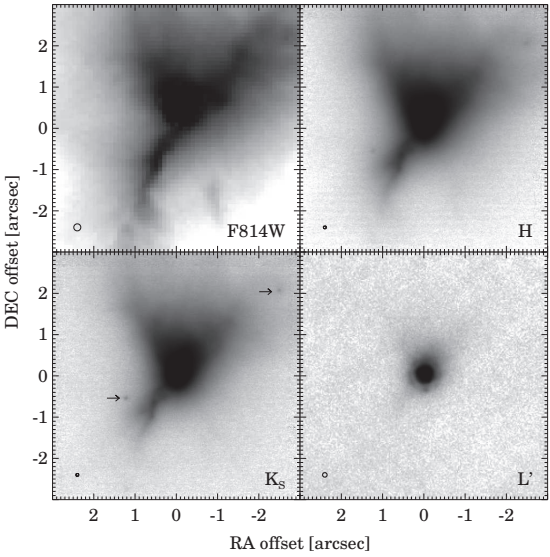

Figure 4.7 HST/WFPC2 (with filter F814W) and VLT/NACO (with filters H, K_S and L′) images of Parsamian 21. Circles at the left bottom corners indicate the FWHM at the center of the corresponding image. In the K_S-band image, arrows mark the positions of the two closest stars to Parsamian 21 (see Sect. 4.4.2).

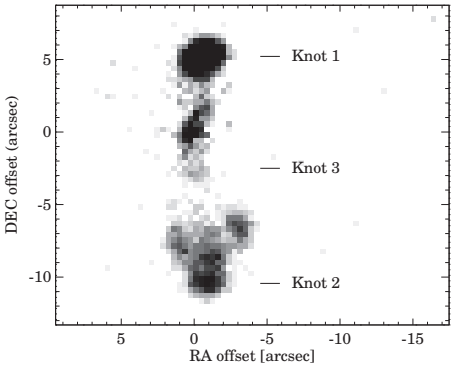

Figure 4.8 Continuum-subtracted H_α image of Parsamian 21. The peak at position (0,0) is the residuum of the central source. Three Herbig-Haro knots could be identified; these were named Knot 1, 2 and 3 by Staude & Neckel (1992).

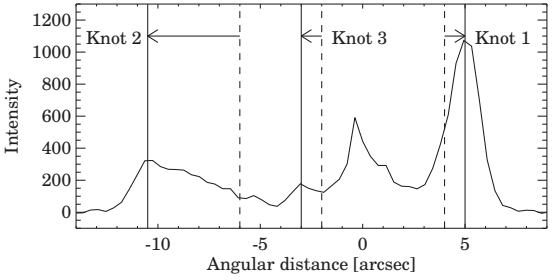

Figure 4.9 South-north oriented cut across Parsamian 21 in the continuum-subtracted H_α image. 0 marks the position of the central star. The peaks marked by solid vertical lines at -10.5, -3 and $5''$ correspond to Knot 2, 3 and 1, respectively. Dashed vertical lines mark the positions of the same knots as measured by Staude & Neckel (1992). Arrows demonstrate the direction where the knots propagate.

the knots along the polar axis is 530 km s^{-1} for Knots 1 and 3, and 120 km s^{-1} for Knot 2. This is in good agreement with the velocities calculated by Staude & Neckel (1992) using radial velocity measurements. Such outflow velocities imply kinematic ages of approximately 180 yr for Knot 1 and 80 yr for Knots 2 and 3.

4.3.3 Spectral energy distribution

Table 4.2 contains our Spitzer and ISO photometry for Parsamian 21. These data, complemented with previously published measurements between 1983 and 1999 are plotted in Fig. 4.10, showing the complete UV-to-mm spectral energy distribution (SED) of the object. Comparing data taken between 1983 and 1999, Ábrahám et al. (2004a) found that there is no long-term flux variation in the $1-100\,\mu$m wavelength range. The new Spitzer data from 2004 reveal that the mid-infrared brightness of Parsamian 21 has stayed constant since then at a 15% level. Although Parsamian et al. (1996) reported $2-3$ mag brightness variations in the B band between 1966 and 1990 (in Fig. 4.10 we plotted optical measurements from 1980 as representative values), no significant flux changes can be seen at longer wavelengths within the measurement uncertainties.

At wavelengths shorter than $3\,\mu$m, the SED is highly reddened (Polomski et al., 2005), probably due to the combined effect of interstellar extinction and self-shadowing by cir-

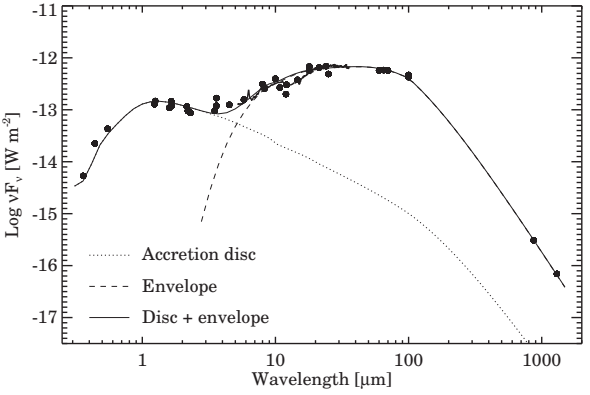

Figure 4.10 Complete UV-to-mm SED of Parsamian 21. Source of data: 2MASS All-Sky Catalog of Point Sources, MSX6C Infrared Point Source Catalog, Ábrahám et al. (2004a), Polomski et al. (2005), Neckel & Staude (1984), Henning et al. (1998), and this work. The model SED is discussed in Sect. 4.4.4.

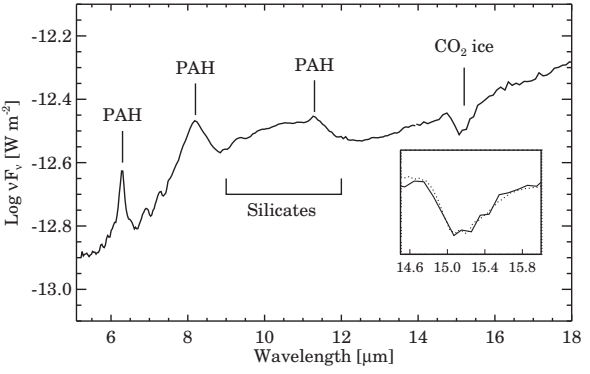

Figure 4.11 $5-18\,\mu$m part of the Spitzer/IRS spectrum of Parsamian 21. The inset displays in details the continuum-subtracted spectral region around the $15.2\,\mu$m CO_2 ice feature of Parsamian 21 with solid line and as a comparison HH 46 IRS with dashed line (for discussion see Sect. 4.4.5).

cumstellar material. The fact that the central source is extended at these wavelengths (see Sect. 4.3.1) indicates that the photometry is contaminated by scattered light from the inner part of the circumstellar environment. Between 3 and 25 μm, the SED is rising towards longer wavelengths as $\nu F_\nu \sim \lambda$. The $5-18\,\mu$m Spitzer spectrum (Fig. 4.11) displays strong PAH emission features at 6.3, 8.2 and 11.3 μm and amorphous silicate emission around 10 μm (Quanz et al. 2007, see also the spectrum of Polomski et al. 2005). Weaker absorption features can also be seen between 7 and 8 μm, which cannot be safely identified with any ice or PAH feature. The $10-19\,\mu$m channel of the Spitzer/IRS spectrum was not shown by Quanz et al. (2007) due to data reduction difficulties. We made an attempt to evaluate also this channel (for details, see Sec. 4.6). As can be seen in the inset of Fig. 4.11, the spectrum shows a strong CO_2 ice absorption feature at 15.2 μm, which has not been reported in the literature so far. Between 25 and 100 μm the SED is flat ($\nu F_\nu \sim$ const.), while the submillimeter shape is $\nu F_\nu \sim \lambda^{-3.5}$ (corresponding to $\beta = 0.5$, assuming optically thin emission and a dust opacity law of $\kappa_\nu \propto \nu^\beta$). Using a distance of 400 pc and an interstellar reddening of $A_V = 2$ mag (Hillenbrand et al., 1992), the bolometric luminosity computed as the integral of the SED from 0.44 to 1300 μm is 10 $L_\odot$ (assuming isotropic radiation field).

4.3.4 Polarimetry

Figure 4.12 shows images of Parsamian 21 calculated from the H-band NACO polarization data, as well as from the 2 μm NICMOS measurements. The left column shows the total intensity (I) obtained as the sum of the intensities of the two orthogonal polarization states. The middle column displays the polarized intensity (PI) calculated as the square root of the quadratic sum of the Q and U Stokes components. The right column shows the degree of polarization (% pol.), i.e. the ratio of the polarized to the total intensity.

The NACO total intensity maps (Fig. 4.12, left) are very similar to the H-band map in Fig. 4.7. Thus, the Wollaston-prism data can reproduce well the direct images taken without the prism. While the total intensity is relatively smooth, the polarized intensity (Fig. 4.12, middle) reveals many fine details not visible in the total intensity map. The most striking feature is a dark horizontal lane across the star, where the polarized intensity is very low. Above this dark lane, high intensity regions can be seen, primarily emphasizing

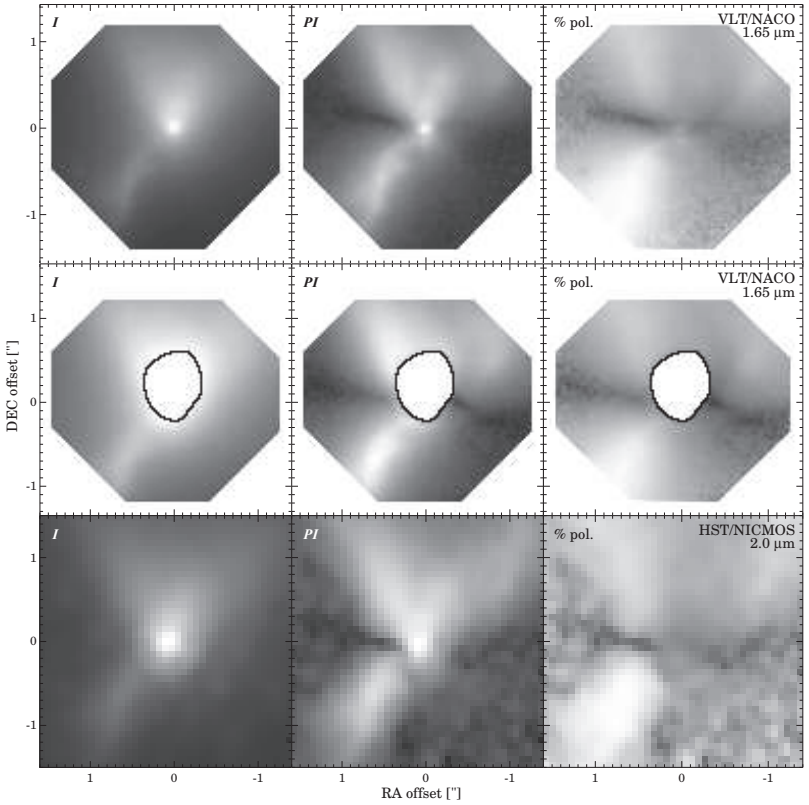

Figure 4.12 *Left:* total intensity (I); *middle:* polarized intensity (PI); *right:* degree of polarization (% pol.). *Upper row:* short exposure H-band NACO images; *middle row:* long exposure H-band NACO images (the saturated central parts are masked out); *lower row:* 2 μm NICMOS images of the same area. The intensity scale is logarithmic and brightness increases from dark to light.

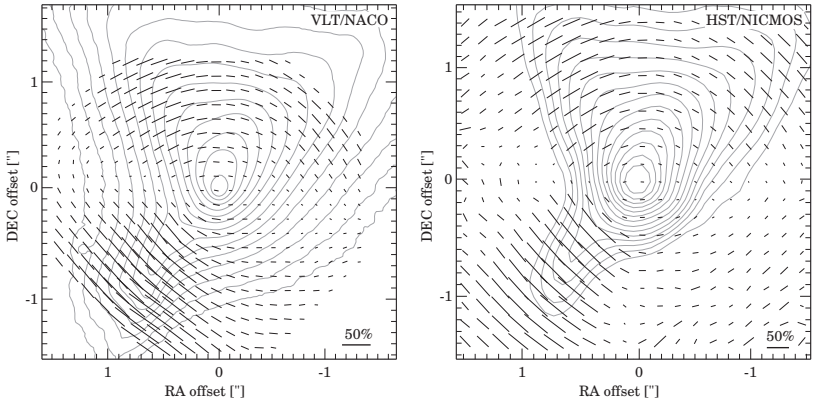

Figure 4.13 Polarization pseudovectors overlaid on intensity contours. *Left:* VLT/NACO, H-band, with 5×5 pixels binning, *right:* HST/NICMOS, $2\,\mu$m, with 2×2 pixels binning.

the walls of the upper lobe. Below the dark lane, the southeastern arc is very pronounced. The degree of polarization (Fig. 4.12, right) again shows features different from the previous two maps. Here, the central star almost disappears, as the stellar light is not polarized. The horizontal dark lane of low polarization across the star is even more pronounced: there the degree of polarization is below $\approx 5\%$ in the H-band NACO images. The polarization of the central source itself, measured in a $0.08''$ radius aperture, is 9% and its position angle is 70° east of north. The long exposure NACO images (Fig. 4.12, middle row), showing the outer regions with higher signal-to-noise ratio, are consistent with the short exposure maps (Fig. 4.12, upper row). It is remarkable that the NICMOS images, which represent independent observations (different resolution, different instrument, different polarization technique), show strikingly similar features, although the degree of polarization is slightly higher.

Figure 4.13 shows the polarization pseudovectors overlaid on total intensity contours. The NACO map, along with the degree of polarization map in Fig. 4.12 right shows that the horizontal band of low polarization across the star is very well-confined, narrow (about $0.15-0.20''$ wide at the 5% polarization level) and can be discerned from 0.12 to $1.2''$ to the star (and likely beyond, as indicated by the long exposure maps, see also the polarization

maps of Draper et al. 1985 and Hajjar et al. 1997). The position angle of this band is $78° \pm 4°$ east of north, consistent with that measured by Draper et al. (1985) ($75° \pm 4°$). This implies that the band in our high spatial resolution images are a direct inward continuation of the band seen by Draper et al. (1985) and Hajjar et al. (1997) in their lower resolution images. The degree of polarization in this band is a few percent, and it is oriented parallel with the band itself.

Most of the northern part of the nebula shows a centrosymmetric pattern, characteristic of reflection nebulae with single scattering. This is consistent with what Draper et al. (1985) and Hajjar et al. (1997) measured for Parsamian 21 itself. It is also similar to what can be seen in other bipolar nebulae (see e.g. Meakin et al. 2005 for nebulae of young stars or Scarrott et al. 1993 for nebulae of evolved stars). The highest polarization in the northern part can be measured in the northeastern wall (25-30%) and also in a spot about $0.9''$ west and $0.6''$ north to the star (20-25%). The southern part of the nebula also follows the regular centrosymmetric pattern seen in the northern part. Here the highest polarization can be found in the southeastern arc (60-70%).

The NICMOS vector map at $2\,\mu$m (Fig. 4.13 right) repeats all the main features seen by NACO in the H-band (Fig. 4.13 left). We note nevertheless the presence of two small, localized depolarization areas on either side of the central source at positions ($0.9''$, $0.0''$) and ($-0.8''$, $-0.1''$).

4.4 Discussion

4.4.1 Parsamian 21: an FU Orionis-type star

Although no optical outburst was ever observed, Parsamian 21 shares many properties characteristic of FUors. Its spectral type in the literature ranges from A5 to F8 supergiant (e.g. Staude & Neckel, 1992), similar to the typical FUor spectral types (F–G supergiant). In addition, it shows strong infrared excess and drives a bipolar outflow, similarly to many FUors. However, in a recent paper by Quanz et al. (2007) the pre-main sequence nature and the FUor status of Parsamian 21 were questioned, mainly because its PAH emission bands are untypical for young stars. They suggest that Parsamian 21 is either an intermediate

α_{2000}	δ_{2000}	H mag	K_S mag	L′ mag
$19^h\ 29^m\ 0.96^s$	$9^\circ\ 38'\ 42.11''$	20.2	19.1	>14.6
$19^h\ 29^m\ 0.70^s$	$9^\circ\ 38'\ 44.78''$	20.6	19.5	>14.4

Table 4.3 VLT/NACO photometry for the two closest stars to Parsamian 21. Uncertainties are about 0.1 mag.

mass FUor object, or an evolved star sharing typical properties with post-AGB stars.

An important parameter which may discriminate between a pre-main sequence object and a post-AGB star is the luminosity. The typical luminosity of post-AGB stars is in the order of $10^3 - 10^4\,L_\odot$ (Kwok, 1993), while FUors are typically fainter than a few $100\,L_\odot$. The luminosity of Parsamian 21, $10\,L_\odot$ (see Sect. 4.3.3), is at least a factor of 100 lower than that of post-AGB stars. Even adopting the largest distance estimate mentioned in the literature (1800 pc, Staude & Neckel 1992), the luminosity of Parsamian 21 is still too low. The observed proper motion of the Herbig-Haro knots, however, prefers the lower distance (400 pc), otherwise the outflow velocities ($\approx$2400 km/s at 1800 pc) would be unusually high for a young stellar object (typically up to 600 km/s, see e.g. Mundt et al., 1987; Hessman et al., 1991b). Moreover, the existence of Herbig-Haro outflows are usually tracers of low-mass star formation (Hughes et al., 1994).

In the following discussion, we consider Parsamian 21 to be a FUor and we discuss its properties in the context of young eruptive stars. Nevertheless we note that most of our results on the morphology and circumstellar structure are valid regardless of the nature of the central object.

4.4.2 Parsamian 21: an isolated young star?

Parsamian 21 is situated close to the Galactic plane ($l = 45.8^\circ$, $b = -3.8^\circ$), in a molecular cloud called Cloud A. This cloud was identified by Dame & Thaddeus (1985) in their CO survey of molecular clouds in the northern Milky Way. The cloud occupies an area of 8 square degrees in the sky, and the only known young star associated with it is the T Tauri star AS 353 (Dame & Thaddeus, 1985).

In order to check whether FUors are usually associated with star forming regions, we searched the literature and found that most FUors are located in areas of active star forma-

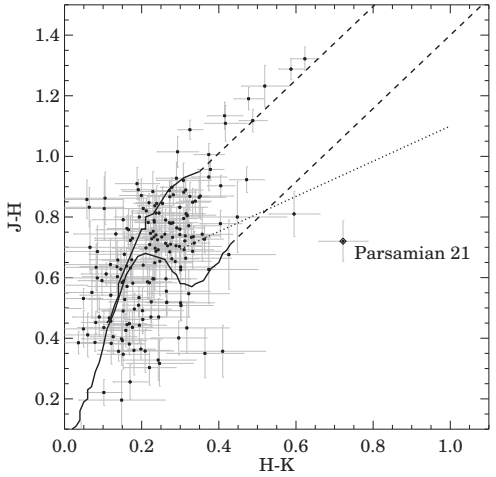

Figure 4.14 2MASS color-color diagram of 188 sources in an area of $5.3' \times 5.3'$ centered on Parsamian 21. The main-sequence and giant branch are marked by solid lines (Koornneef, 1983), the reddening path with dashed lines (Cardelli et al., 1989) and the T Tauri locus with dotted line (Meyer et al., 1997).

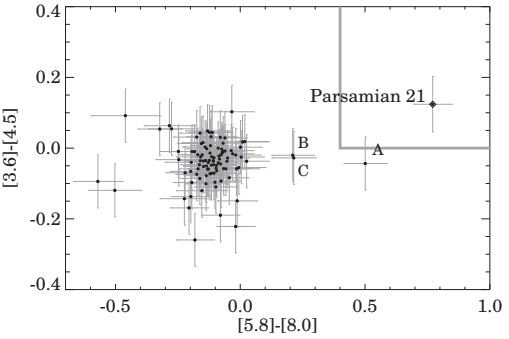

Figure 4.15 IRAC color-color diagram of 100 sources located in the same area as in Fig. 4.14. The gray square in the upper right corner marks the approximate domain of Class II sources (Allen et al., 2004).

tion (e.g. Henning et al., 1998). To find out whether there is star formation in the vicinity of Parsamian 21, we searched for pre-main sequence stars. For this purpose we constructed a 2MASS J−H vs. H−K_S and an IRAC [3.6]−[4.5] vs. [5.8]−[8.0] color-color diagram for sources found in our $5.3' \times 5.3'$ IRAC field of view (Fig. 4.14, 4.15). Our selection criteria in the case of 2MASS was S/N > 10 and uncertainties < 0.1 mag in all J, H and K_S bands, while in the case of IRAC S/N > 3 and detectability at all four bands was required. The 2MASS diagram revealed that most of the nearby objects are reddened main sequence or giant stars. On the IRAC diagram, however, there are three objects (apart from Parsamian 21 itself), which display infrared excess at 8 μm (marked by A, B and C in Fig. 4.15). According to the classification of Allen et al. (2004), Class II sources exhibit colors of [3.6]−[4.5] > 0.0 and [5.8]−[8.0] > 0.4, thus one of these stars (A) might be a Class II source, while B and C are more likely Class III/main sequence sources. The nature of source A and its possible relationship to Parsamian 21 is yet to be investigated. Nevertheless, Parsamian 21 seems to be rather isolated compared to most FUors and certainly not associated with any rich cluster of young stellar objects.

We also searched for possible close companions of Parsamian 21 in the WFPC2 and NACO direct images. In order to establish a detection limit for source detection, we measured the sky brightness on the NACO images (before sky-subtraction), and estimated a limiting magnitude for each filter. The resulting values are 22.8, 21.6, and 15.2 mag in H, K_S and L′, respectively. In case of the HST/WFPC2 image, the larger ($80'' \times 80''$) field of view made it possible to estimate a limiting magnitude using star counts; the resulting value is 23.5 mag. Due to the bright reflection nebula, the detection limit is somewhat lower close to the star. The two closest objects we found are the following: one star to the southeast, at a distance of 1.4″ (560 AU at 400 pc), and another one to the northwest, at a distance of 3.3″ (1320 AU at 400 pc). These sources are marked with arrows in Fig. 4.7. Neither of the stars are visible at 3.8 or 0.814 μm, although we can give an upper limit for their L′ brightness. Their positions and photometry are given in Table 4.3. As these sources are very red, they can equally be heavily reddened background stars, or stars with infrared excess (indicating that they might be associated with Parsamian 21). Supposing that they are reddened main sequence stars, one can estimate an extinction of $A_V \approx 10 - 15$ mag. Further multifilter observations may

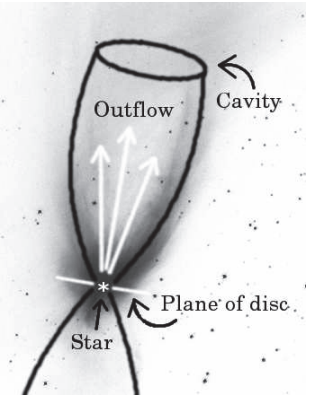

Figure 4.16 Sketch of the morphology of circumstellar material around Parsamian 21, overlaid on the HST/WFPC2 image. The central star is surrounded by an edge-on disk. Perpendicular to the disk, the star drives a bipolar outflow that excavates an outflow cavity in the dense circumstellar material. Light from the central star illuminates the walls of the cavity.

help to clarify the nature of these objects and their possible relationship to Parsamian 21.

4.4.3 The circumstellar environment of Parsamian 21

The appearance and polarization properties of the nebula around Parsamian 21 can be understood in the following way: the star drives an approximately north-south oriented bipolar outflow, which had excavated a conical cavity in the dense circumstellar material (Fig. 4.16). The star illuminates this cavity and the light is scattered towards us mainly from the walls of the cavity. The outflow direction is perpendicular to an almost edge-on dense circumstellar disk. This picture is supported by the following facts: (a) the centrosymmetric polarization pattern is characteristic of reflection nebulae with single scattering; (b) the morphology and limb brightening suggest a hollow cavity (as opposed to an "outflow nebula", where the lobes are composed of dense material ejected by the central source); and (c) the low-polarization lane across the star strongly suggests the presence of an edge-on circumstellar disk, where multiple scattering occurs. In general the Parsamian 21 system shows similarities to the NGC 2261 nebula associated with R Mon.

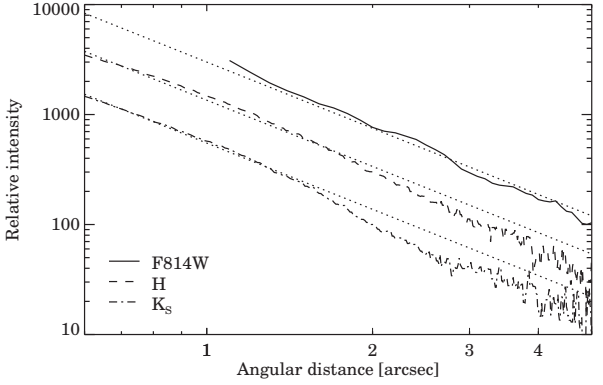

Figure 4.17 Brightness profiles of Parsamian 21 at 0.8 μm and in the H and K_S bands. Dotted lines mark Hubble's relation.

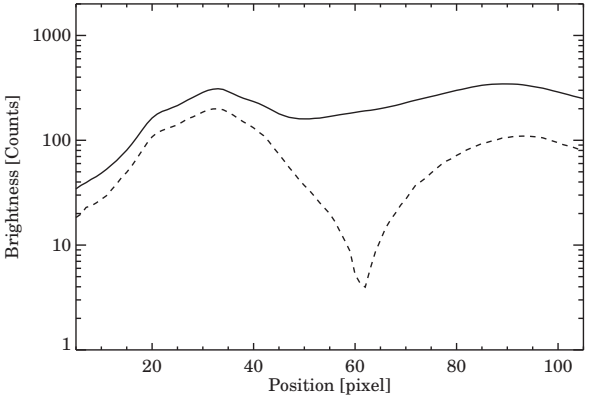

Figure 4.18 South-north cut at 0.6″ east from the star. *Solid line:* total intensity; *dashed line:* polarized intensity.

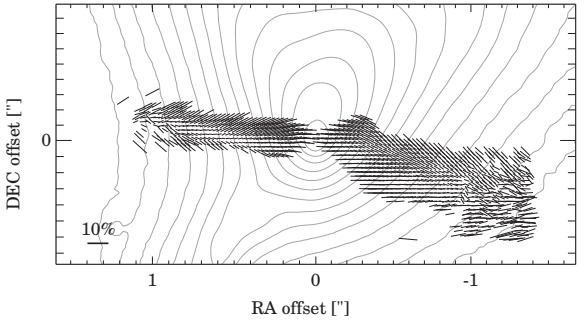

Figure 4.19 VLT/NACO polarization map of Parsamian 21 overlaid on H-band total intensity contours. Polarization vectors are displayed at full resolution, only showing the central low polarization band, where the polarization vectors are aligned. Such arrangement is expected when multiple scattering occurs in an edge-on disk.

Envelope/Cavity

We characterised the opening of the upper lobe by marking the ridge along the northeastern and northwestern arcs which we interpret as the walls of the cavity. As viewed from the star northwards, the cavity starts as a cone with an opening angle of $\approx 60°$, giving the nebula in Fig. 4.7 a characteristic equilateral triangle-shape. Farther away from the star the cavity deviates from the conical shape, becomes narrower. The whole cavity occupies an area of $8\,000 \times 24\,000$ AU (at a distance of 400 pc). The sharp outer boundary of the nebula implies a significant density contrast between the cavity and the surrounding envelope.

In Fig. 4.17 we plotted radial brightness profiles at 0.8 μm and in the H and K_S bands, starting from the star northwards. The slope of the intensity profiles in the inner $\sim 1.6''$ (640 AU) follows closely Hubble's relation (Hubble, 1922), i.e. the brightness is proportional to r^{-2}. This trend can be clearly followed above the noise out to about $5''$ in our H and K_S images, giving an estimate of 2000 AU for the outer size of the envelope. The fact that the brightness profiles follow Hubble's relation implies that the nebula is produced by isotropic single scattering, in accordance with the centrosymmetric polarization pattern and the high degree of polarization. Around $\sim 1.6''$ the profiles becomes steeper, probably due to decreased density in the inside of the cavity. Similar steepening in the outer part of the

nebula was already mentioned by Li et al. (1994). The profiles are similar at all observed wavelengths and do not show significant dependence on the position angle.

Disk

As mentioned in Sect. 4.3.4, both the NACO and NICMOS polarimetric images show a lane of low polarization oriented nearly east-west across the star (Fig. 4.12). The drop in the degree of polarization can also be clearly seen in Fig. 4.18, where a north-south cut at 0.6″ east to the star is plotted. The low polarization can be explained by multiple scattering in an edge-on disk (Bastien & Ménard, 1990). According to models of such circumstellar structures (e.g. Whitney & Hartmann, 1993; Fischer et al., 1996) the polarization vectors are oriented parallel to the disk plane. As can be seen in Fig. 4.19, despite the low degree of polarization, the predicted alignment of the vectors can be clearly seen in the case of Parsamian 21, too. The NICMOS polarization map shows a similar effect. The dark lane in Fig. 4.12 can be followed inwards to as close as 48 AU from the star. This is an upper limit for the inner radius of the circumstellar disk.

An interesting feature of the mentioned models is the presence of two depolarized areas on either side of the central star, which mark the outer end points of an edge-on disk. The depolarization is due to a transition from the linearly aligned to the centro-symmetic polarization pattern. These depolarized areas can be seen in Fig. 4.13 right, on both sides at about 0.9″ from the star. At the distance of Parsamian 21 this corresponds to 360 AU, and can be adopted as the outer radius of the dense part of the disk, where multiple scattering at near-infrared wavelengths is dominant. It is interesting that the NACO map does not show clear depolarized areas at the same position, but seems to resolve the transition in vector orientation, while the larger beam of NICMOS averaged the differently oriented vectors, resulting in depolarized spots.

Figure 4.12 suggests a slight asymmetry in the dense disk: the eastern (left) side is straight, while the western (right) side shows a kink and also has a different position angle than that on the other side. The thickness of the disk can be measured on the area where the polarization vectors are aligned (Fig. 4.19). This approximately corresponds to the area where the degree of polarization is below $\approx 10\%$. The resulting thickness is $0.05''-0.1''$

(20−40 AU) to the east and is somewhat larger, 0.15″−0.2″ (60−80 AU), to the west. If the inclination is not exactly 90°, these values give an upper limit for the thickness of the circumstellar disk around Parsamian 21. The thickness does not show significant increase with radial distance, suggesting the picture of a flat, rather than a flared disk, at least considering the dense, multiple-scattering part. The smooth brightness and polarization distribution between the disk and the surrounding envelope (Fig. 4.18), however, implies that there is a continuous density transition between the two components. From the ratio of the horizontal to vertical sizes of the disk a lower limit of 84° for the inclination of the system (the angle between the normal of the disk and the line of sight) can be derived.

Fischer et al. (1996) computed a grid of polarization maps of young stellar objects with the aim of helping the interpretation of polarimetric imaging observations. They consider five different models, four with massive, self-gravitating disks and one with a massless Keplerian disk. Since the mass of circumstellar material of Parsamian 21 derived from submillimeter observations is relatively low ($< 0.3\,M_\odot$, Henning et al. 1998; Polomski et al. 2005; Sandell & Weintraub 2001; Hillenbrand et al. 1992), the most appropriate model for our case is a Keplerian disk. Indeed the polarization pattern as computed by Fischer et al. (1996) for an inclination of 87° (their Fig. 1) looks remarkably similar to our Fig. 4.13 (the differences might be explained by the narrower cavity and flatter disk of Parsamian 21). Thus, the geometry and structure assumed by Fischer et al. (1996) in their Keplerian model could be a good starting point for further radiative transfer modelling of Parsamian 21.

4.4.4 Modelling the circumstellar environment

Our observations provide some direct measurements of the geometry of the circumstellar structure (disk size and thickness, inclination, envelope size). In the following we discuss the consistency of this picture with the observed SED. Our approach is to construct a simple disk+envelope model, in which we fix those parameters whose values are known from our NACO observations. Then we check whether the SED can be fitted by tuning the remaining parameters. We adopted an analytical disk model (Adams et al., 1987), which has been successfully used to model FUors (Quanz et al., 2006; Ábrahám et al., 2006). Our model consists of two components, an optically thick and geometrically thin accretion disk

Parameter	Variable	Value
Inner disk radius	R_1	$3.5\,R_\odot$
Outer disk radius	R_2	*360 AU*
Temperature at 1 AU	$T_{\rm d,0}$	284 K
Power-law index for temperature	$q_{\rm d}$	*0.75*
Power-law index for surface density	$p_{\rm d}$	1.5
Disk mass	$M_{\rm d}$	*0.02* $M_\odot$
Inclination	i	*86°*
Inner envelope radius	R_3	5 AU
Outer envelope radius	R_4	*2000 AU*
Temperature at 5 AU	$T_{\rm e,0}$	410 K
Power-law index for temperature	$q_{\rm e}$	*0.4*
Power-law index for surface density	$p_{\rm e}$	0.4
Envelope mass	$M_{\rm e}$	$0.02\,M_\odot$
Interstellar Extinction	A_V	*2 mag*

Table 4.4 Model parameters for Parsamian 21. Parameters in italics are fixed, while the others were fitted.

(Shakura & Sunyaev, 1973) and an optically thin envelope. No central star is included in the simulation, partly because in outbursting FUors the star's contribution is negligible compared to that of the inner disk (Hartmann & Kenyon, 1996), and partly because of the edge-on geometry where the star is obscured by the disk. This assumption is supported by the fact that the shape of the SED at optical wavelengths is broader than a stellar photosphere.

The temperature and surface density distribution in the disk are described by power-laws:

$$T(r) = T_{\rm d,0}\left(\frac{r}{1\,{\rm AU}}\right)^{-q_{\rm d}}, \tag{4.13}$$

$$\Sigma(r) = \Sigma_{\rm d,0}\left(\frac{r}{1\,{\rm AU}}\right)^{-p_{\rm d}}. \tag{4.14}$$

Similar power-laws were assumed for the envelope. The observed flux at a specific frequency is given by

$$F_\nu = \frac{\cos i}{D^2}\int_{\rm R1}^{\rm R2} 2\pi r(1-e^{\frac{-\Sigma_{\rm d}\kappa_\nu}{\cos i}})B_\nu(T_{\rm d}){\rm d}r + \tag{4.15}$$

$$\frac{1}{D^2}\int_{\rm R3}^{\rm R4} 2\pi r(1-e^{-\Sigma_{\rm e}\kappa_\nu})B_\nu(T_{\rm e}){\rm d}r. \tag{4.16}$$

The first term describes the emission of the accretion disk, the second term describes the

radiation of the optically thin envelope. For the dust opacity we used a constant value of $\kappa_\nu = 1$ cm^{2}g^{-1} at $\lambda > 1300\,\mu$m, $\kappa_\nu = \kappa_{1300\mu\mathrm{m}} \frac{\lambda}{1300\mu\mathrm{m}}$ between 1300 and 100 μm and again a constant value of $\kappa_\nu = \kappa(100\,\mu\mathrm{m})$ at $\lambda < 100\,\mu$m. For the description of the parameters and their best-fit values, see Table 4.4. The fitted model SED as well as the disk and envelope components are overplotted in Fig. 4.10.

The model SED is consistent with the observed fluxes. This shows that the picture of a thin accretion disk and an envelope is consistent with both our polarimetric observations and the measured SED. Detailed modelling of the silicate, PAH, and ice spectral features would require radiative transfer modelling, which is beyond the scope of this paper.

4.4.5 The evolutionary status of Parsamian 21

The geometry of FUor models discussed in the literature (e.g. Hartmann & Kenyon 1996; Turner et al. 1997) usually consists of a central star surrounded by an accretion disk and an infalling envelope with a wind-driven polar hole. These assumptions are supported by the fact that they fit well the SED (Green et al., 2006; Quanz et al., 2007), the interferometric visibilities (Millan-Gabet et al., 2006; Ábrahám et al., 2006) and the temporal evolution of the SED (Ábrahám et al., 2004a). In this paper we present the first direct imaging of these circumstellar structures in a FUor. Our polarimetric measurements of Parsamian 21 show the existence of a circumstellar disk which extends from at least 48 to 360 AU. The most striking feature of the disk is its flatness over the whole observed range. The short-wavelength part of the SED could be well reproduced using a radial temperature profile of $r^{-0.75}$ (Sect. 4.4.4). This profile is expected from both a geometrically thin accretion disk and a flat reprocessing disk. An envelope was also seen in the polarization maps of Parsamian 21 and it was also a necessary component for the SED modelling. Envelopes are involved in many FUor models and in this paper we present a direct detection of this model component. Our images reveal that the envelope can be followed inwards as close to the star as the disk. The temperature profile of $r^{-0.53}$ resulted from the SED modelling is typical of circumstellar envelopes. FUor models often assume a polar cavity in the envelope, created by a strong outflow or disk wind. The direct images of Parsamian 21 clearly show the presence of such a cavity and we also detected a bipolar outflow in the Parsamian 21 system.

As new interferometric and infrared spectroscopic observations were published for FUors, the group turned out to be more inhomogeneous in physical properties than earlier assumed, when mainly optical photometry and spectroscopy had been available. Quanz et al. (2007) proposed that some differences might be understood as an evolutionary sequence. They suggest that FUors constitute the link between embedded Class I objects and the more evolved Class II objects. Members of the group exhibiting silicate absorption at 10 μm are younger and more embedded (Category 1, e.g. V346 Nor); while objects with pure silicate emission are more evolved (Category 2, e.g. FU Ori and Bran 76). There are objects showing a superposition of silicate absorption and emission, which are probably in an intermediary evolutionary stage (e.g. RNO 1B). Green et al. (2006) also sorted FUors, based on the ratio of the far-infrared excess and the luminosity of the central accretion disk, f_d (Equ. 7 in their paper). A large relative excess ($f_d > 5\%$) indicates an envelope of large covering fraction (V1057 Cyg and V1515 Cyg), while low relative excess means a tenuous or completely missing envelope (Bran 76 and FU Ori). This is also an evolutionary sequence, as young, more embedded objects have large envelopes, while around more evolved stars, the envelope has already dispersed. f_d can also be used to calculate the opening angle of the envelope, thus a prediction of this scheme is that the opening angle is becoming wider during the evolution, probably due to strong outflows during the repeated FUor outbursts.

The two classification schemes are not inconsistent and one can merge them into the following evolutionary sequence: (1) the *youngest objects* exhibit silicate absorption and large far-infrared excess (V346 Nor, probably also OO Ser and L1551 IRS 5 belong here); (2) *intermediate-aged objects*, where the silicate feature is already in emission but there is still a significant far-infrared excess (V1057 Cyg, V1515 Cyg, probably also RNO 1B and V1647 Ori); (3) the most *evolved objects* show pure silicate emission and low far-infrared excess (FU Ori, Bran 76). We note, however, that this classification has some weak points. As Quanz et al. (2007) already mentioned, an edge-on geometry in a more evolved system may appear as a younger one. Moreover, during an outburst and the subsequent fading phase, certain spectral features as well as the global shape of the SED may change.

Parsamian 21 can be placed in this evolutionary scheme, though one should keep in mind that because of the nearly edge-on geometry, the classification of this object is somewhat

uncertain. Parsamian 21 displays silicate emission (Fig. 4.11). Integrating the flux of the two components in our simple model (Sect. 4.4.4), and correcting the apparent disk luminosity for inclination effect ($i = 86°$, Table 4.4) using Equ. 6 of Green et al. (2006), we obtained a large relative far-infrared excess of $f_d = 75\%$. These two properties place Parsamian 21 into the intermediate-aged category (though because of its inclination, it may actually seem younger than it is). Following Equ. 7 of Green et al. (2006), from the f_d value, we also computed the opening angle of the envelope. The resulting opening angle of 60° agrees well with the angle measured in the direct NACO images (Sect. 4.4.3).

Parsamian 21 was placed into the evolutionary scheme using two parameters: the silicate feature and the relative far-infrared excess. In the following we discuss whether its other physical characteristics match with those of other FUors.

(i) Our observations revealed that the circumstellar disk of Parsamian 21 is very flat. Due to lack of similar direct measurements for other FUors, we can only speculate that perhaps all FUors with envelopes have such flat disks. On the other hand, the most evolved FUor, FU Ori, seems to have no envelope but its disk is probably flared (Kenyon & Hartmann, 1991; Green et al., 2006; Quanz et al., 2006). This might suggest that disk flaring develops at later stages, when illumination from the central source may heat the disk surface more directly.

(ii) In a nearly edge-on system like Parsamian 21, one expects to see the 10 μm silicate feature in absorption. The fact that Parsamian 21 has silicate emission indicates that the line of sight towards the central region is not completely obscured. Using the optical depth of the 15.2 μm CO_2 ice feature, we calculated an $A_V = 8$ mag ($A_V = 38.7 A_{15.2\mu m}$, Savage & Mathis 1979). This value is surprisingly low compared to V1057 Cyg ($A_V \sim 50 - 100$ mag, Kenyon & Hartmann 1991). This indicates a much more tenuous envelope, which is also supported by the low envelope mass of 0.02 $M_\odot$ in our modelling.

(iii) Following Quanz et al. (2007), we analysed the profile of the 15.2 μm CO_2 ice feature of Parsamian 21. The inset in Fig. 4.11 shows that the feature has a characteristic double-peaked sub-structure, very similar to HH 46 IRS, an embedded young source

(Boogert et al., 2004). HH 46 IRS is a reference case for processed ice. The presence of processed ice in Parsamian 21 indicates heating processes and the segregation of CO_2 and H_2O ice, already at this evolutionary stage. Other FUors exhibiting this kind of profile are L1551 IRS 5, RNO 1B and RNO 1C (Quanz et al., 2007).

The evolutionary state of a young stellar object can also be estimated following the method proposed by Chen et al. (1995). According to their Equ. (1) we calculated a bolometric temperature of $T_{bol} = 410\,K$ for the measured SED. We compared this value with the distribution of corresponding values among young stellar objects in the Taurus and Ophiuchus star forming regions (Chen et al. 1995). From this check we can conclude that Parsamian 21 seems to be a Class I object, and its age is $\sim 10^5\,yr$. However, Green et al. (2006) argued that the apparent SED of the disk component depends on the inclination. Thus we computed T_{bol} also for a face-on disk configuration and obtained $T_{bol} = 1160\,K$, corresponding to a Class II object. In fact, Parsamian 21 is probably close to the Class I / Class II border, in accordance with the proposal of Quanz et al. (2007).

4.5 Summary

We present the first high spatial resolution near-infrared direct and polarimetric observations of Parsamian 21, with the VLT/NACO instrument. We complemented these measurements with archival infrared observations, such as HST/WFPC2 imaging, HST/NICMOS polarimetry, Spitzer IRAC and MIPS photometry, Spitzer IRS spectroscopy as well as ISO photometry. Our main conclusions are the following:

(1) We argue that Parsamian 21 is probably an FU Orionis-type object;

(2) Parsamian 21 is not associated with any known rich cluster of young stars;

(3) our measurements reveal a circumstellar envelope, a polar cavity and an edge-on disk; the disk seems to be geometrically flat and extends from at least 48 to 360 AU from the star;

(4) the SED can be successfully modeled with a circumstellar disk and an envelope;

(5) within the framework of an evolutionary sequence of FUors proposed by Quanz et al. (2007) and Green et al. (2006), Parsamian 21 can be classified as an intermediate-aged object.

4.6 Refined calibration of the Spitzer/IRS beam profiles

In those cases when the source is not well centered in the slit, part of the stellar PSF falls outside of the slit, leading to flux loss. When the precise absolute flux level of the spectrum is important, one should correct for this effect. Correction for this kind of flux loss is not implemented in the Spitzer data reduction pipeline. For point sources flux loss in off-centered sources can be efficiently corrected if one knows the beam profiles of the different IRS slits. In order to construct the beam profiles for all four IRS slits, I reduced and analysed dedicated IRS calibration measurements taken in spectral mapping mode in a regular grid. Table 4.5 shows a log of these calibration measurements. I used the pipeline processed post-BCD files (pipeline version S14.0.0). At each spatial position, I divided the measured spectrum with a synthetic MARCS model spectrum appropriate for the measured star (Decin, 2005). The result is a data cube with two spatial dimensions and one wavelength dimension. We resampled these data cubes to finer spatial grid and smoothed them in wavelength.

I checked whether the measured beam profiles are consistent with the PSFs provided by Spitzer's Tiny Tim (J. Krist). In Fig. 4.21 I plotted the ratio between the observed and the model spectrum at different distances from the slit center at a certain wavelength. I found slight differences: the measured profiles were in general narrower than the model PSFs, and in some cases they were not centered in 0. I examined several effects that can cause a difference between the model and the measured profiles and we found that the differences can be attributed to pixelization effects (pixel sizes are 1.8″ for SL, 2.3″ for SH, 5.1″ for LL and 4.5″ for LH) and to small (few tenths of arcsecond) uncertainties in the exact position of the calibration star with respect to the slit. Based on the analysis, I decided to use the measured profiles to correct the science measurements, and to use the Tiny Tim model profiles to estimate the uncertainty of the correction. Using this correction, the absolute flux level of IRS spectra has an uncertainty of 10%, but individual measurements can be much more precise if the source is well-centered in the slit and the necessary correction is small.

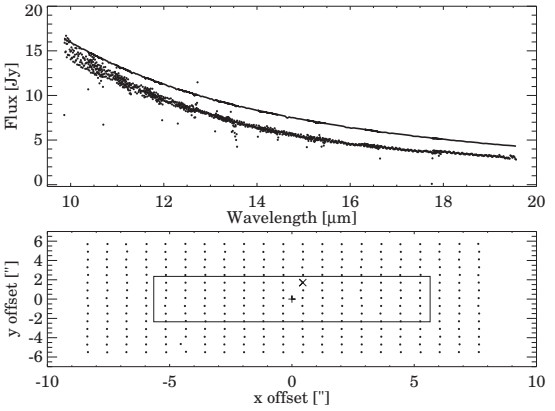

Figure 4.20 *Top:* Dots show the measured spectrum of HR 6688, obtained with Spitzer/IRS through the Short High slit; the continuous line shows a model spectrum of the same star (from Decin, 2005). *Bottom:* Scheme of the data grid; the + sign marks the slit center; dots show the position of the star relative to the slit center; the rectangle indicates the slit itself; the × sign marks the position where the spectrum plotted in the top panel was taken.

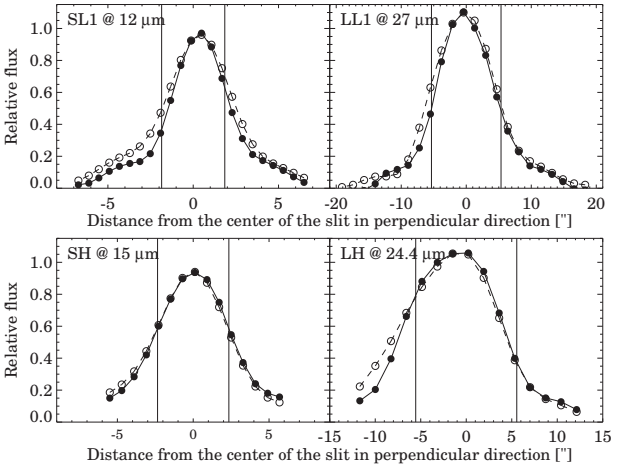

Figure 4.21 Beam profiles of the four Spitzer/IRS channels, perpendicular to the slit, at selected wavelengths. Filled dots show the measured profile, while open dots indicate the pixelized model PSF.

Channel	AOR	Date	Target
Short Low	16295168	2005-Nov-21	HR 7341
	19324160	2006-Jul-5	HR 7341
Short High	16294912	2005-Nov-21	HR 6688
Long Low	16463104	2005-Dec-19	HR 6606
Long High	16101888	2005-Oct-18	HR 2491

Table 4.5 Log of IRS calibration measurements.

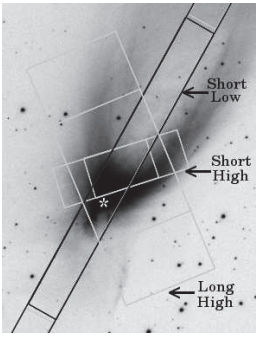

Figure 4.22 Positions of the Spitzer/IRS slits with respect to Parsamian 21 (marked with an asterisk). Black rectangle: Short Low, small grey rectangle: Short High, big grey rectangle: Long High.

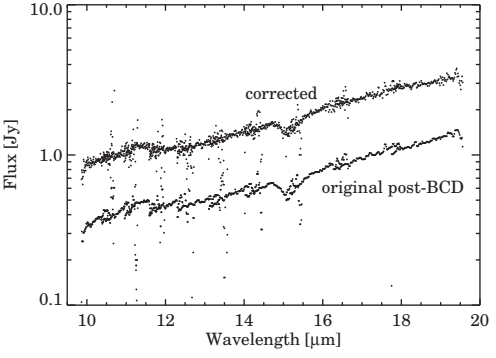

Figure 4.23 Short High channel spectrum of Parsamian 21.

Figure 4.22 shows the position of the IRS slits overplotted on the HST/WFPC2 image of Parsamian 21. While the target is well-centered in the Short Low slit, it is slightly off-centered in the Long High and it is practically off-slit in the Short High. Considering my measured beam profiles, I found that no correction is necessary in the Short Low channel, a small correction (5−20%, depending on wavelength) is necessary in the Long High channel, and a significant correction must be made in the Short High channel, where the corrected flux is approximately 3-4 times the original one (see Fig. 4.23). After the correction, the different IRS channels match fairly well in the overlapping wavelength regimes.

I calculated new correction data cubes for the current pipeline (S15.3.0 as of 2008 March). These data cubes, along with a detailed description on how I obtained them and how they can be used to correct IRS observations, became part of the official Spitzer website at the Spitzer Science Center and is available for the whole astronomy community at the following place:

`http://ssc.spitzer.caltech.edu/irs/calib/calspf/irs_beamprofiles.html`.

Chapter 5

Summary

Scientific goals

A number of issues are still open concerning the circumstellar structure of young eruptive stars. Do all low-mass young stars undergo FUor/EXor-type eruptions? Are FUor-type outbursts recurrent? What can trigger the eruption? Do all young eruptive stars have similar circumstellar structures? How do they evolve?

Current FUor models are usually based on fitting the spectral energy distribution and the optical light curve of the object. However, the geometry usually cannot be determined unambiguously from the modeling, thus, direct observations of the circumstellar environment would be desirable. It is also an open question whether all FUors have companions.

My aim was to contribute to the solution of the above questions and to obtain more information about the FUor phenomenon. For this purpose, I documented and analysed the outburst of two young eruptive stars, *OO Ser* and *V1647 Ori* at optical-infrared wavelengths. I also analysed high-resolution observations of *Parsamian 21*, a FUor system with an edge-on disk. In my dissertation I present a thorough analysis of these three individual young eruptive stars. Taking into account the small number of known FUors and EXors, these results may contribute to the general understanding of this interesting phase of pre-main sequence evolution.

Methods

I used optical and infrared data to study the circumstellar properties and evolution of the three aforementioned young eruptive stars. For V1647 Ori, ground-based data were mainly obtained at the Piszkéstető Mountain Station (Hungary) and at the Teide Observatory (Canary Islands) with the involvement of several observers. When higher spatial resolution information was necessary, I analysed VLT/NACO differential polarimetric data for Parsamian 21, obtained within the framework of our ESO observing proposal. For OO Ser and Parsamian 21, I used mid- and far-infrared archival data from the *Infrared Space Observatory* (ISO) and the *Spitzer Space Telescope*. In the case of Parsamian 21, I also utilized archival *Hubble* observations.

For data reduction, usually the standard methods appropriate for the given instrument were followed. For the ISO photometry, VLT/NACO differential polarimetry, and Spitzer/IRS spectroscopy, however, I also developed new algorithms.

Most of these data were taken with international front-line instrumentation. I combined them in order to construct a spectral energy distribution of each object discussed in this work. Then, I compared the results to predictions of the standard outburst model of young eruptive stars (Bell et al. 1995, ApJ 444, 376; Hartmann & Kenyon 1996, ARA&A 34, 207), and estimated the values of different physical parameters.

Theses

The outburst of the eruptive young star OO Serpentis between 1995 and 2006 (A&A 470, 211–219, 2007)

(1) Based on archival ISO data and new observations, I documented and analysed the brightness evolution of OO Ser during its outburst between 1995 and 2006. I compared the pre-outburst fluxes with the outburst spectral energy distribution and found that the outburst caused brightening not only at 2.2 μm (where the outburst was discovered), but at all infrared wavelengths between 2.2 and 100 μm. My analysis revealed that the fading of the source is still ongoing, and OO Ser will probably not return to

quiescence before 2011. The flux decay has become slower since the outburst peak and has been practically wavelength-independent.

(2) I analysed the physical parameters and evolutionary status of OO Ser. Based on its spectral energy distribution and bolometric temperature, OO Ser seems to be an early Class I object, with an age of $< 10^5$ yr. The outburst timescale (at least 16 years) and the moderate luminosity (4.5 $L_\odot$ before the outburst and $\approx$31 $L_\odot$ at peak brightness) suggest that the object is different from both FUors and EXors, and shows more similarities with V1647 Ori.

(3) I compared the available observations with a widely accepted model of young eruptive stars (Bell et al. 1995), and concluded that the object is probably surrounded by an accretion disk and a dense envelope. This picture is also supported by the wavelength-independence of the fading. However, due to the shorter timescales, outburst models developed for FUors can only work for OO Ser if the viscosity parameter in the circumstellar disk is set to an order of magnitude larger value than usual for FUors.

The 2004–2006 Outburst and Environment of V1647 Ori (AJ 133, 2020-2036, 2007)

(4) I contributed to the optical monitoring of V1647 Ori, and analysed the brightness evolution and colors of the central source and the nebula around it. My results are:

4/1 The brightness of V1647 Ori stayed more than 4 mag above the pre-outburst level for about two years. Using observations obtained at Piszkéstető, I reported the beginning of its rapid fading in 2005 October (Kóspál et al. 2005, IBVS 5661, 1).

4/2 By calculating the time delay between the brightness variations of the star and a nebular position, I determined an angle of 61° between the axis of the nebula and the line of sight.

4/3 From the J–H and H–K_S color maps of the infrared nebula I derived the presence of a circumstellar envelope whose largest extension is about 18″ (0.03 pc).

(5) Based on our optical and near-infrared spectra obtained at different epochs during the outburst, I analysed the temporal variation of a number of spectral features. The observed decrease of line flux of the hydrogen lines can be interpreted as a decrease in the accretion rate of about an order of magnitude between the peak brightness and the quiescence. An interesting result is that the CO band head emission at 2.2 μm was observable during the outburst, but is not present in our quiescent spectrum.

(6) I compared the observed properties of V1647 Ori with the predictions of the thermal instability model of Bell et al. (1995), and concluded that this model reproduces most observational results, but one order of magnitude higher than usual disk viscosity parameter has to be assumed. I argue that V1647 Ori might belong to a new class of young eruptive stars, defined by relatively short timescales, recurrent outbursts, modest increase in bolometric luminosity and accretion rate, and an evolutionary state earlier than that of typical FUors.

Notes: Most of the results presented in Acosta-Pulido et al. (2007) are the joint work of the co-authors and it is very difficult to precisely separate the contribution of each co-author. In the theses and in the dissertation I only presented results where I made a significant contribution.

High-resolution polarimetry of Parsamian 21: revealing the structure of an edge-on FU Ori disc (MNRAS 383, 1015–1028, 2008)

(7) I studied the stars in the vicinity of Parsamian 21 in the optical and near-infrared color-color diagrams, and found that Parsamian 21, unlike many other FUors, is rather isolated and is not associated with any known rich cluster of young stars. I found no close companion which could have triggered an eruption.

(8) From our direct and polarimetric observations I proved the presence of a circumstellar envelope, a polar cavity in the envelope and an edge-on disk. The disk seems to be geometrically flat and extends from at least 48 to 360 AU. The disk is surprisingly flat, its thickness is at most 80 AU, while its inclination is smaller than 6°.

(9) Within the framework of an evolutionary sequence of FUors proposed by Quanz et al. (2007, ApJ 668, 359) and Green et al. (2006, ApJ 648, 1099), I classified Parsamian 21

as an intermediate-aged young eruptive star. This conclusion is supported by the weak silicate emission at 10 μm, the opening angle of 60° of the polar cavity, the shape of the spectral energy distribution, and the bolometric temperature, characteristic of a Class I / Class II transition object.

Conclusions

This work has demonstrated the feasibility and importance of multiepoch, multiwavelength studies as well as of high spatial resolution observations of young stellar objects. Combining data obtained with different instruments at different epochs requires great care and a secure knowledge of instrument effects. Reducing data from non-standard observation modes, such as differential polarimetric imaging at the Very Large Telescope, also requires careful data handling. However, all these work worth to do, since with their help one can obtain information about the target that would be inaccessible with any other, more traditional methods.

The observational results presented here on OO Ser, V1647 Ori and Parsamian 21 are all in general agreement with the standard picture of FUors. I found that the outburst model described in Bell et al. (2005) is consistent with the light curves of OO Ser and V1647 Ori. The model geometry (involving a central star, an accretion disk, and a circumstellar envelope) is also consistent both with the spectral energy distributions of all three sources, and with the circumstellar geometry seen in the polarimetric images of Parsamian 21.

The analysis, however, also revealed some differences between these three objects, supporting the suspicion that the group of FUors is very inhomogeneous. It might well be that there is a transition between the two classes, FUors and EXors. OO Ser and V1647 Ori might represent such transition objects. We are still far from being able to build a comprehensive picture of the FUor phenomenon. Nevertheless, the concept of an evolutionary sequence to explain the differences between individual FUors seems to be a promising direction.

Acknowledgements

I am grateful to the Konkoly Observatory of the Hungarian Academy of Sciences and its director, Lajos G. Balázs, for the possibility that I could work here and use the computer facilities and the nice library. I am also grateful to my thesis advisors, Kristóf Petrovay (Eötvös University) and Péter Ábrahám (Konkoly Observatory). My thanks and appreciation to my colleagues (and former colleagues) at Konkoly Observatory: Timea Csengeri, Szilárd Csizmadia, Mária Eredics, Attila Juhász, Csaba Kiss, Mária Kun, Attila Moór, László Mosoni, Miklós Rácz, Nikoletta Sipos, László Szabados, and Viktor L. Tóth.

My thanks must go also to all my collaborators from foreign institutes, especially Dániel Apai (University of Arizona), Carol A. Grady (GSFC), Thomas Henning (MPIA), Timo Prusti (ESA), Jose Acosta-Pulido (IAC), Sascha Hony (KU Leuven), and Ralf Siebenmorgen (ESO). It was a pleasure to work with you!

In 2006-2007 I had the opportunity to have a half-year scholarship at the Spitzer Science Center (Infrared Processing and Analysis Center, Caltech, Pasadena, USA). I am grateful to David R. Ardila (Caltech) for being my supervisor for this period.

I must acknowledge all my colleagues at the Department of Astronomy of the Eötvös University and at the Baja Astronomical Observatory.

I must thank Péter Ábrahám, Attila Moór, Nikoletta Sipos and László Szabados for their help with the careful proofreading and printing of this dissertation.

I need to express my gratitude and deep appreciation to Péter, Mari, Attila, and Csaba. Their friendship and thorough knowledge in astronomy was extremely helpful during my time at Konkoly Observatory. They have consistently helped me in all kinds of problems and shown me how to stay a sane human person when dealing with scientist, bureaucrats, and life in general. I'm in your debt!

Of course none of this work would have been possible without the continuous, unwavering, and unconditional support of my family.

Bibliography

Ábrahám, P., Kóspál, A., Csizmadia, S., et al. 2004b, A&A., 419, L39

Ábrahám, P., Kóspál, Á., Csizmadia, S., et al. 2004a, A&A, 428, 89

Ábrahám, P., Mosoni, L., Henning, T., et al. 2006, A&A, 449, L13

Acosta-Pulido, J. A., Kun, M., Ábrahám, P., et al. 2007, AJ, 133, 2020

Acosta-Pulido, J. A. et al. 2003, ING Newsl., 7, 15

Adams, F. C., Lada, C. J., & Shu, F. H. 1987, ApJ, 312, 788

Allen, L. E., Calvet, N., D'Alessio, P., et al. 2004, ApJS, 154, 363

André, P., Ward-Thompson, D., & Barsony, M. 1993, ApJ, 406, 122

Andrews, S. M., Rothberg, B., & Simon, T. 2004, ApJ, 610, L45

Apai, D., Pascucci, I., Brandner, W., et al. 2004, A&A, 415, 671

Aspin, C., Barbieri, C., Boschi, F., et al. 2006, AJ, 132, 1298

Bastien, P. & Ménard, F. 1990, ApJ, 364, 232

Bell, K. R., Cassen, P., Klahr, H. H., & Henning, T. 1997, ApJ, 486, 372

Bell, K. R. & Lin, D. N. C. 1994, ApJ, 427, 987

Bell, K. R., Lin, D. N. C., Hartmann, L. W., & Kenyon, S. J. 1995, ApJ, 444, 376

Blommaert, J. A. D. L., Siebenmorgen, R., Coulais, A., et al., eds. 2003, The ISO Handbook, Volume II - CAM - The ISO Camera

Boogert, A. C. A., Pontoppidan, K. M., Lahuis, F., et al. 2004, ApJSS, 154, 359

Bouchet, P., Schmider, F. X., & Manfroid, J. 1991, Ap&SS, 91, 409

Briceño, C., Vivas, A. K., Hernández, J., et al. 2004, ApJ, 606, L123

Cardelli, J. A., Clayton, G. C., & Mathis, J. S. 1989, ApJ, 345, 245

Cesarsky, C. J., Abergel, A., Agnese, P., et al. 1996, A&A., 315, L32

Chen, H., Myers, P. C., Ladd, E. F., et al. 1995, ApJ, 445, 377

Chiang, E. I. & Goldreich, P. 1997, ApJ, 490, 368

Clegg, P., Ade, P., Armand, C., et al. 1996, A&A., 315, L38

Cohen, J. G., Frogel, J. A., Persson, S. E., & Elias, J. H. 1981, ApJ, 249, 481

Cutri, R. M. et al. 2003, Explanatory Supplement to the 2MASS All Sky Data Release (Pasadena, Caltech)

Dame, T. & Thaddeus, P. 1985, ApJ, 297, 751

de Graauw, T., Haser, L. N., Beintema, D. A., et al. 1996, A&A., 315, L49

Decin, L. 2005

Diolaiti, E., Bendinelli, O., Bonaccini, D., et al. 2000, Proc. SPIE, 4007, 879

Draine, B. T. 2003, Ann. Rev. Astron. Astrophys., 41, 241

Draper, P. W., Warren-Smith, R. F., & Scarrott, S. M. 1985, MNRAS, 212, 1P

Edwards, S., Fischer, W., Hillenbrand, L., & Kwan, J. 2006, ApJ, 646, 319

Eiroa, C., Oudmaijer, R. D., Davies, J. K., et al. 2002, A&A., 384, 1038

Eislöffel, J. & Mundt, R. 1997, AJ, 114, 280

Fischer, O., Henning, T., & Yorke, H. W. 1996, A&A, 308, 863

Frieswijk, W. F., Shipman, R. F., & Lahuis, F. 2004, http://ida.esac.esa.int:8080/hpdp/technical_reports/technote12.pdf

Gabriel, C. et al. 1997, Proc. of the ADASS VI Conference, ASP Conf. Ser., 125, 108

Gibb, E. L., Rettig, T. W., Brittain, S. D., et al. 2006, ApJ, 641, 383

Green, J. D., Hartmann, L., Calvet, N., et al. 2006, ApJ

Grosso, N., Kastner, J. H., Ozawa, H., et al. 2005, A&A, 438, 159

Hajjar, R., Bastien, P., & Nadeau, D. 1997, Canada-France-Hawaii Telescope Information Bulletin, 37, 3

Hamilton, C. M., Herbst, W., Vrba, F. J., et al. 2005, AJ, 130, 1896

Hartmann, L. 2000, Accretion Processes in Star Formation (Cambridge University Press), 77–101

Hartmann, L. & Kenyon, S. J. 1996, ARA&A, 34, 207

Hartung, M., Bizenberger, P., Boehm, A., et al. 2000, in Proc. SPIE Vol. 4008, p. 830-841, Optical and IR Telescope Instrumentation and Detectors, Masanori Iye; Alan F. Moorwood; Eds., 830–841

Henning, T., Burkert, A., Launhardt, R., Leinert, C., & Stecklum, B. 1998, A&A, 336, 565

Herbig, G. H. 1966, Vistas in Astronomy, 8, 109

—. 1977, ApJ, 217, 693

—. 1989, ESO Workshop on Low-Mass Star Formation and Pre-Main Sequence Objects (ESO, Garching), 233

Hessman, F. V. 1991a, A&A., 246, 137

Hessman, F. V., Eisloeffel, J., Mundt, R., et al. 1991b, ApJ, 370, 384

Hillenbrand, L. A., Strom, S. E., Vrba, F. J., et al. 1992, ApJ, 397, 613

Hines, D. C., Schmidt, G. D., & Schneider, G. 2000, PASP, 112, 983

Hines, D. C. & Schneider, G. 2006, Proceedings of the 2005 HST calibration workshop, 153

Hodapp, K.-W. 1999, AJ, 118, 1338

Hodapp, K.-W., Hora, J. L., Hall, D. N. B., et al. 1996a, New Astronomy, 1, 177

Hodapp, K.-W., Hora, J. L., Rayner, J. T., Pickles, A. J., & Ladd, E. F. 1996b, ApJ, 468, 861

Hubble, E. P. 1922, ApJ, 56, 400

Hughes, J., Hartigan, P., Krautter, J., & Kelemen, J. 1994, AJ, 108, 1071

Hurt, R. L. & Barsony, M. 1996, ApJ, 460, L45

Johnstone, D., Fich, M., Mitchell, G. F., & Moriarty-Schieven, G. 2001, ApJ, 559, 307

Juhász, A., Prusti, T., Ábrahám, P., & Dullemond, C. 2007, MNRAS, 374, 1242

Kaas, A. A., Olofsson, G., Bontemps, S., et al. 2004, A&A., 421, 623

Kastner, J. H., Richmond, M., Grosso, N., et al. 2004, Nature, 430, 429

—. 2006, ApJ, 648, L43

Kenyon, S. J. & Hartmann, L. W. 1987, ApJ, 323, 714

—. 1991, ApJ, 383, 664

Kenyon, S. J., Hartmann, L. W., & Kolotilov, E. A. 1991, PASP, 103, 1069

Kessler, M. F., Steinz, J. A., Anderegg, M. E., et al. 1996, A&A., 315, L27

Koornneef, J. 1983, A&A, 128, 84

Kóspál, A., Ábrahám, P., Acosta-Pulido, J., et al. 2005, IBVS, 5661, 1

Kóspál, A., Ábrahám, P., Prusti, T., et al. 2007, A&A, 470, 211

Kuhn, J. R., Potter, D., & Parise, B. 2001, ApJ, 553, L189

Kwok, S. 1993, ARA&A, 31, 63

Larsson, B., Liseau, R., Men'shchikov, A. B., et al. 2000, A&A., 363, 253

Laureijs, R. J., Klaas, U., Richards, P. J., Schulz, B., & Ábrahám, P., eds. 2003, The ISO Handbook, Volume IV - PHT - The Imaging Photo-Polarimeter

Lemke, D., Klaas, U., Abolins, J., et al. 1996, A&A., 315, L64

Lenzen, R., Hofmann, R., Bizenberger, P., et al. 1998, in Proc. SPIE Vol. 3354, p. 606-614, Infrared Astronomical Instrumentation, Albert M. Fowler; Ed., 606–614

Li, W., Evans, N., Harvey, P., et al. 1994, ApJ, 433, 199

Malbet, F., Berger, J.-P., Colavita, M. M., et al. 1998, ApJ, 507, L149

Malbet, F., Lachaume, R., Berger, J.-P., et al. 2005, A&A, 437, 627

Manchado, A. et al. 2004, Proceedings of the SPIE, 5492, 1094

Manchado-Torres, A. et al. 2003, in Proc. of the SPIE, Instrument Design and Performance for Optical/Infrared Ground-based Telescopes, Vol. 4841, 160

Mazzuca, L. & Hines, D. 1999, Instrument Science Report NICMOS ISR-99-004

McGehee, P. M., Smith, J. A., Henden, A. A., et al. 2004, ApJ, 616, 1058

McNeil, J. W., Reipurth, B., & Meech, K. 2004, IAU Circ., 8284, 1

Meakin, C. A., Hines, D. C., & Thompson, R. I. 2005, ApJ, 634, 1146

Meyer, M. R., Calvet, N., & Hillenbrand, L. A. 1997, AJ, 114, 288

Millan-Gabet, R., Monnier, J. D., Akeson, R. L., et al. 2006, ApJ, 641, 547

Mundt, R., Brugel, E. W., & Buehrke, T. 1987, ApJ, 319, 275

Muzerolle, J., Calvet, N., & Hartmann, L. 1998a, ApJ, 492, 743

—. 2001, ApJ, 550, 944

Muzerolle, J., Hartmann, L., & Calvet, N. 1998b, AJ, 116, 2965

Muzerolle, J., Megeath, S. T., Flaherty, K. M., et al. 2005, ApJ, 620, L107

Neckel, T. & Staude, H. J. 1984, A&A, 131, 200

Ojha, D. K., Ghosh, S. K., Tej, A., et al. 2006, MNRAS, 368, 825

Ojha, D. K., Kusakabe, N., Tamura, M., et al. 2005, PASJ, 57, 203

Ott, S. et al. 1997, Proc. of the ADASS VI Conference, ASP Conf. Ser., 125, 34

Parsamian, E. 1965, Izv. Akad. Nauk Armyan. SSR., Ser., 18, 146

Parsamian, E. S., Gasparian, K. G., & Ohanian, G. B. 1996, Astrophysics, 39, 121

Persson, S. E., Murphy, D. C., Krzeminski, W., et al. 1998, AJ, 116, 2475

Polomski, E. F., Woodward, C. E., Holmes, E. K., et al. 2005, AJ, 129, 1035

Quanz, S., Henning, T., Bouwman, J., et al. 2007, ApJ, 668, 359

Quanz, S. P., Henning, T., Bouwman, et al. 2006, ApJ, 648, 472

Reipurth, B. & Aspin, C. 2004, ApJ, 606, L119

Rettig, T. W., Brittain, S. D., Gibb, E. L., Simon, T., & Kulesa, C. 2005, ApJ, 626, 245

Rousset, G., Lacombe, F., Puget, P., et al. 2003, in Adaptive Optical System Technologies II. Edited by Wizinowich, Peter L.; Bonaccini, Domenico. Proceedings of the SPIE, Volume 4839, pp. 140-149 (2003)., 140–149

Sandell, G. & Weintraub, D. A. 2001, ApJS, 134, 115

Savage & Mathis. 1979, ARA&A, 17, 73

Scarrott, R. M. J., Scarrott, S. M., & Wolstencroft, R. D. 1993, MNRAS, 264, 740

Semkov, E. H. 2006, IBVS, 5683, 1

Serra-Ricart, M., Oscoz, A., Sanchís, T., et al. 1999, ApJ, 526, 40

Shakura, N. I. & Sunyaev, R. A. 1973, A&A, 24, 337

Shu, F. H., Adams, F. C., & Lizano, S. 1987, Ann. Rev. Astron. Astrophys., 25, 23

Stahler, S. W. & Palla, F. 2004, The Formation of Stars (Weinheim: Wiley-VCH)

Staude, H. J. & Neckel, T. 1992, ApJ, 400, 556

Stetson, P. B. 1987, PASP, 99, 191

Tinbergen, J. 1996, Astronomical Polarimetry (Cambridge University Press)

Tsukagoshi, T., Kitamura, Y., Kawabe, R., et al. 2005, PASJ, 57, L21

Tuffs, R. J. & Gabriel, C. 2003, A&A, 410, 1075

Turner, N. J. J., Bodenheimer, P., & Bell, K. R. 1997, ApJ, 480, 754

Vacca, W. D., Cushing, M. C., & Rayner, J. T. 2003, PASP, 115, 389

Vacca, W. D., Cushing, M. C., & Simon, T. 2004, ApJ, 609, L29

Wachmann, A. A. 1954, Zeitschrift für Astrophysik, 35, 74

Walter, F. M., Stringfellow, G. S., Sherry, W. H., & Field-Pollatou, A. 2004, AJ, 128, 1872

Wassell, E., Grady, C., Woodgate, B., et al. 2006, ApJ, 650, 985

Whitney, B. A. & Hartmann, L. 1993, ApJ, 402, 605

Whittet, D. C. B., Martin, P. G., Hough, J. H., et al. 1992, ApJ, 386, 562

Összefoglalás

A fiatal eruptív csillagok (FU Orionis- és EX Lupi-típusú objektumok) a fősorozat előtti csillagok kis, de nagyon fontos csoportját alkotják. Jellemzőjük, hogy egy kitörés során fényességük akár 100-szorosára is nőhet. A kitörés valószínűleg összefügg a csillagkörüli korongról a csillagra történő megnövekedett tömegakkrécióval. Értekezésemben három fiatal eruptív csillagot vizsgálok részletesebben, űrcsillagászati és földi, optikai és infravörös hullámhosszakon történt megfigyelések segítségével.

Az OO Serpentis kitörése 1995 és 2006 között. Az OO Ser egy mélyen beágyazott, fősorozat előtti csillag, amely 1995-ben tört ki. Archív adatok (ISO, Spitzer), valamint új mérések alapján 10 különböző infravörös hullámhosszon összeállítottam a csillag fénygörbéit, amelyek azt mutatják, hogy a kitörés során a forrás az egész infravörös tartományban felfényesedett. Ezt egy hullámhosszfüggetlen halványodás követte, amelynek jelenlegi üteme arra utal, hogy a forrás nem fog visszatérni a kitörés előtti állapotba 2011 előtt. A kitörés időskálája rövidebb, mint ami az FU Orionis-típusú objektumoknál szokásos, de hosszabb, mint ami az EX Lupi-típusú objektumokra jellemző. A spektrális energiaeloszlás alapján az OO Ser egy korai 1. osztályú forrásnak tűnik, kora $< 10^5$ év. A kitörési modellekkel összhangban a csillagot valószínűleg egy akkréciós korong és egy sűrű burok veszi körül. A rövidebb időskála miatt az FU Orionis-típusú csillagokra kifejlesztett modellek csak akkor alkalmazhatók az OO Ser-re, ha a viszkozitás a csillagkörüli korongban egy nagyságrenddel nagyobb, mint az FU Orionis-típusú objektumoknál szokásos.

A V1647 Orionis 2004 és 2006 közötti kitörése és környezete. A V1647 Ori egy fősorozat előtti csillag, amely alig 4 hónap alatt váratlanul felfényesedett, 2004 februárjában érve el maximális fényességét. Részt vettem egy fotometriai monitorozó programban, melynek során $VR_CI_CJHK_S$ szűrőkkel készültek felvételek a csillagról. A csillag a maximális fényesség elérése után lassú ütemben halványodott, majd – meglepő módon – 2005 októberében hirtelen visszahalványodott a kitörés előtti állapotába. A kitörés időskálája és a forrás bolometrikus luminozitásának nem túl nagy változása arra utal, hogy a V1647 Ori eltér mind az FU Orionis-, mind az EX Lupi-típusú csillagoktól. Megvizsgáltam a csillagnak és a környező reflexiós köd bizonyos részeinek fényváltozásai közötti időeltérést is, és ebből következtetéseket vontam le a rendszer geometriájára. A közeli infravörös színtérképek arra utalnak, hogy a rendszert egy akkréciós korong és egy kiterjedt burok veszi körül.

A Parsamian 21 nagyfelbontású polarimetriás mérései. A Parsamian 21 egy fősorozat előtti csillagból és az azt körülvevő kiterjedt reflexiós ködből álló FU Orionis-típusú rendszer. A objektumról nagy térbeli felbontású közeli-infravörös direkt és polarimetriás mérések készültek az *Európai Déli Observatórium (ESO)* 8 m-es távcsövével a *NACO* adaptív optikás műszerrel. Ezeket a méréseket archív infravörös észlelésekkel egészítettem ki, melyek a *Hubble*, *Spitzer* és az *ISO* űrtávcsővel készültek. A mérések eredményéből megállapítottam, hogy (1) a csillag valószínűleg valóban FU Orionis-típusú; (2) a csillag nem tartozik semmilyen fiatal csillaghalmazhoz; (3) a csillagot egy éléről látott csillagkörüli korong és egy burok veszi körül, az utóbbin kúp alakú nyílással a pólusok irányában (4) a korong geometriailag lapos és a csillagtól 48-tól 360 cs.e. távolságig lehet követni; (5) a csillag spektrális energiaeloszlása reprodukálható egy egyszerű korong+burok modellel; (6) az FU Orionis-típusú csillagokra irodalomban publikált evolúciós elméletek alapján a csillag közepes korúként klasszifikálható.

Summary

Young eruptive stars (FU Orionis- and EX Lupi-type objects) form a small, but remarkable subgroup of pre-main sequence stars. They are characterized by eruptions which may increase the brightness of the system by as much as a factor of 100. Outbursts probably correspond to increased accretion from the circumstellar disk to the star. In my dissertation I present the detailed analysis of three young eruptive stars using ground-based and space-borne observations at optical and infrared wavelengths.

The outburst of OO Serpentis between 1995 and 2006. OO Ser is a deeply embedded young star that produced an eruption in 1995. Using archival (ISO, Spitzer) and new observations, I constructed the light curves of the star at ten different infrared wavelengths. My results show that the eruption caused brightening in the whole infrared regime, which is followed by a slow, wavelength-independent fading. The fading is still ongoing and the star will probably not return to quiescence before 2011. The timescale of the outburst is shorter than that of typical FU Ori-type objects, but longer than that of EX Lupi-type stars. Based on the spectral energy distribution, OO Ser seems to be an early Class I object with an age of $< 10^5$ yr. In accordance with outburst models, the star is probably surrounded by an accretion disk and a dense envelope. Due to the shorter timescales, outburst models developed for FU Ori-type stars can only work for OO Ser if the viscosity of the circumstellar disk is set to an order of magnitude larger value than usual for FU Ori objects.

The 2004–2006 outburst and environment of V1647 Orionis. V1647 Ori is a pre-main sequence star that suddenly brightened up in less than 4 months, reaching its peak brightness in 2004 February. I participated in a monitoring program, in which we obtained $VR_CI_CJHK_S$-band observations. After reaching its peak brightness, the star was fading very slowly. Then, in 2005 October it suddenly faded back to its quiescence level. The timescale of the outburst and the moderate increase in bolometric luminosity suggest that V1647 Ori differs both from FU Ori- and EX Lupi-type objects. By calculating the time delay between the brightness variations of the star and a nebular position, I deduced the geometry of the system. The near-infrared color maps of the nebula suggest that the star is surrounded by a disk and an extended nebula.

High-resolution polarimetry of Parsamian 21. Parsamian 21 is an FU Orionis-type object consisting of a central star and an extended reflection nebula. We obtained high spatial resolution adaptive optics assisted near-infrared direct and polarimetric observations with the NACO instrument at ESO's Very Large Telescope. I complemented these measurements with archival Hubble, Spitzer and ISO data. The results revealed that (1) the star is probably indeed an FU Orionis-type objectar; (2) the star is not associated with any known rich cluster of young stars; (3) the star is surrounded by an edge-on disk, and a circumstellar envelope with a polar cavity; (4) the disk seems to be flat and extends from at least 48 to 360 AU from the star; (5) the spectral energy distribution can be successfully modeled with a circumstellar disk and an envelope; (6) within the framework of an evolutionary sequence of FU Ori-type stars, Parsamian 21 seems to be an intermediate-aged object.